Analysing Transient Effects in the Ionosphere Using Narrowband VLF Data

by

Sherry Bremner

Submitted in partial fulfilment of the requirements for the degree of Master of Science in the School of Physics, University of KwaZulu-Natal.

As the candidate's Supervisor I have/have not approved this thesis for submission

Signed: ..... Name: ..... Date: .....

Durban, 2009.

Abstract Very Low Frequency (VLF) radio waves propagate within the Earth-ionosphere waveguide with very little attenuation. Modifications of the waveguide geometry affect the propagation conditions, and hence, the amplitude and phase of VLF signals. Changes in the ionosphere, such as the presence of the D-region during the day, or the precipitation of energetic particles, are the main causes of this modification. Using narrowband receivers monitoring remote VLF transmitters, the amplitude and phase of these signals are recorded. A multivariate data analysis technique, Principal Component Analysis (PCA), is applied to the data in order to determine parameters such as seasonal and diurnal changes which affect the variation of these signals. Data was then analysed for effects from extragalactic gamma ray bursts, terrestrial gamma ray flashes and solar flares. Only X-rays from solar flares were shown to have an appreciable affect on ionospheric propagation.

PREFACE

The experimental work described in this dissertation was carried out at the Hermanus Magnetic Observatory, Hermanus, and in the School of Physics, University of KwaZulu-Natal, Durban, from January 2008 to December 2009 under the supervision of Dr Andrew B. Collier.

These studies represent original work by the author and have not otherwise been submitted in any form for any degree or diploma to any tertiary institution. Where use has been made of the work of others it is duly acknowledged in the text.

DECLARATION 1 - PLAGIARISM

I, ..., declare that

1. The research reported in this thesis, except where otherwise indicated, is my original research.
2. This thesis has not been submitted for any degree or examination at any other university.
3. This thesis does not contain other persons' data, pictures, graphs or other information, unless specifically acknowledged as being sourced from other persons.
4. This thesis does not contain other persons' writing, unless specifically acknowledged as being sourced from other researchers. Where other written sources have been quoted, then:
   (a) Their words have been re-written but the general information attributed to them has been referenced
   (b) Where their exact words have been used, then their writing has been placed in italics and inside quotation marks, and referenced.
5. This thesis does not contain text, graphics or tables copied and pasted from the Internet, unless specifically acknowledged, and the source being detailed in the thesis and in the References sections.

Signed: .....

DECLARATION 2 - PUBLICATIONS

DETAILS OF CONTRIBUTION TO PUBLICATIONS that form part and/or include research presented in this thesis (include publications in preparation, submitted, *in press* and published and give details of the contributions of each author to the experimental work and writing of each publication)

No publications resulted from this research.

Signed: .....

ACKNOWLEDGEMENTS

I would like to thank J. Lichtenberger, Space Research Group, Eötvös University for the use of the data recorded by the UltraMSK system in Tihany, Hungary; my fellow students for their support and ideas; C. Rodger and M. Clilverd for the countless ideas and willingness to search through data for possible events; and my supervisor, Dr A Collier, whose support, encouragement, ideas and occasional criticism have not only made this project possible, but also made it make sense.

A special thank you to my friends and family who have provided so much support throughout my studies.

Contents

List of Figures

List of Tables

Chapter 1

Introduction

Very Low Frequency (VLF) radio waves are those with frequencies in the range 3 – 30 kHz. These signals travel with very little attenuation in the spherical waveguide formed by the Earth and ionosphere. The ionosphere, which is the electrically conducting region of the upper atmosphere, thus plays an important role in the propagation of VLF waves. As the ground remains mainly electrically constant, modifications in the waveguide, and thus changes in the VLF propagation conditions, are mostly generated by changes in the ionosphere.

The ionosphere has layers, divided by differing regions of electron density. These are named D, E and F regions. The D region, present only during the day when Lyman-α radiation (121.6 nm) from the Sun ionises the neutral nitric oxide (NO) constituent of the atmosphere, is the most important factor in VLF propagation. Figure 1.1 shows the electron density of the ionosphere as

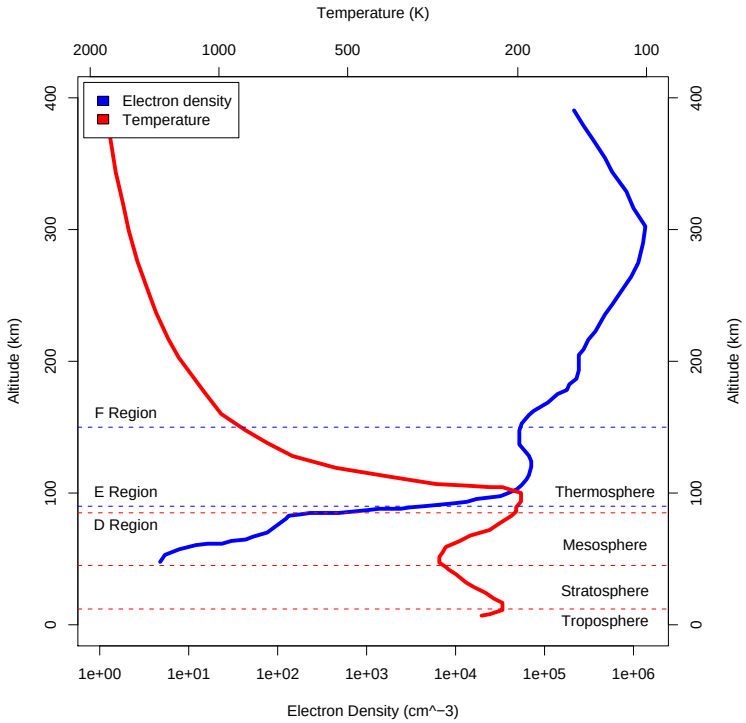

Figure 1.1: An illustration of the ionospheric profile of electron density and temperature. The layers are indicated by dashed lines, where blue refers to ionospheric layers (divisions defined by electron density) and red refers to atmospheric layers (divisions defined by temperature). Adapted from `http://ion.le.ac.uk/ionosphere/profile.html`.

it changes with height. The D, E and F regions are indicated at their approximate heights. The temperature profile of the atmosphere is also shown.

During the day, the D region forms the top boundary of the Earth-ionosphere waveguide. However, at night the D region disappears and hence the E region takes on this role, although it is weakened by the lack of an ionising source.

Propagation of VLF waves in the Earth-ionosphere waveguide has been a well studied problem for many years. There are many ways to calculate the propagation conditions, most based on numerical or approximate analytical solutions of waveguide mode propagation (Budden, 1957; Wait, 1962). With the increasing use and availability of high performance processors in computers, other methods such as Finite Difference Time Domain (FDTD) modeling are feasible (Cummer, 2000; Chevalier and Inan, 2006).

In waveguide mode propagation, a big problem is to define the boundary conditions, namely the electrical conditions of the bottom of the ionosphere. The daytime D region electron densities are well described as increasing exponentially with height. This is done by using two traditional parameters, defined by Wait, the D region height, H' in km , and the sharpness of the lower edge, β in km^{-1}

These parameters have successfully been used, along with VLF measurements, to describe normal daytime variations in the D region electron densities (Thomson, 1993) and the enhanced densities occurring during solar flares (Thomson et al., 2002).

Experimental work on VLF propagation has mainly entailed the use of the broadband electromagnetic signals from lightning discharges. Lightning is by far the most prolific natural source of VLF radiation, the signals (termed spherics) travel far in the Earth-ionosphere waveguide, providing a means of determining the reflection height of the ionosphere, as well as estimating the attenuation constant of VLF waves in the waveguide. Barr et al. (2000) give a useful overview of this research.

Spherics arrive at receivers as a single pulse of broadband radiation, with a duration 1 – 10 ms. The analysis of the amplitude spectra of spherics recorded at increasing distances gives an estimate of the attenuation constant in the VLF band. Figure 1.2 shows the experimentally determined attenuation as a function of frequency consolidated from a number of sources (Wait, 1962).

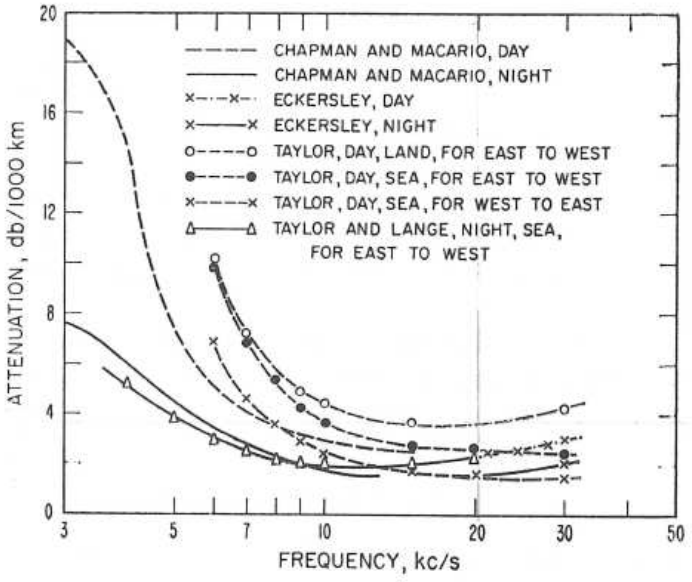

Figure 1.2: Experimental determination of attenuation of signals in VLF range. After Wait (1962).

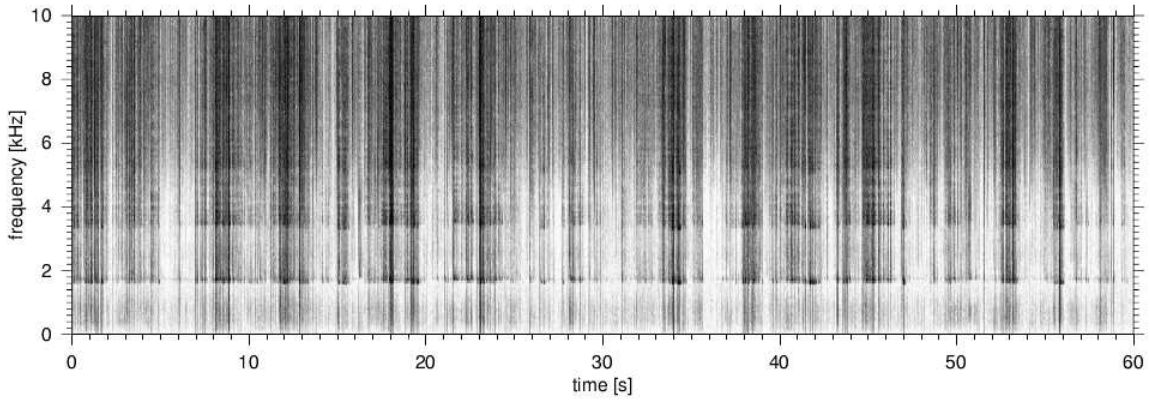

Figure 1.3: Tweek spectrogram, showing waveguide cutoffs. Recorded on 23 February 2003 at 21:00 UT, at the South African National Antarctic Expedition base, SANAE IV.

From Figure 1.2 it is apparent that VLF signals suffer very little attenuation over incredibly large distances. The attenuation constant ranges between 2 – 5 dB per 1000 km.

The reflection height of the ionosphere is determined with the use of tweek spherics. Tweeks are produced by propagation over very long distances, thus the pulse radiation undergoes dispersion, with the higher frequencies arriving at the receiver fractions of a second before the lower frequencies. Since the group velocity of the wave packet propagating in the waveguide tends to zero at the waveguide cutoff, there is a significant reduction of wave power at these cutoff frequencies. The cutoffs of adjacent tweek spherics form a well-defined horizontal line on a spectrogram.

The height of the ionosphere is estimated by recalling that the transverse magnetic cutoff frequency in a parallel plate waveguide is given by

$$\nu_c = \frac{mc}{2a} \tag{1.1}$$

where $m = 1, 2, 3, \ldots$ represents the mode number, c is the velocity of light and a is the height of the waveguide (Pollack and Stump, 2002). The cutoffs, clearly seen in the tweek spectrum, see Figure 1.3, can then be used to calculate the height of the ionosphere. The horizontal lines seen on the spectrogram correspond to the waveguide cutoffs for different modes. For the lowest order mode, $m = 1$, the height of the ionosphere can be calculated by inverting (1.1) to form

$$a = \frac{c}{2\nu_c}. \tag{1.2}$$

Taking the observed fundamental cutoff as 1.8 kHz yields an estimate of $a = 83.3$ km. This model, however, is highly simplistic.

The ionospheric height varies diurnally, with the development of the D region, thus the propagation conditions reflect this variation. The changing reflection height changes the cutoff frequencies as well as the attenuation constant. Propagation during the day time is weaker, due to the lower reflection height, yet it is also more stable than night time propagation. This is partly because most perturbations occur at higher altitudes, namely in the E region and above.

The passage of the day-night terminator (the line between day and night on the Earth) also creates changes in the waveguide, resulting in depressions of VLF wave amplitudes. It is not possible to explain these field strength variations during sunrise and sunset with single mode propagation theory, thus Crombie (1964) used two waveguide modes, with mode conversion occurring at the day-night boundary to model this effect. Pappert and Morfitt (1975) presented a mode

conversion program that modeled the minima with reasonable agreement with observations. Lynn (1967) found that the terminator effects were dependent on the angle between the propagation path and the day-night terminator. In a study of a signal with a North–South propagation path, Clilverd et al. (1999) showed that the majority of features observed in the amplitude variation were consistent with mode conversion.

The US Navy operates a network of VLF transmitters, used to communicate with their submarines, as VLF waves have a large skin depth in salt water. These transmitters operate on set frequencies in the upper half of the VLF band, with a few operating outside of it. They are distributed over the surface of the Earth, mostly in the Northern hemisphere, with only one in the Southern hemisphere, making a global network. VLF receivers run by a number of academic and research institutions all over the world monitor these signals. As these signals are affected by the propagation conditions in the Earth-ionosphere waveguide, and the Earth remains mostly electrically constant, changes in the waveguide are caused mainly by changes in the ionosphere. Thus, this network of transmitters provide a useful probe of ionospheric conditions, including the annual and seasonal variations.

Chapter 2

Transient Events and their Effects

Transient events are ones that cause a sudden and temporary change in ionospheric conditions. These modify the Earth-ionosphere waveguide and hence, cause amplitude and phase perturbations in VLF signals. The types of events examined in this research are explained below.

2.1 Gamma Ray Bursts

Gamma Ray Bursts (GRBs) are brief, intense flashes of high energy photons, originating in violent explosions occurring in distant galaxies. These explosions are thought to be the outcome of the formation of black holes, via the collapse of a massive star, or the collision of two compact objects (ie. neutron stars or black holes) orbiting in a binary system (Meszaros, 2006). The duration of a GRB varies from a fraction of a second to several minutes. Although brief, GRBs outshine all other sources of γ-rays in the sky. GRBs are isotropically distributed in the sky and would be observed with a frequency of approximately one per day if it was possible to observe the entire sky continuously.

2.1.1 Temporal Structure

GRBs are divided into long and short bursts, with the watershed being $t = 2$ s. The possible duration of bursts spans the range from less than 0.01 s to more than 100 s. Long GRBs are highly variable, often showing variations in the flux on a time scale that is much shorter than the duration of the burst (Piran, 2005). They are often comprised of multiple pulses in flux, where each pulse has a light curve that is characterised by a Fast Rise and Exponential Decay (FRED) (Norris et al., 1996). Those long GRBs that do not show substructure exhibit an overall FRED structure. Fenimore (1999) determined that the average temporal structure of 36 bright bursts has a sharp rise and linear decay.

It is difficult to determine the variability of short bursts due to the duration of the burst being close to the limiting resolution of most γ-ray detectors.

2.1.2 Burst Spectra

No two GRBs are the same, varying dramatically in both duration and energy flux. The spectrum is non-thermal, with the energy flux peaking at a few hundred keV. There is often a high energy tail that can extend up to GeV (Piran, 2005). Band et al. (1993) developed a phenomenological model that accurately fits a large range of observed GRB spectra. This model consists of two

power laws joined smoothly at a break energy $E_0 = (\alpha - \beta)E_0/(2 + \alpha)$,

$$f(E) = A \begin{cases} \left(\frac{E}{100}\right)^{\alpha} e^{-\frac{E(2+\alpha)}{E_0}} & \text{for } E < \frac{(\alpha-\beta)E_0}{(2+\alpha)} \\ \left[\frac{(\alpha-\beta)E_0}{100(2+\alpha)}\right]^{(\alpha-\beta)} e^{(\beta-\alpha)\left(\frac{E}{100}\right)^{\beta}} & \text{for } E \geq \frac{(\alpha-\beta)E_0}{(2+\alpha)} \end{cases} \tag{2.1}$$

where $f(E)$ is the flux, A is the amplitude in photons $\mathrm{s}^{-1}\mathrm{keV}^{-1}\mathrm{cm}^{-2}$ and α and β are dimensionless spectral indices. The pivot energy of 100 keV is the energy at which the normalisation of A is determined.The lower boundary in energy of the higher energy power law is marked by E_0. Although there are no universal values for α, β and E_0, they tend to remain in specific ranges: $-1.5 \lesssim \alpha \lesssim 0.5$, $-2.8 \lesssim \beta \lesssim -1.9$ and $E_0 \sim 200$ keV (Preece et al., 2000). For most observed values of α and β, the peak γ-ray flux occurs at $E_p = (\alpha + 2)E_0$ (Piran, 2005). These model parameters may change with the detector observing the GRB.

As short bursts are entirely different creatures, this spectrum model does not apply to them.

2.1.3 Fluence

The bulk of the energy radiated by a GRB is in the γ-ray band of ~ 0.1 to 1 MeV. The total fluence (radiative flux integrated over time, which is equivalent to total integrated flux) in any one GRB ranges from 10^{-10} to 10^{-7} Jm^{-2} (10^{-7} to 10^{-4} erg cm^{-2}), where the lower limit depends on the limitations of the detector.

2.1.4 Example: GRB 080319B

GRBs are named for the date on which they occur, thus GRB 080319B was the second burst on 19 March 2008, beginning at 06:12:47 UT. This was a far from typical burst, displaying at its peak, the brightest optical and X-ray fluxes and one of the highest γ-ray fluxes. Although unusual, it is one of the best observed GRBs to date, making observational parameters easier to determine.

GRB 080319B had a duration of $\sim$60 s with a long decaying tail, extending up to 200 s in some energy bands. The fluence in the band 20 keV to 7 MeV was 5.72×10^{-7} Jm^{-2}. The spectrum is well-fit by the Band et al. (1993) model, with parameters determined by Golenetskii et al. (2008)

$$\begin{aligned} \alpha &= -0.822(-0.012, +0.014) \\ \beta &= -3.87(-1.09, +0.44) \\ E_p &= 651(-14, +13) \text{ keV}. \end{aligned} \tag{2.2}$$

The light curve is complex, being strongly energy dependent and showing many clearly separated pulses above 70 keV (Racusin et al., 2008). This is shown in Figure 2.1 where the counts per second in each detector are shown (Cummings et al., 2008). The count rate is shown for some time before and after the burst. Each energy band shows the same onset time, and similar sudden decreases in count rate after the burst, although the lower energy bands show a slowly decreasing tail. The burst itself varies erratically in all the energy bands shown here.

2.2 Terrestrial Gamma Ray Flashes

Terrestrial Gamma ray Flashes (TGFs) are exceptionally short bursts of X-rays and γ-rays observed by satellites, which occur below the satellite. They were first observed with the Burst and Transient Source Experiment (BATSE) on NASA's Compton Gamma Ray Observatory (CGRO). The exact source location of TGFs is unknown, but they are spatially correlated with areas of large thunderstorm activity (Grefenstette et al., 2009) and some TGFs have been temporally correlated with strong lightning flashes (Inan et al., 1996). Observations show that the altitude of

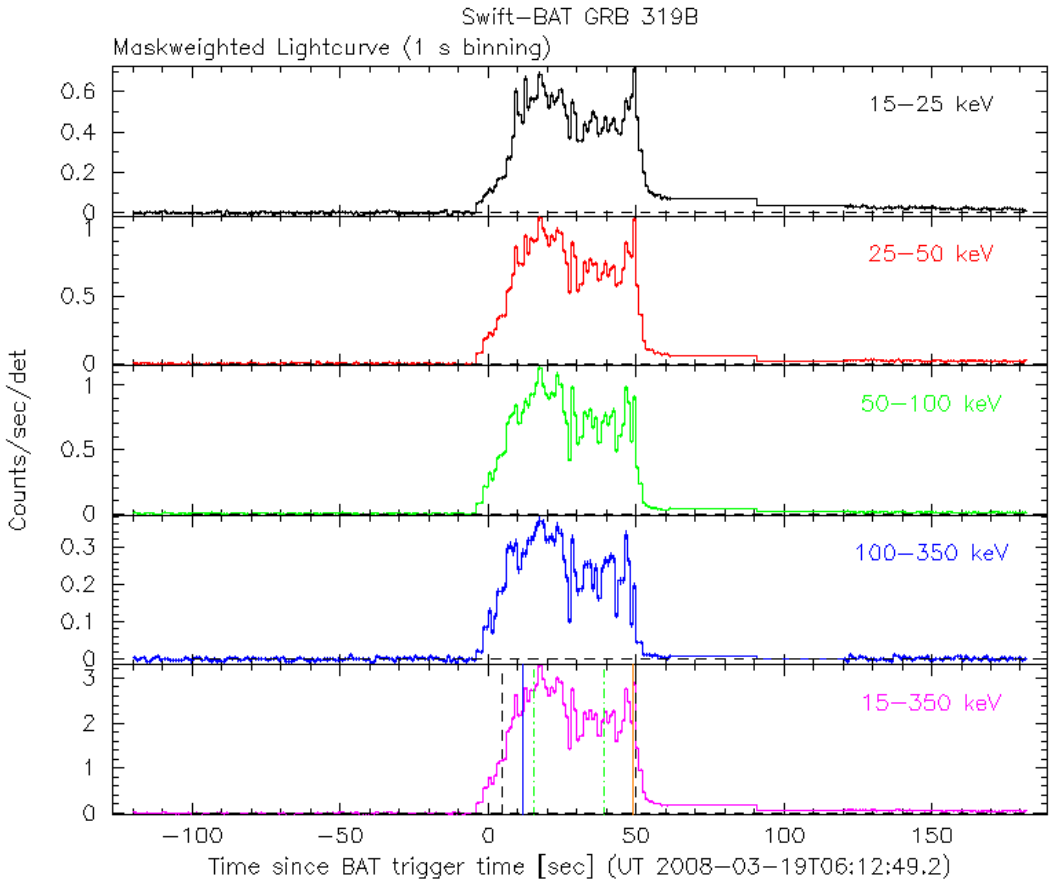

Figure 2.1: Lightcurve of GRB 080319B, showing the counts per second in each detector of BAT (Burst Alert Telescope) on the Swift satellite. After Cummings et al. (2008).

the source is lower than 21 km (Hazelton et al., 2009). The mechanism for the generation of TGFs has been extensively debated with the most likely explanation being a relativistic runaway electron avalanche process, which produces a large number of energetic electrons via multiplication and acceleration of a seed population (Gurevich et al., 1992; Dwyer and Smith, 2005). Dwyer (2008) determined that TGFs could not be produced by a seed population consisting of normal background radiation or cosmic ray air showers, rather preferring the explanation that the seed population is produced by a relativistic feedback process or runaway electron production in the strong electric fields associated with lightning leaders. Paiva et al. (2009) explored the possibility of the seed electrons being produced by muon decay.

TGF signatures are different from those of short GRBs in their extremely short durations, having peaks that last less than 1 ms.

2.2.1 Burst Spectra

The γ-ray spectrum of TGFs is consistent with bremsstrahlung emission from relativistic runaway electrons, with the spectrum extending above 20 MeV. With the launch of NASA's RHESSI satellite, it was discovered that the burst spectra had a hardening above 1 MeV. An example of an energy spectrum is shown in Figure 2.2, which was recorded by BATSE. Nemiroff et al. (1997)

fit a power law model to this spectrum, of the form

$$f = A(E/E_{piv})^{\alpha} \tag{2.3}$$

where f is the flux in photons $\mathrm{s}^{-1}\mathrm{keV}^{-1}\mathrm{cm}^{-2}$, A is the fitted amplitude parameter, E is the energy in keV, E_{piv} is the pivot energy, which was set at 100 keV and α is a dimensionless power law index. In Figure 2.2, the TGF spectrum is fit with a power law with $\alpha = -1.28 \pm 5.7 \times 10^{-2}$ and $A = 1.86 \times 10^{-1} \pm 1.6 \times 10^{-2}$ photons $\mathrm{s}^{-1}\mathrm{keV}^{-1}\mathrm{cm}^{-2}$.

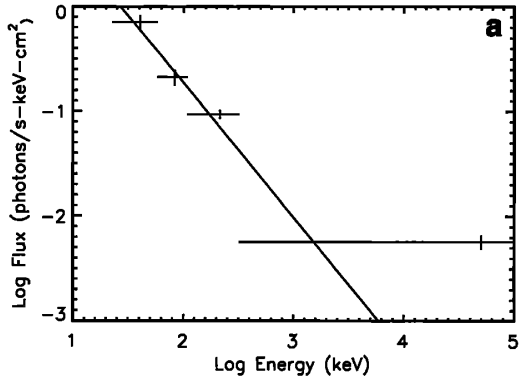

Figure 2.2: Four channel energy spectrum of a TGF that occurred on 22 April 1991 at 00:42:11 UT, with the diagonal solid line showing the best fit power law spectrum. After Nemiroff et al. (1997).

2.2.2 Temporal Structure

TGFs are extremely short and usually consist of several fast pulses. They vary over timescales between 26 µs and 250 µs, with the average peak lasting 50 µs (Nemiroff et al., 1997). This temporal structure is shown in the light curve of the TGF in Figure 2.3. The count rates in each energy band are highly variable, with multiple distinguishable peaks. The peak count rate does not occur at exactly the same time in each band and the structure of the TGF is also energy dependent.

2.3 Solar Flares

Solar flares are large explosions in the Sun's atmosphere, releasing between 10^{23} and 10^{25} J over time intervals ranging from a few seconds to many minutes. Occurring in regions of high magnetic intensity, such as sunspot groups, solar flares are caused by the sudden release of magnetic energy (Carroll and Ostlie, 1996). They cause electromagnetic radiation ranging from the kilometre-wavelength radio waves to very short wavelength γ-ray emission. Charged particles, protons and electrons, are also accelerated to energies exceeding 1 MeV.

2.3.1 Flare Classification

Solar flares are classified according to the peak X-ray flux in the 0.1 – 0.8 nm band (Bai and Sturrock, 1989), as received by the GOES satellites in geostationary orbit. The levels of classification are A, B, C, M and X, where the classes are arranged on a logarithmic scale. A class events have the lowest intensity, while X class are the most powerful. The classification is summarised in Table 2.3.1 below.

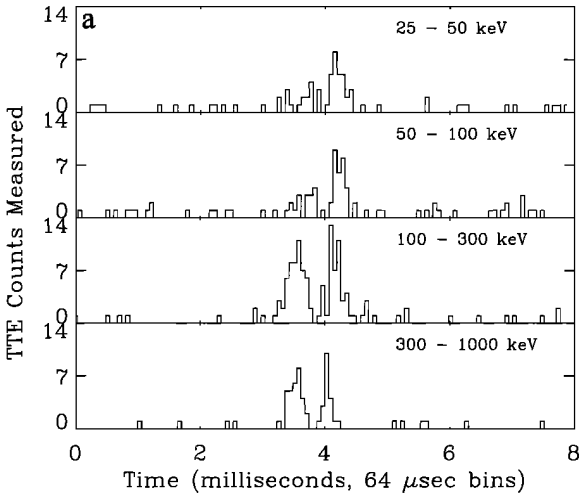

Figure 2.3: Temporal structure of a TGF that occurred on 22 April 1991 at 00:42:11 UT, given in the four energy bands of BATSE. After Nemiroff et al. (1997).

Table 2.1: Solar flare classification.

Class	mks system (Wm^{-2})	cgs system (erg $cm^{-2}s^{-1}$)
A	$I < 10^{-7}$	$I < 10^{-4}$
B	$10^{-7} < I < 10^{-6}$	$10^{-4} < I < 10^{-3}$
C	$10^{-6} < I < 10^{-5}$	$10^{-3} < I < 10^{-2}$
M	$10^{-5} < I < 10^{-4}$	$10^{-2} < I < 10^{-1}$
X	$10^{-4} < I < 10^{-1}$	$10^{-1} < I < 10^{2}$

Each solar flare, having been classified as either A, B, C, M or X, is then also given a number between 1 and 10, which is a further linear scale within each class. This is the multiplication factor of the peak X-ray flux for the flare. Thus a C4.5 flare has a peak flux of 4.5×10^{-6} Wm^{-2}.

2.3.2 Total Integrated Flux

The total integrated flux is the flux received over the entire duration of the burst. The total energy of solar flares spans many orders of magnitude, following a uniform distribution with flare frequency roughly proportional to the inverse of the total energy.

2.3.3 Temporal Structure

There are generally three stages to a solar flare. The first is the precursor stage, which occurs when the release of magnetic energy is triggered. Soft X-rays are emitted during this phase. The second stage is characterised by hard X-rays, γ-rays and radio waves. This is the impulsive phase, where electrons and protons are accelerated. The decay stage consists of the gradual build-up and then decay of soft X-rays. In total, a flare may last from a few seconds to many minutes. Some flares have a complex flux distribution, showing multiple peaks in the $0.1 - 0.8$ nm X-ray band.

Figure 2.4 shows an example of a flare on 27 April 1981 (Bai and Sturrock, 1989). This shows the energy flux in different energy bands, as well as the approximate evolution of the phases. The X-ray flux peaks during the main phase and slowly decreases in the decay phase. The evolution of

the flare is similar in all the energy bands, with the gaps in the high band caused by the recording satellites nights.

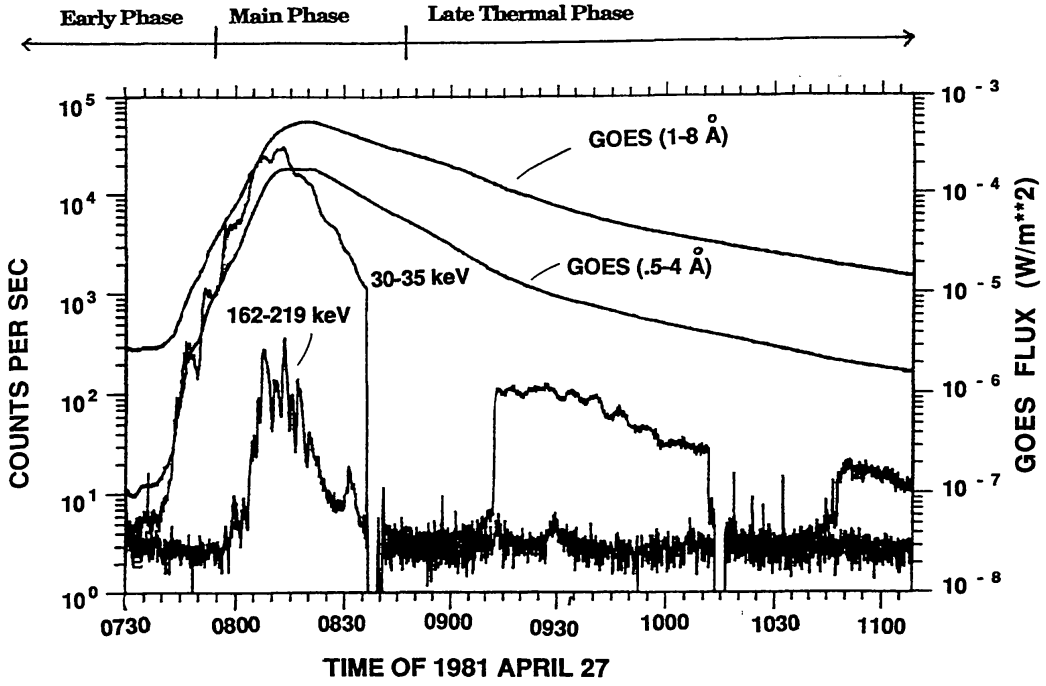

Figure 2.4: Example of a solar flare that occurred on 27 April 1981, with approximate phases of the X class flare indicated and the fluxes in different energy bands. After Bai and Sturrock (1989)

2.4 Effect on Sub-Ionospheric Propagation and Observations

Very Low Frequency (VLF) radio signals propagate with little attenuation over large distances in the Earth-ionosphere waveguide. Under quiescent conditions the propagation paths within this waveguide are stable. However, perturbations in the ionosphere lead to changes in the geometry of the waveguide, resulting in changes in the propagation conditions. The enhanced γ-ray and X-ray flux caused by GRBs and solar flares creates additional ionisation in the lower ionosphere, which leads to a perturbation in amplitude and phase of the signals from VLF navigation transmitters.

2.4.1 Gamma Ray Bursts

After the initial discovery of GRBs, it was proposed that the γ-rays of cosmic origin may cause an observable transient ionospheric effect. Brown (1973) calculated the energy deposition in the atmosphere by a proposed GRB with fluence 3×10^{-7} Jm^{-2} as a function of zenith angle. The peak energy deposition occurred at an altitude less than that considered the edge of the daytime D region, which is an altitude usually ionised by galactic cosmic rays. Brown (1973) hypothesized that the best opportunity to observe GRBs would be at low geomagnetic latitudes, where the cosmic ray ionisation would be of lesser magnitude.

A search for GRB transient effects was carried out by Kasturirangan et al. (1976). Fourteen GRBs, ranging in fluence from 7×10^{-9} to 1×10^{-7} Jm^{-2}, were examined and no ionospheric effects were observed. This was attributed to the short duration of the bursts (ranging from 1 to 30 seconds), which is much less than the relaxation time of the ionosphere at the relevant

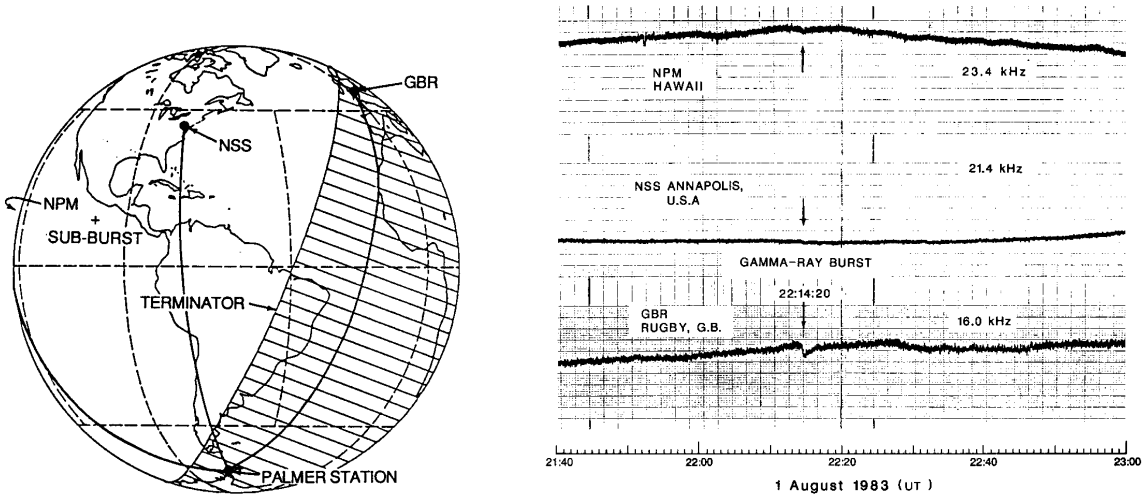

(a) System configuration at the time of GRB 830801.

(b) Amplitude of radio signals received at Palmer, Antarctica. The event is indicated with arrows at 22:14:20.

Figure 2.5: Observations of GRB 830801. After Fishman and Inan (1988).

altitude. The computed electron production profile rates peaked at an altitude of 70 – 75 km, and the authors estimate the electron density enhancement caused by the GRBs was insignificant at that height.

The first observation of a GRB causing an ionospheric disturbance was reported by Fishman and Inan (1988). GRB 830801 occurred at 22:14:18 UT and had a total fluence of 2×10^{-6} Jm^{-2}. The location on Earth directly below the burst is indicated by a cross on Figure 2.5(a). Also indicated are the great circle paths (GCPs) between three VLF transmitters, and the receiver at Palmer Station in Antarctica, as well as the location of the day/night terminator at the time of the burst. Figure 2.5(b) shows the amplitude of the transmitter signals. At the time of GRB 830801 a clear drop in amplitude of the GBR transmitter, whose path is completely in darkness, can be seen. However, this perturbation is not so apparent on the two transmitters with paths in daylight. Thus, the GRB created a small, but noticeable effect on the VLF signal. However, a burst of this magnitude is rarely detected.

Other astronomical γ-ray emitters have been known to create an ionospheric disturbance. Inan et al. (1999) report the observation of large amplitude and phase changes attributed to a giant periodic flare from a Soft Gamma Repeater, SGR 1900+14. The perturbations in the VLF signals exhibited the same periodicity as the flare.

2.4.2 Solar Flares

The effects of solar flares on the ionosphere are a long studied phenomenon. During quiet times the D region is maintained by Lyman-α radiation, which ionises neutral nitric oxide. The lower edge of the D region is also affected by cosmic rays. During a solar flare, the X-ray flux arriving at Earth increases dramatically. The X-rays cause major effects in the Earth's upper atmosphere, but are absorbed before reaching the ground. Although the Lyman-α radiation is also enhanced during a flare, the effect of the X-rays overwhelms it (Grubor et al., 2008). The extra ionisation in the ionosphere at this time lowers the reflection height of the D region. As VLF waves propagate within the Earth-ionosphere waveguide, the propagation conditions are modified, causing phase and amplitude anomalies in the subionospheric signals.

Bain and Hammond (1975) studied solar flares as the cause of Sudden Phase Anomalies (SPA) in VLF transmitter data. The magnitude of the SPAs was found to be dependent on the peak flux of the flare as well as the solar zenith angle. McRae and Thomson (2004) made use of the disturbances in phase and amplitude to calculate the D region electron density enhancement, as a function of solar flare flux. By deriving Wait's parameters, H' and β during the flare disturbances, they were able to extrapolate their results to other frequencies and estimate the amplitude and phase perturbation for these transmitters.

Thomson et al. (2004) used the phase anomaly produced by a solar flare to determine the peak flux of the flare, after it had saturated the detectors on the GOES satellites. Thomson et al. (2005) extended this work to include analysis of a number of large flares, noting that the phase perturbation varies in proportion to the logarithm of the X-ray flux, while the amplitude does not. They also utilised the amplitude and phase perturbations to determine the parameters H' and β, at the time of the flare.

Grubor et al. (2008) classified X-ray solar flares by their effects on the lower ionospheric electron density profile. The lowest class flare able to be detected in VLF amplitude and phase perturbations was determined as a C1 flare, corroborating results from Thomson et al. (2005). Modelling of the change in the ionospheric chemistry during a solar flare was undertaken by Enell et al. (2008), showing that the ion chemistry is significantly affected, while the neutral composition of the atmosphere is not.

2.4.3 Terrestrial Gamma Ray Flashes

TGFs have not as yet been recorded as having an effect on the amplitude and phase of VLF signals. These brief, energetic events, however, may cause ionisation within the Earth-ionosphere waveguide itself, as they are thought to be generated within a thunderstorm and hence originate within the troposphere. This is a topic for further research.

Chapter 3

Principal Components Analysis

3.1 Introduction

Many factors influence the subionospheric propagation of VLF signals. The development of the D region ionosphere during daylight hours, the passage of the terminator over the signal path, changes of season and the solar cycle are all causes of regular variations in the amplitude and phase of signals. These tend to paint a complicated picture, as many of these factors are related. Analysing the variations caused by transient effects is difficult when they are entangled amongst all the regular effects. Thus, it is necessary to find a technique that can unravel all the regular variations and their dependencies, in order to simplify the detection of transient effects.

Principal Components Analysis (PCA) is a multivariate data analysis technique that fulfills these requirements. PCA simplifies a data set by representing the data in fewer than the original number of variables, thus reducing the dimension of the problem. The success of the factoring technique relies on the existence of correlation across some of the original variables.

The PCA technique proceeds through the following steps:

- the data is arranged in a matrix and the correlation matrix is calculated;
- the original data are rotated to a new orientation, with the same dimensionality, such that the dimensions (or components) are mutually orthogonal with sequentially decreasing variance;
- the transformed space is reduced, usually by removing the dimensions displaying the smallest amount of variance;
- the reduced space is then transformed to make the retained components more interpretable and thus, a substantive analysis can be performed on the new dimensions.

Since the derived components are linear composites of the original variables, it is possible to easily reconstruct the original data exactly, or approximate it by removing the components responsible for "noise" in the data.

3.2 Method

In the discussion that follows, the basic principles of PCA are highlighted. For an in depth treatment of PCA consult Green and Carroll (1978).

3.2.1 Factor Analysis

Consider a matrix of data, X, with dimensions $m \times n$, where m is the number of measurements made of n variables. This matrix would be in the following form:

$$X = \begin{pmatrix} x_{1,1} & x_{1,2} & \dots & x_{1,n} \\ x_{2,1} & x_{2,2} & \dots & x_{2,n} \\ \vdots & \vdots & \ddots & \vdots \\ x_{m,1} & x_{m,2} & \dots & x_{m,n} \end{pmatrix}$$

Each row of the data matrix is standardised by subtracting the mean, then dividing by the standard deviation. The correlation matrix, which is a measure of the correlation between each variable, is related to X by

$$R = \frac{1}{m-1} X'X \tag{3.1}$$

The singular value decomposition of the correlation matrix reduces it to the product of three matrices,

$$R = U D\, U' \tag{3.2}$$

where U is the matrix of eigenvectors of R and D is a diagonal matrix of the ordered eigenvalues of R. The new axes of the rotated data are then given by

$$Z = XU. \tag{3.3}$$

The columns of Z are the principal component scores. The direction cosines that form the rotation of X are given by U. The variances of the point projections along the new axes are given by the values of D. It is convenient to work with the component scores when they have been scaled to have variances equal to unity. The scaling is then given by

$$Z = XUD^{-1/2}. \tag{3.4}$$

The component loadings, which express the correlation between each original variable and the principal components, are given by

$$F = UD^{1/2} \tag{3.5}$$

The decomposition of the standardised data matrix is reversible: it is possible to reconstruct the original standardised data from the components and loadings. As the components are arranged in order of sequentially decreasing variance, it is also possible to produce an approximation to the original data by neglecting the components with smaller variance, thus producing a noise-free approximation to the standardised data. The standardised data is reconstructed from (3.4) and (3.5) by

$$X = ZF'. \tag{3.6}$$

3.2.2 Reduction of Dimension

One of the primary purposes of PCA is reduction of dimensionality. PCA has already provided an ordered set of principal components, each mutually orthogonal and with sequentially decreasing variance. Thus, the components accounting for the greatest variance are ranked higher than the less important components. However, one must now decide where the cut-off of most important components lies. There are various statistical and graphical methods available to determine how many components to retain. Only a few mechanical procedures are discussed here, a more detailed description can be found in Green and Carroll (1978).

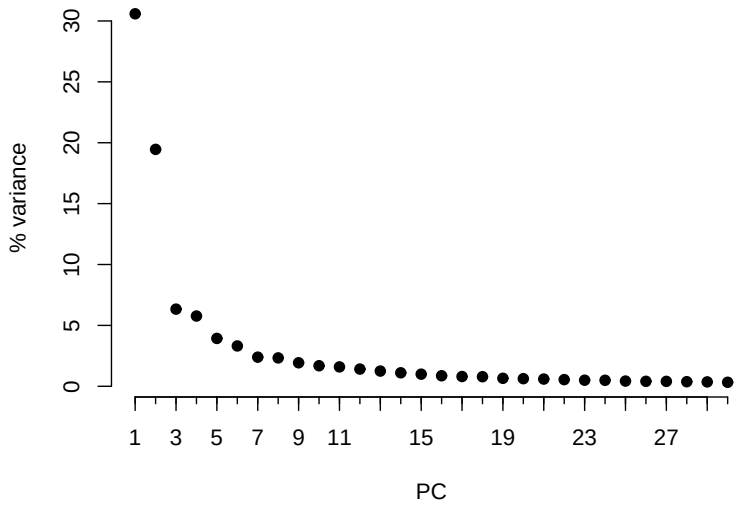

Figure 3.1: Example of a scree test. The elbow in the graph is between 3 and 9.

The most widely utilised method is to retain only components whose eigenvalues are greater than a threshold value. This is often set to unity. However, it is possible to retain more than the appropriate number of eigenvalues with this method.

The next method, termed the scree test, looks for an elbow in the graph of variance as a function of principal component rank. The position of the elbow should indicate the number of significant components to retain. This method has a rather high degree of subjectivity as very often a clear elbow is not present, even if a large number of components are retained. An example of a scree test plot is given in Figure 3.1. This figure also illustrates the difficulty in determining the precise position of the elbow. In this case, it is somewhere between 3 and 9.

A more intuitive method is to retain all components that account, on a cumulative basis, for a specified proportion of the total variance. Even if the neglected components are statistically significant, they just may not be important enough to consider.

These methods are heuristic guides and require a large degree of judgment when applied. Many of the statistical tests are not useful for large sample sizes, as too many components are statistically significant. When reduction is performed to increase the interpretability of the analysis, it may be necessary to retain fewer components than are statistically significant. Therefore it is often more useful to apply a combination of these methods to determine the number of components to retain.

3.2.3 Varimax Rotation

A further step in factor analysis that can be taken is to determine an orientation of the component loading solution which is more interpretable. The initial solution of a PCA has the tendency to produce a first general component on which the majority of the variables are strongly correlated. The loadings of the following components then tend to exhibit a bipolar structure, with variables either being positively or negatively correlated. A more interpretable solution is an orientation where one component is strongly correlated with only a few variables.

It is necessary to ask if further transformations of the component solution are permissible? The matrices fundamental to PCA, the standardised component loadings and scores given by (3.4) and (3.5), are used to reproduce X, using (3.6), assuming that all components are retained. What needs to be determined is if X remains unchanged if certain transformations are applied to Z and

F. Applying a nonsingular transformation T to Z

$$Z \rightarrow ZT$$

requires a companion transformation of F so that X is not affected. This transformation is

$$F \rightarrow F(T')^{-1}$$

Computing the product of ZT and the transpose of $F(T')^{-1}$, X is once again obtained.

$$\begin{aligned} X &= (ZT)[F(T')^{-1}]' \\ &= ZF' \end{aligned}$$

The correlation matrix, R, can be represented as the major product moment of F.

$$R = FF' \tag{3.7}$$

The question remains if this is affected by a transformation of F. Consider J to be an orthonormal, but arbitrary matrix, by which F is postmultiplied.

$$FJ$$

The major product moment of FJ is then

$$\begin{aligned} (FJ)(FJ)' &= FJ'JF' \\ &= FF' \end{aligned}$$

since $J'J = JJ' = I$. Thus, neither X nor R are affected by transformations of Z and F and the problem now becomes one of finding an orthonormal matrix J that makes the rotated loadings FJ more interpretable.

The most popular approach to finding such a matrix is based on the principles of simple structure. A loading matrix that exhibits simple structure has the following properties:

- the majority of loadings on any component are small, with only a few loadings being large;
- each variable is strongly correlated with only a few components;
- each component is unique.

The problem is then to find a transformation matrix that when applied to the loading matrix produces a matrix with these properties.

Varimax rotation is one such procedure that searches for simple structure. It looks for $G = FJ$, where G exhibits simple structure. Varimax works by maximising the variance of the squared loadings. The computation proceeds through a number of iterations until the criterion being maximised does not change significantly between iterations.

The standardised factor scores, Z, are computed in this new orientation by

$$Z = XG(G'G)^{-1} \tag{3.8}$$

Most computer implementations do not supply the applied rotation matrix, but it can be calculated with $J = F'G$.

In the new rotated solution, the variance maximising properties of the PCA are lost. The total variance accounted for by the retained components remains unchanged, but the distribution of that variance over the components is no longer the same. Factor rotations that search for simple structure tend to produce components over which the variance is fairly evenly distributed. Thus the first dimension does not necessarily account for the largest proportion of the variance.

3.3 Application to Narrowband Data

PCA was applied to narrowband data by considering each day of amplitude data to be a separate variable. In terms of the data matrix, X, this means that each day of data forms a column in the matrix. The component scores and loadings were then calculated. By applying the methods discussed in Section 3.2.2, the number of components were reduced and then each day of data was reconstructed without the higher order, noisy components, which consisted of only a small portion of the total variance. The residuals between the original data and the reconstructed data were then examined for signatures of transient events. A Varimax rotation was later applied to the reduced-space principal components to improve the interpretability of the components.

Chapter 4

Results

4.1 Principal Components and Loadings

Narrowband data recorded by an UltraMSK receiver in Tihany, Hungary were analysed using PCA. UltraMSK records the amplitude and phase of signals from VLF transmitters, which use Minimum-Shift Keying (MSK) modulation. Data covering a considerable length of time were available from two transmitters. However, only the amplitude data was used in this analysis as the phase data was not sufficiently stable over the period of the data sets. Thus, as there was no consistent pattern from day to day, the use of PCA to analyse the phase data was not possible. The first transmitter, operating at a frequency of 19.6 kHz with call sign GBZ, is located in Anthorn, UK (54.911° N, 3.278° W). The signal path from GBZ to Tihany is west to east with path length 1720 km. Data were available from 26 May 2007 until 14 June 2009. Unfortunately, due to operational problems, some data were not usable and had to be neglected. As a result, 553 days of data were used in the PCA. The data were first smoothed by calculating the running median between data points and then sub-sampled by selecting every thousandth data point. This resulted in 1728 data points per day, or 1 data point every 50 s. This resolution allows for the reduction of the computation time required, while still being fine enough to detect the shorter transient events. Although the timescales of these events are much shorter than this resolution, the relaxation time of the ionosphere at the altitudes affected by these events is of the order of 200 s.

The second transmitter used operates at 45.9 kHz, with call sign NSY. It is located in Niscemi, Italy (37.126° N, 14.436° E). Data from this transmitter were available from 25 July 2008 to 11 June 2009, although only 197 days of data were used in the analysis.

4.1.1 GBZ, 19.6 kHz Transmitter

The amplitude of GBZ undergoes considerable changes on both diurnal and seasonal time scales. Figure 4.1 shows the typical signal strength profiles for each season, where the red and blue lines represent the High and Low components of the UltraMSK signal. The average of these was used in the PCA. A plot of annual signal strength variation, seen in Figure 4.2, highlights a number of characteristics of the signal variation at a glance. A similar figure was presented by Reuveni and Price (2009), who used it to show the effect of the 27 day solar cycle. The dashed lines on the plot show the sunrise and sunset times for the receiver location, at an altitude of 100 km, while the solid line shows the same for the transmitter. The signal strength varies diurnally, with night time transmission being stronger than day time transmission. There is a transition region around dawn and dusk, where the signal power drops. The dawn transition is usually more definite than the dusk transition, with a larger drop during winter than during summer. The annual variation shows a characteristic hour glass shape.

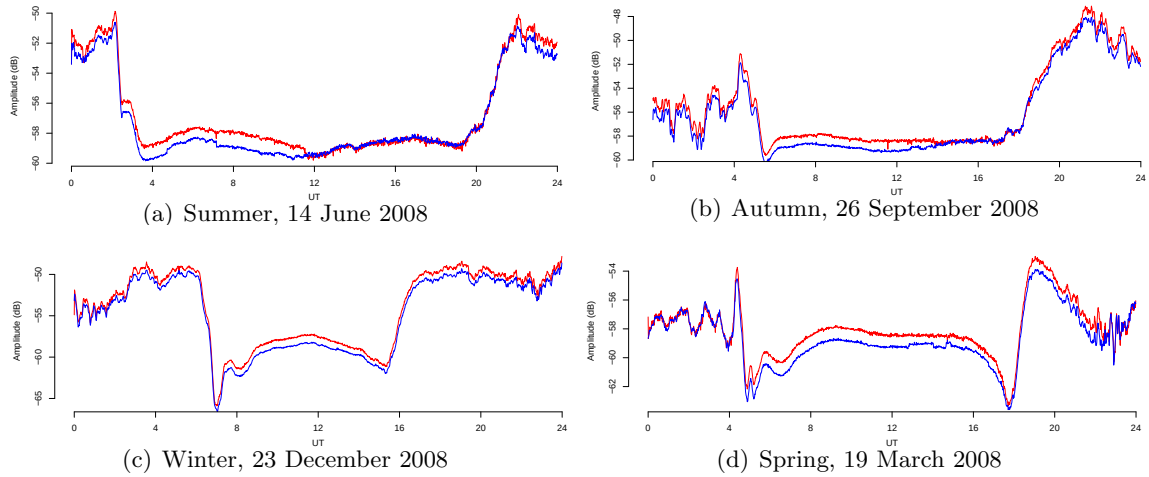

(a) Summer, 14 June 2008

(b) Autumn, 26 September 2008

(c) Winter, 23 December 2008

(d) Spring, 19 March 2008

Figure 4.1: Typical seasonal variation of amplitude of GBZ. Note, the amplitude is measured in dB above an arbitrary reference level.

As the data set spans more than 1 year, the data were averaged over day number in Figure 4.2. However, even with the averaging, there are periods with both very high and very low amplitude signals. These were caused by periods in June 2007 and September 2007 where the signal was abnormally strong and abnormally weak, respectively. As this was more likely to be caused by a change in either the transmitter or receiver than the ionosphere, these periods were neglected in the PCA. Figure 4.2 shows only signals in the range -70 to -40 dB. Apart from the periods of abnormal operation already mentioned, there are days with white sections where the signal strength exceeds the plot limits. This usually occurred on days where the transmitter was inoperational for a few hours and the signal dropped to the noise floor. These days were neglected in the PCA.

The variations illustrated in Figure 4.2 can be quantified more precisely by analysing the results from the PCA. These results are summarised in Table 4.1.1, which gives the eigenvalues, variances and summed variance for the first 10 principal components. From this it is seen that the first principal component accounts for 60.87% of the variance in the data set, with the second, third and fourth accounting for 16.31%, 7.26% and 3.79% respectively. As they collectively account for 88% of the variance in the data, the first four principal components should express the main variations in the signal.

Figure 4.3 shows the variance for each principal component. It is clear that the first ten components account for the majority of the variance in the data set. Note that there is no clearly defined elbow in this graph.

The first principal component (PC 1) is shown in Figure 4.4(a). It is evident that this represents the general diurnal variation of the signal amplitude, although the length of the daylight depression implies that it is more representative of winter than summer months. This becomes more apparent when one looks at the correlation with this component with each variable in Figure 4.4(b). Although the large majority of variables are strongly positively correlated with PC 1, the summer months are not as strongly correlated as the winter months. The lower correlations during summer occur when there is less variation between day and night signal amplitude.

The second principal component (PC 2) is slightly more complicated. Figure 4.5 shows the signal and its loadings. PC 2 has significant power peaks at approximately 05:00 and 18:00 UT. The loadings exhibit an annual variation. During times where the variables are positively correlated with PC 2, namely the northern hemisphere winter, addition of this component to

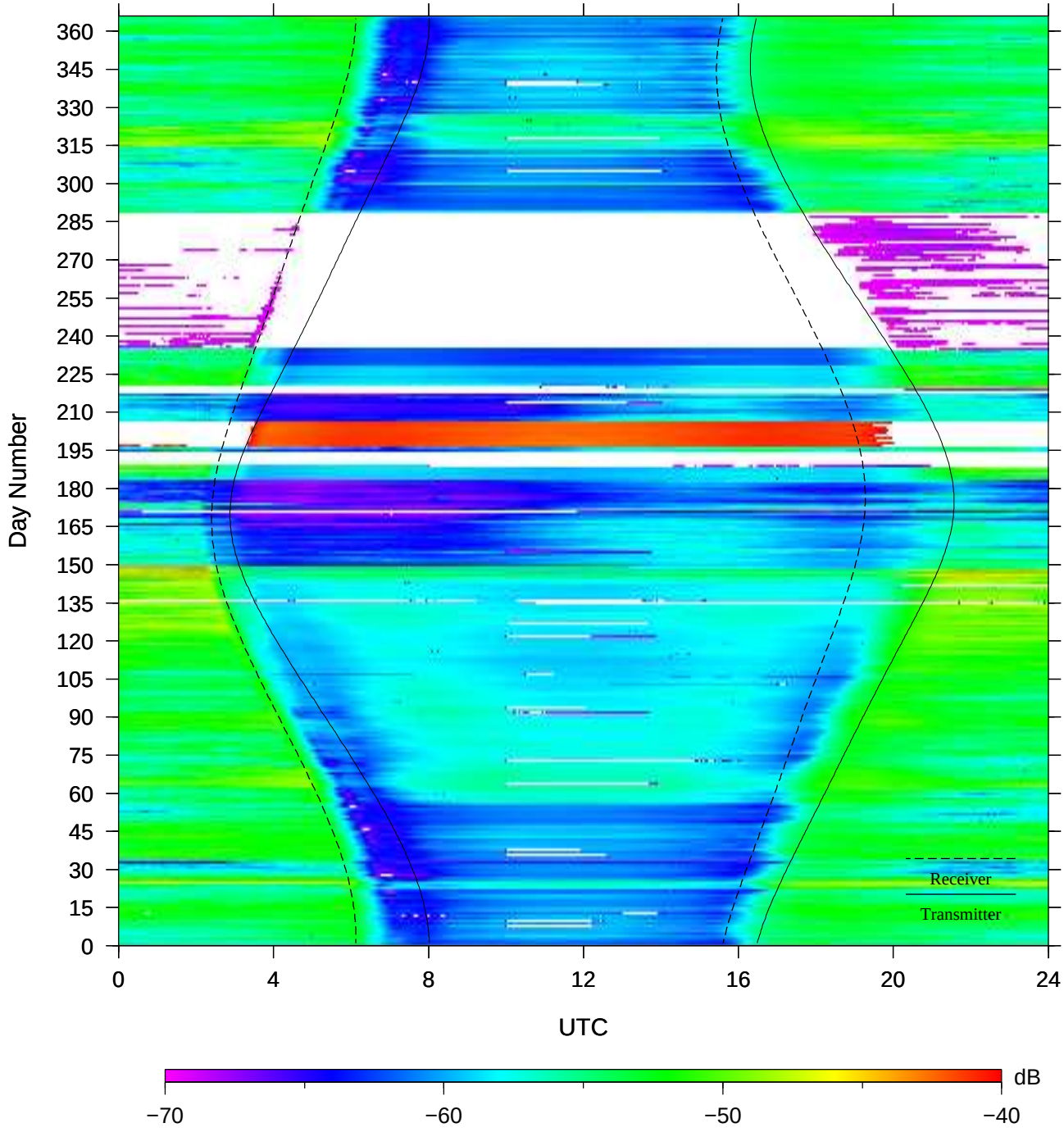

Figure 4.2: Annual signal strength variation for GBZ, 19.6 kHz. This is averaged over the period 26 May 2007 to 14 June 2009.

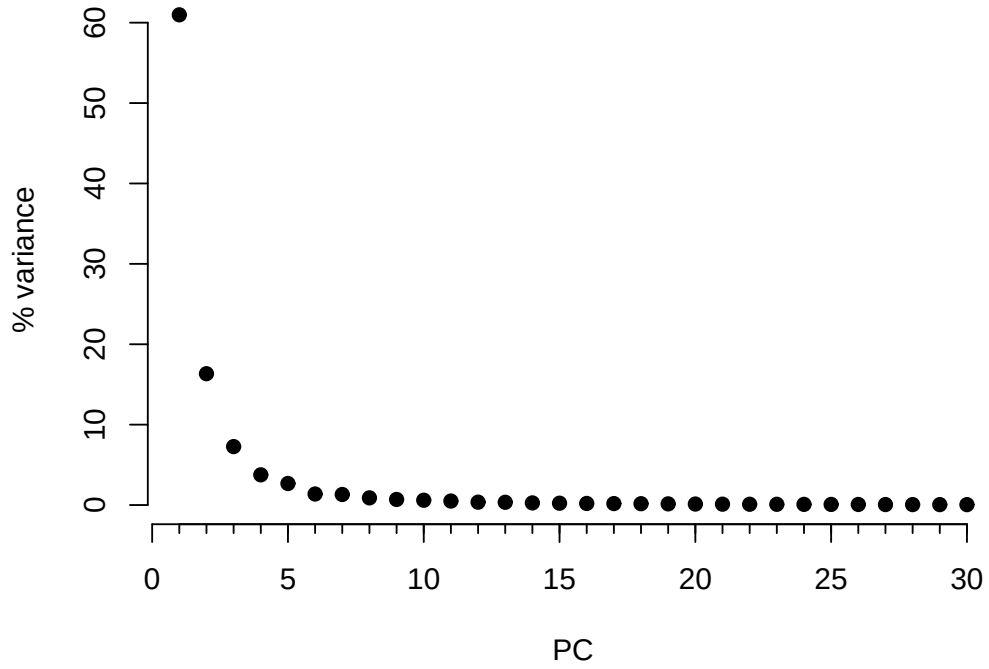

Figure 4.3: Variances accounted for by the principal components of GBZ.

the first has the effect of steepening the transitions between night and daytime conditions. The summer months are negatively correlated with PC 2, hence the addition of the inverse of the component is appropriate. This has the effect of lengthening the daytime depression of signal amplitude by pushing back the dawn and dusk transitions.

The next principal component (PC 3), shown in Figure 4.6(a), has dipolar signatures at dawn and dusk. The loadings, displayed in Figure 4.6(b), show a semi-annual variation, with positive correlations over the solstices and negative correlations over the equinoxes. This component has the effect of steepening the dawn and dusk transitions during the equinoxes, as well as producing a deep depression during these times. The opposite is true for the solstices, where this component levels out any small depressions created by PC 2 during sunrise and sunset.

Figure 4.7 shows the fourth principal component. The correlations appear to have no annual

Table 4.1: First 10 principal components of GBZ.

PC	Eigenvalue	Variance (%)	Summed Variance (%)
1	336.63	60.87	60.87
2	90.18	16.31	77.18
3	40.16	7.26	84.44
4	20.95	3.79	88.23
5	14.89	2.69	90.93
6	7.85	1.42	92.35
7	7.26	1.31	93.66
8	4.99	0.90	94.56
9	3.85	0.70	95.26
10	3.30	0.60	95.85

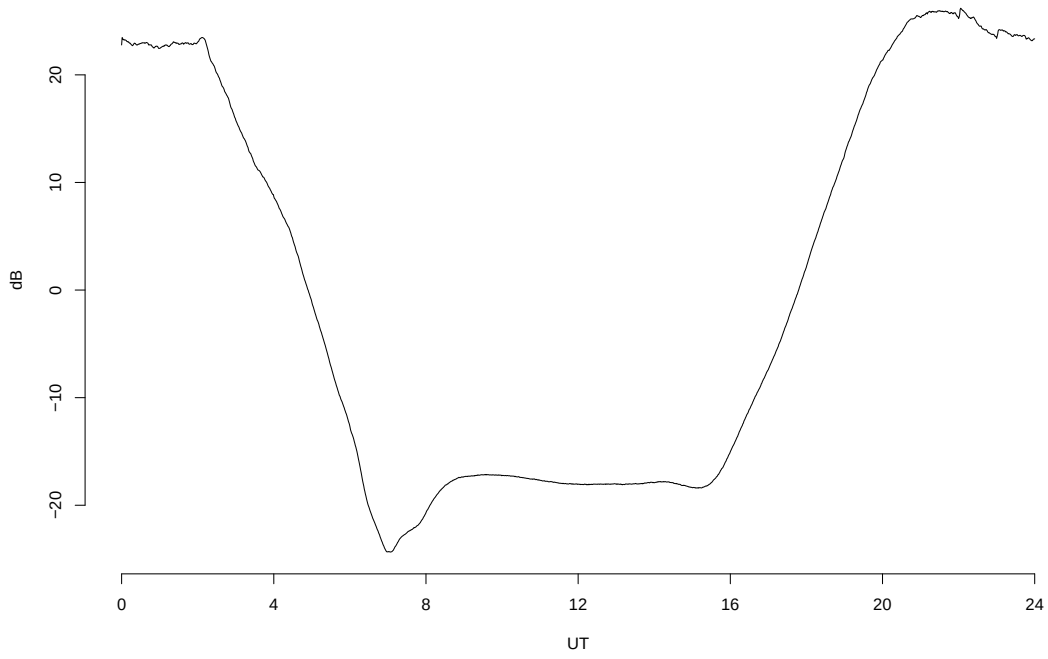

(a) PC 1

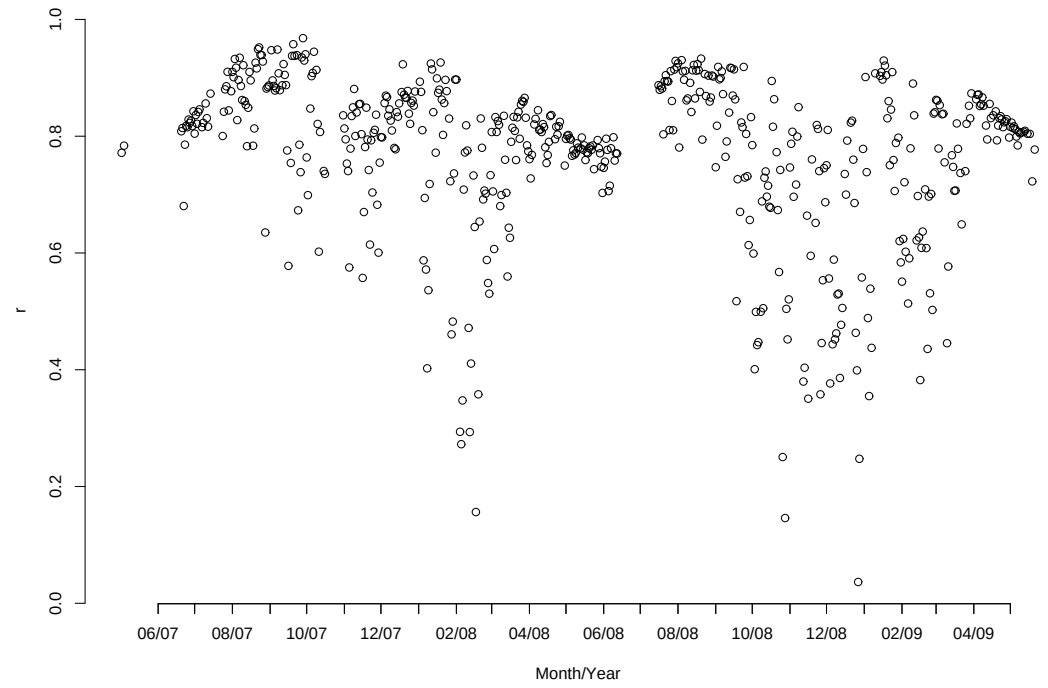

(b) Loadings of PC 1

Figure 4.4: First principal component signal and loadings for GBZ.

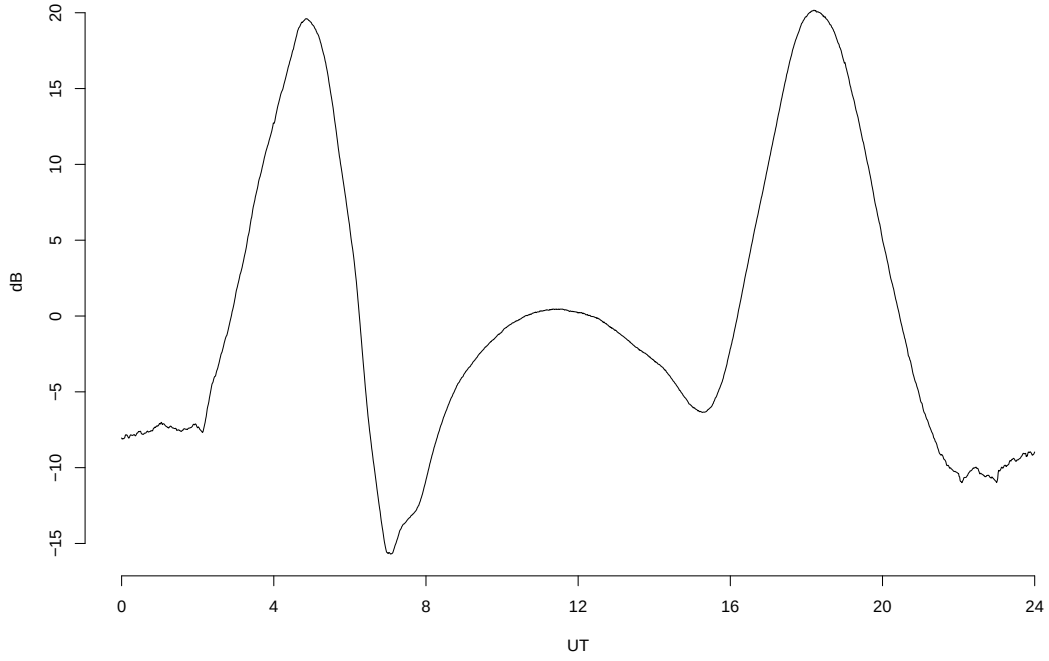

(a) PC 2

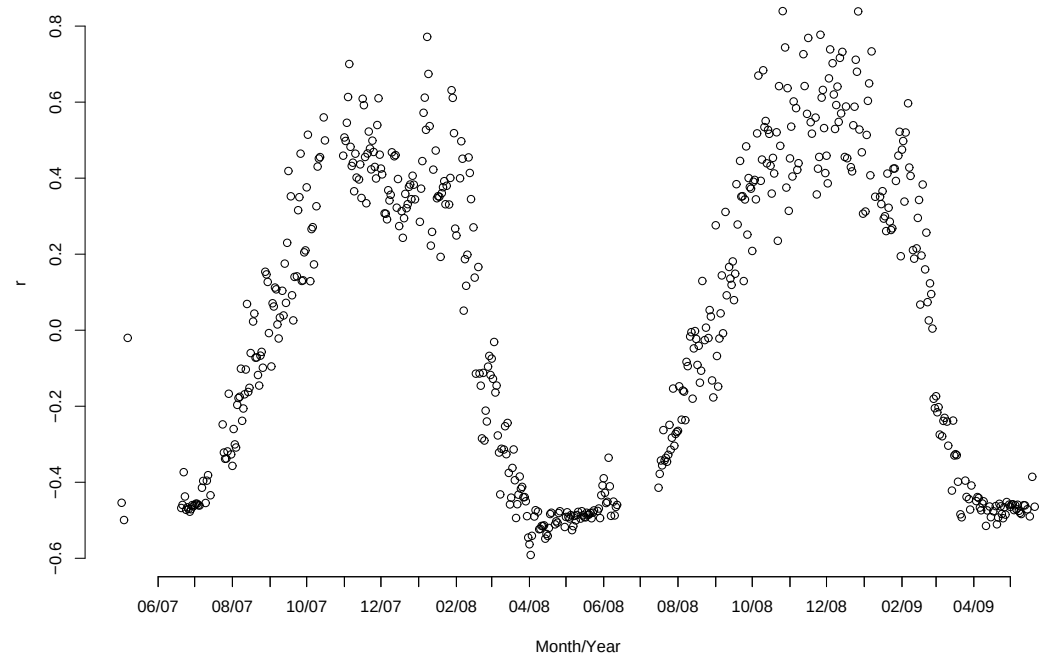

(b) Loadings of PC 2

Figure 4.5: Second principal component signal and loadings for GBZ.

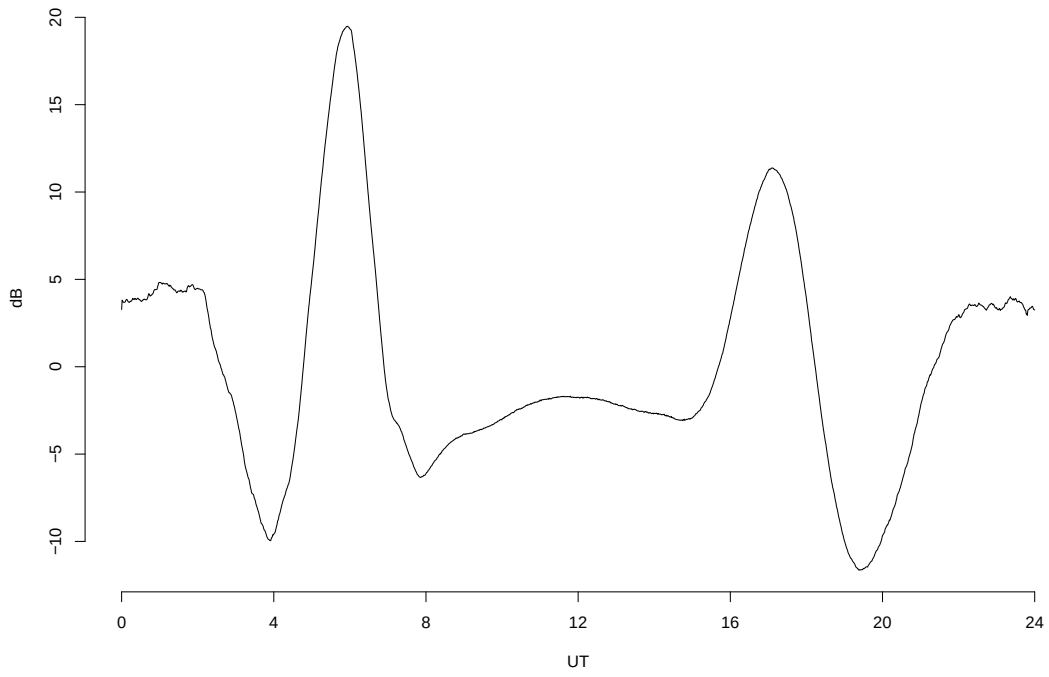

(a) PC 3

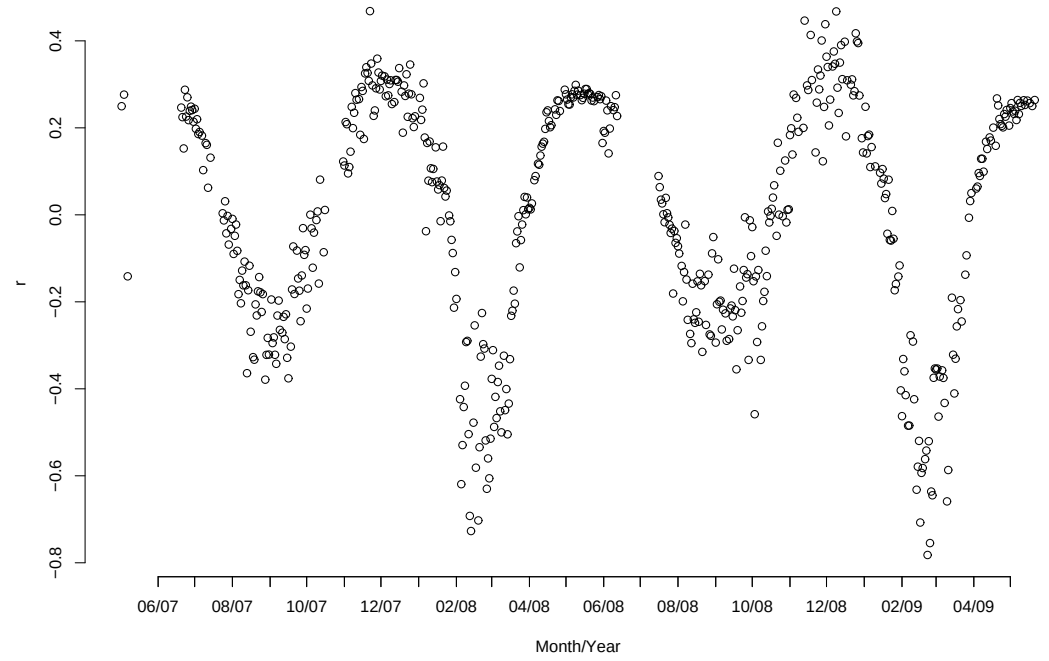

(b) Loadings of PC 3

Figure 4.6: Third principal component signal and loadings for GBZ.

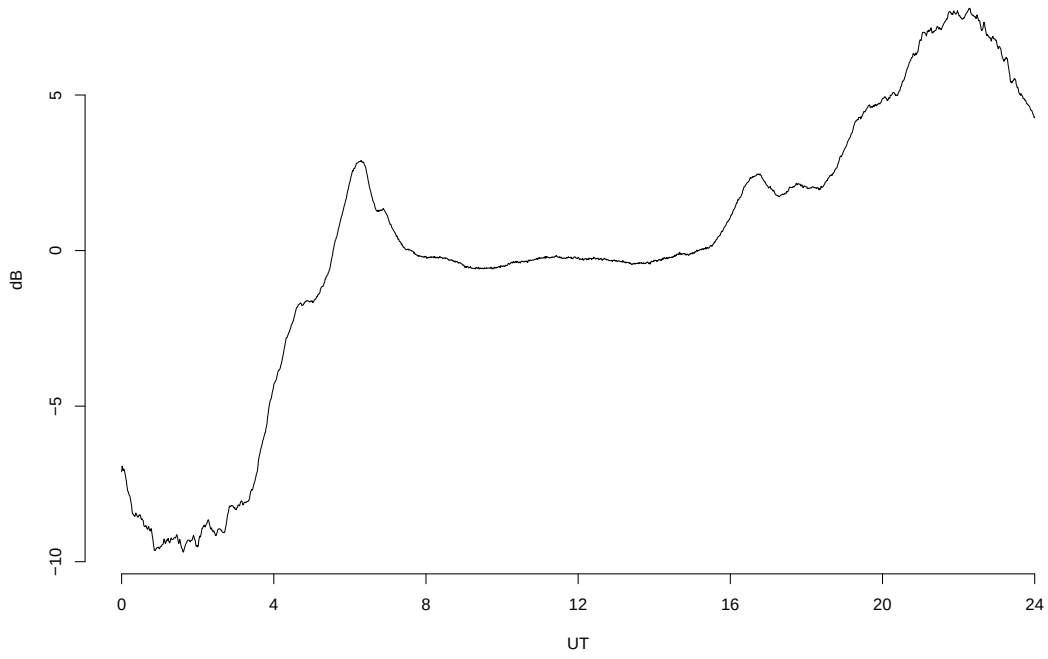

(a) PC 4

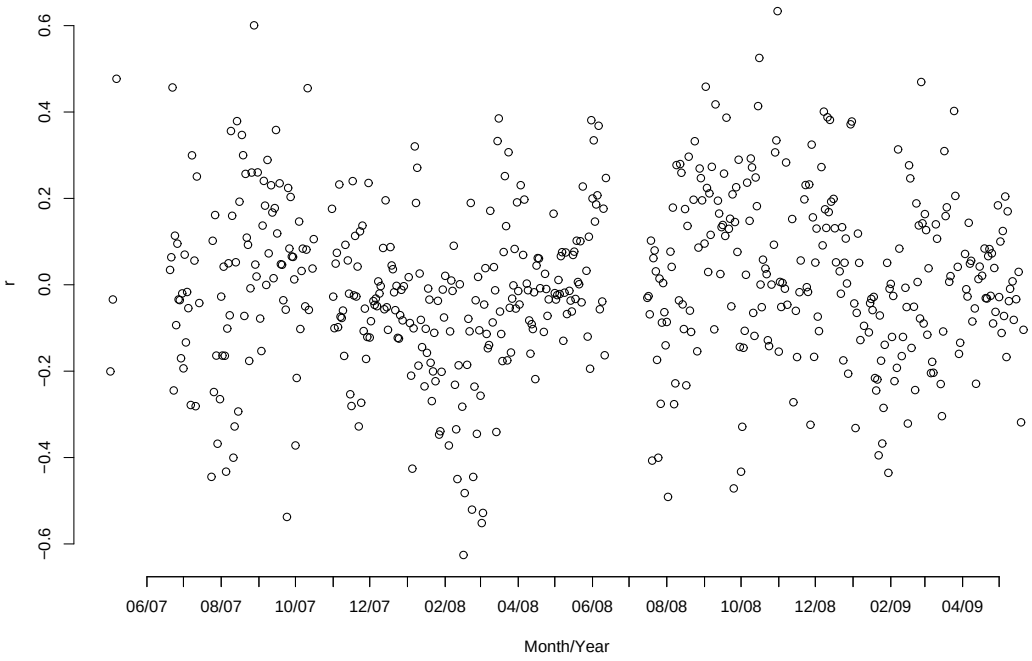

(b) Loadings of PC 4

Figure 4.7: Fourth principal component signal and loadings for GBZ.

variation and are seemingly randomly distributed. This component lowers the signal strength of the nighttime transmission prior to dawn with respect to that after dusk. It also has the effect of smoothing out the dusk terminator passage and increasing the definition of the dawn terminator passage, as seen in Figure 4.2. Thus the dawn terminator is much more well defined than the dusk terminator.

Further components become increasingly difficult to analyse, as they become more complex and their correlations vary more erratically during the year. Therefore they are representative less of general patterns and more of specific patterns pertaining to particular days.

4.1.2 NSY, 45.9 kHz Transmitter

The signal path from NSY to Tihany is north–south oriented with a length of 1124 km. Due to the different orientation and higher frequency than GBZ, the annual variation of signal strength of NSY is considerably different. Typical profiles of the signal strength for each season appear in Figure 4.8.

The annual and diurnal variations of signal strength are presented in Figure 4.9. The sections of white represent bad or missing data. NSY appears to be more operationally stable than GBZ. The diurnal variation of signal strength is clearly seen, with the nighttime signal being much stronger than the daytime signal. Once again, the sunrise and sunset times at 100 km altitude above the transmitter and receiver are indicated by the solid and dashed curves respectively. Unlike with the GBZ–Tihany path, these cross over at some point during the northern hemisphere spring and again in autumn. The passage of the dawn and dusk terminator produces pronounced dips in signal power. The dawn transition tends to consist of two distinct drops in power, with a separation of about two hours between them. The later power drop is not present throughout the year, seemingly absent during summer. The dusk terminator produces a singular power dip, which jumps between earlier and later times at approximately the same time of year as when the sunset times for the transmitter and receiver cross. These drops in power are due to mode conversion in the waveguide propagation as the sunrises or sets. Similarly to the GBZ–Tihany path, the dawn transition is more sharply defined than the dusk transition.

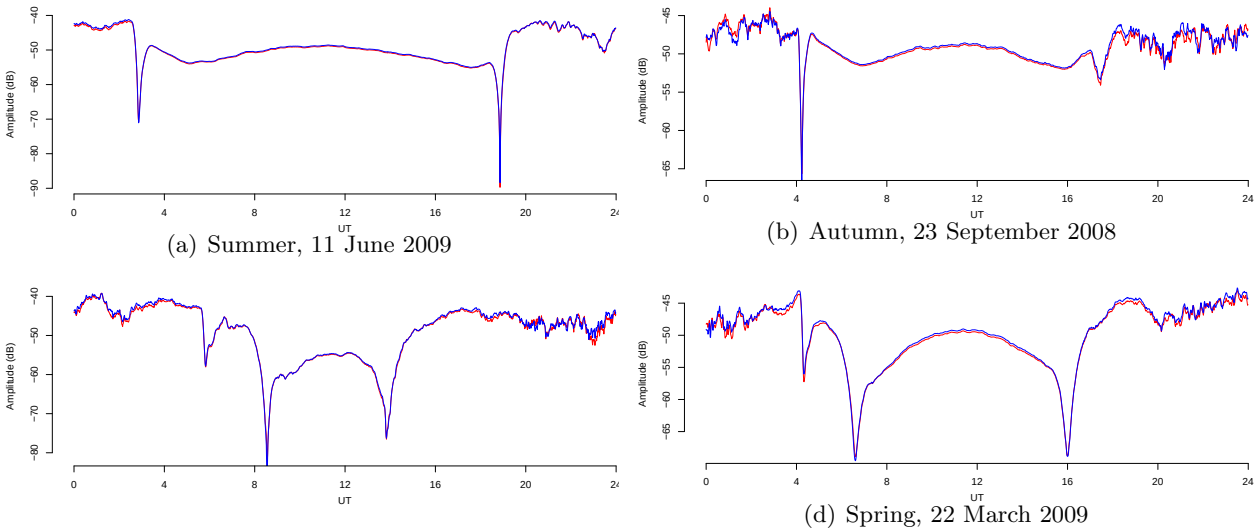

(a) Summer, 11 June 2009

(b) Autumn, 23 September 2008

(c) Winter, 20 December 2008

(d) Spring, 22 March 2009

Figure 4.8: Typical seasonal variation of amplitude of NSY. Note, the amplitude is measured in dB above an arbitrary reference level.

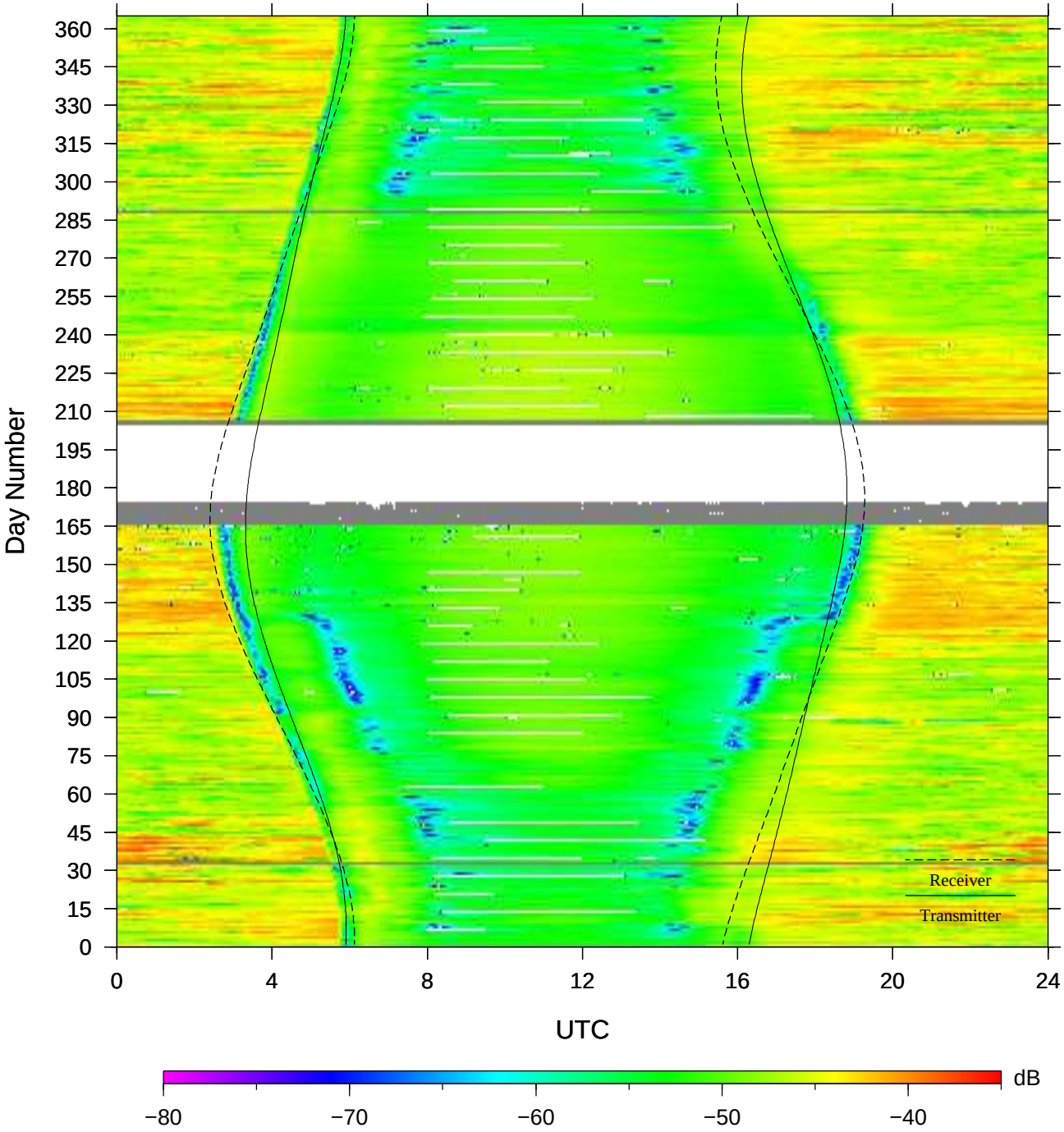

Figure 4.9: Annual signal strength variation for NSY, 45.9 kHz.

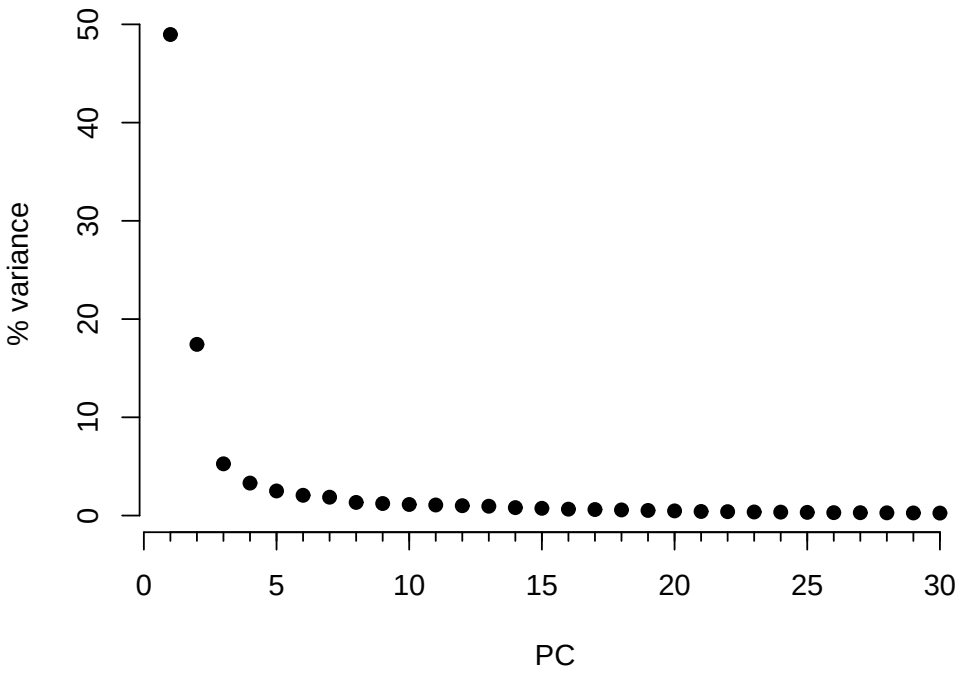

Figure 4.10: Variances accounted for by the principal components of NSY.

The variations of this signal are even more complex than that of GBZ, thus being an excellent candidate for PCA. The results from the PCA appear in Table 4.1.2. The first principal component accounts for 48.97% of the variance, less than the first principal component for GBZ. The second, third and fourth components account for 17.43%, 5.27% and 3.30% of the variance respectively. Together, they account for 75% of the total variance in the data. Figure 4.10 shows the variance for each principal component. The first ten components seem to account for the major part of the variance in the data set.

Figure 4.11(a) shows the first principal component (PC 1), with the loadings in Figure 4.11(b). This component expresses the general diurnal variation of the NSY signal strength. As seen from the component loadings, it is more indicative of the signal during the northern hemisphere winter, with the daylight hours being short and the two dips in signal power during sunrise. The difference in signal strength between day and night is also quite high.

Table 4.2: First 10 principal components of NSY.

PC	Eigenvalue	Variance (%)	Summed Variance (%)
1	96.47	48.97	48.97
2	34.33	17.43	66.39
3	10.38	5.27	71.66
4	6.51	3.30	74.96
5	4.93	2.50	77.47
6	4.06	2.06	79.53
7	3.68	1.87	81.40
8	2.63	1.34	82.74
9	2.41	1.23	83.96
10	2.22	1.13	85.09

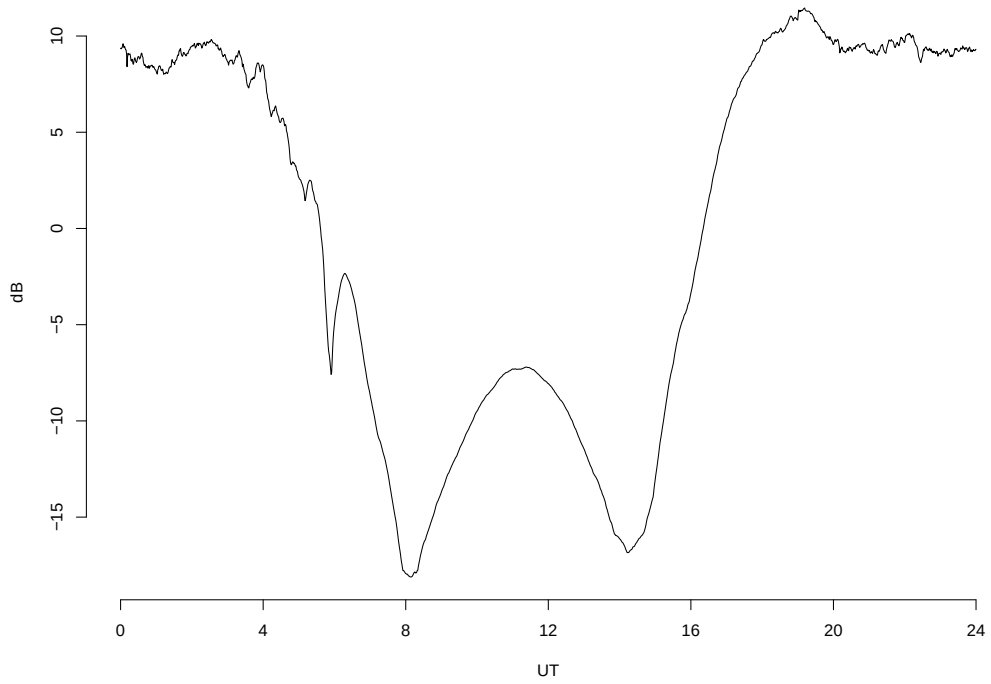

(a) PC 1

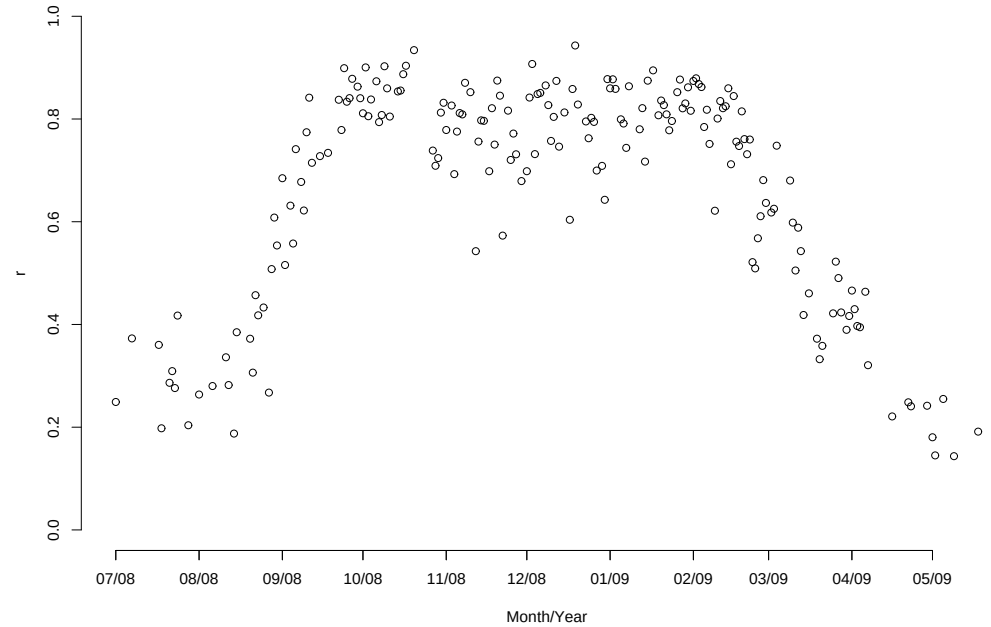

(b) Loadings of PC 1

Figure 4.11: First principal component signal and loadings for NSY.

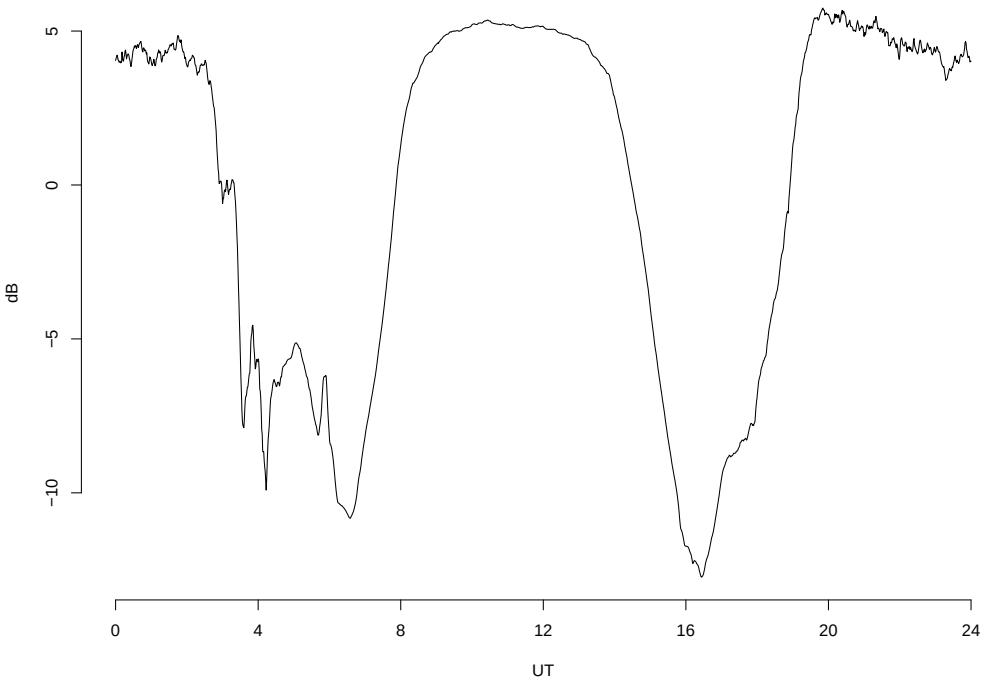

(a) PC 2

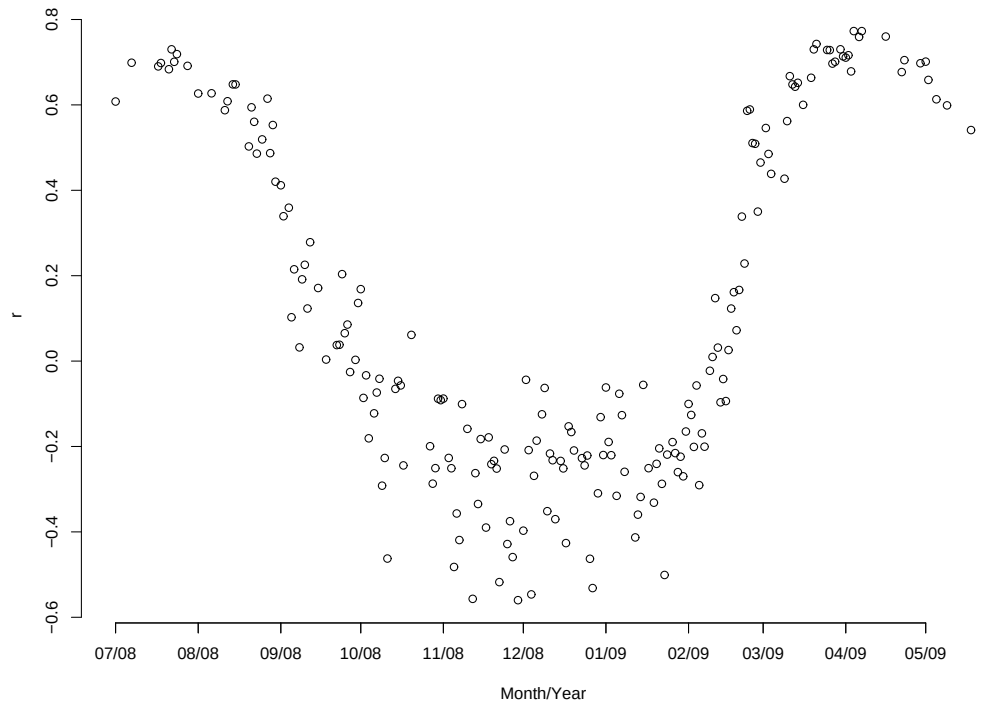

(b) Loadings for PC 2

Figure 4.12: Second principal component signal and loadings for NSY.

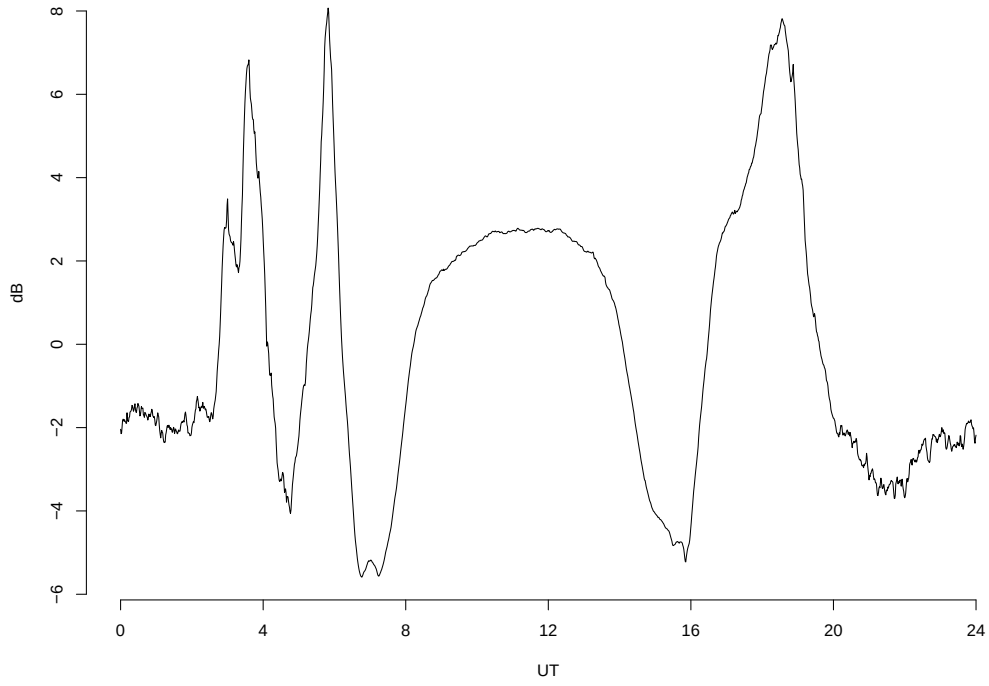

(a) PC 3

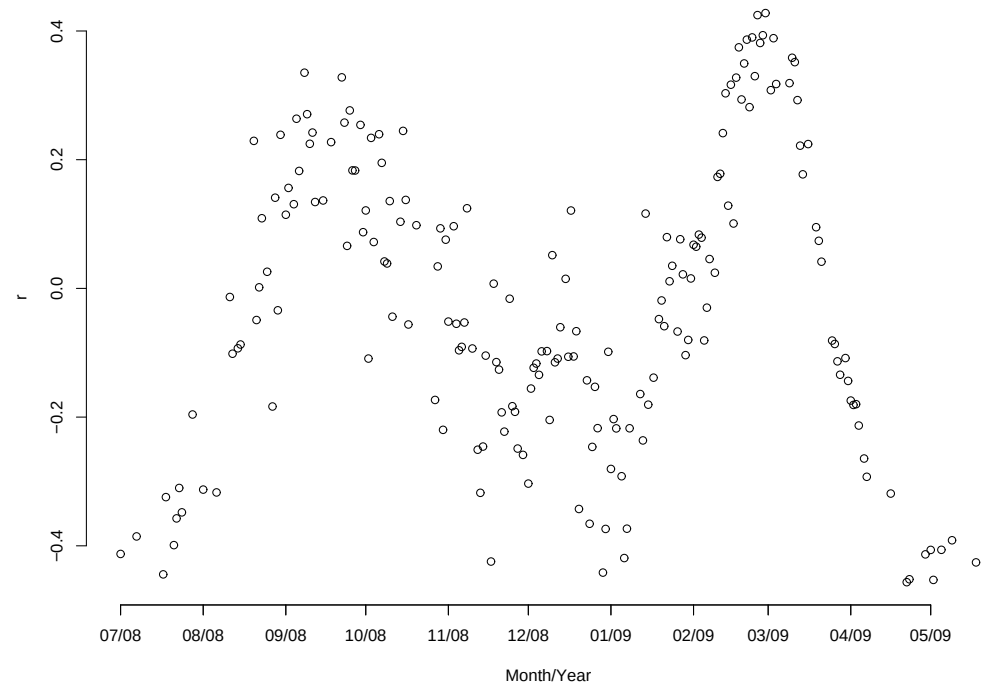

(b) Loadings of PC 3

Figure 4.13: Third principal component signal and loadings for NSY.

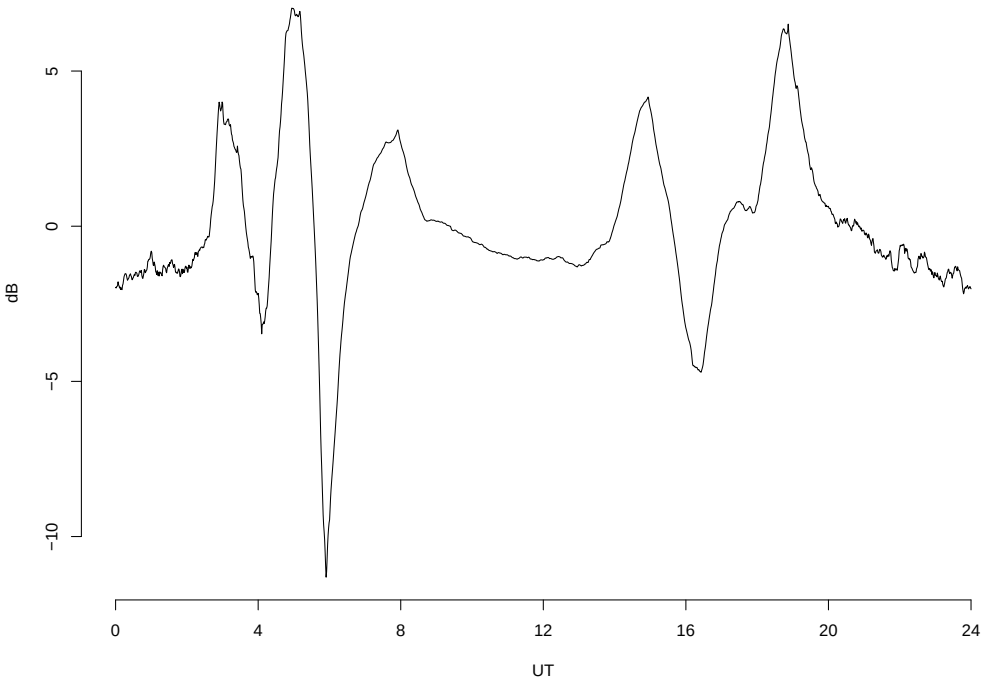

(a) PC 4

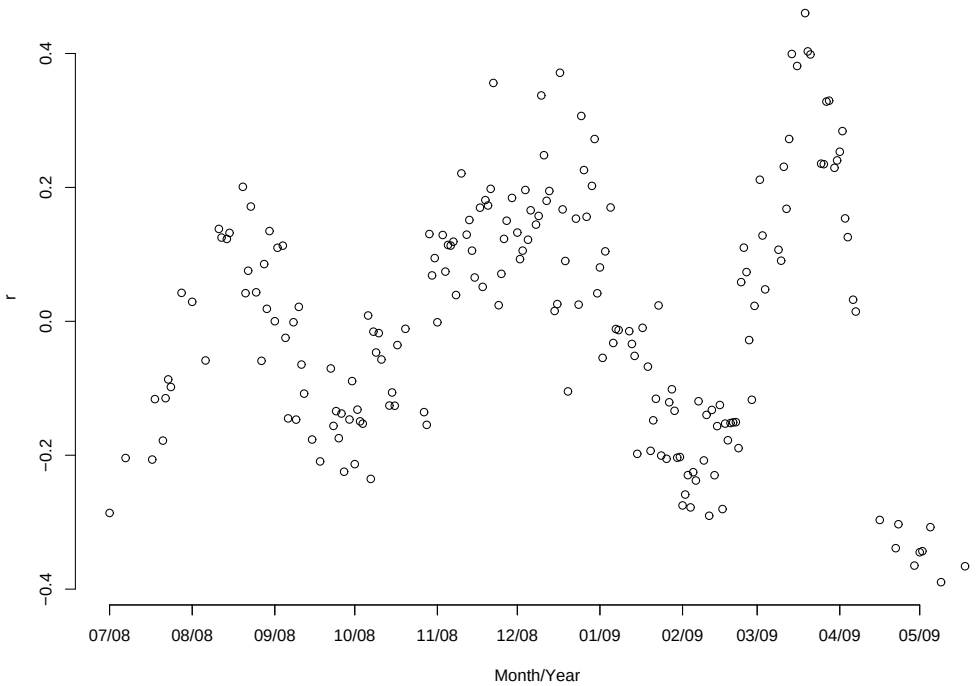

(b) Loadings of PC 4

Figure 4.14: Fourth principal component signal and loadings for NSY.

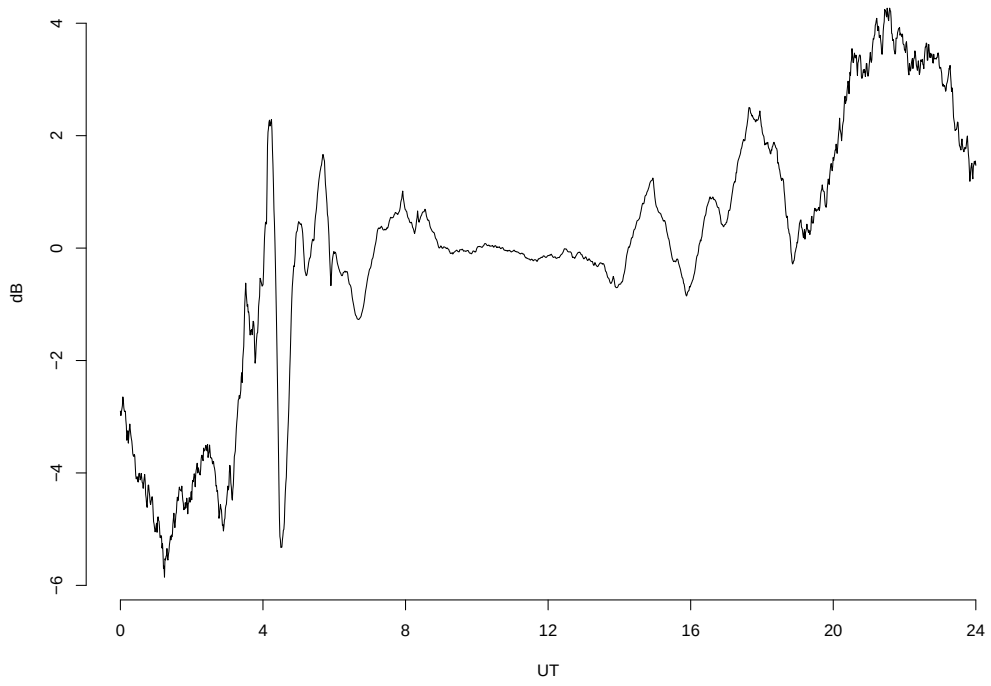

(a) PC 5

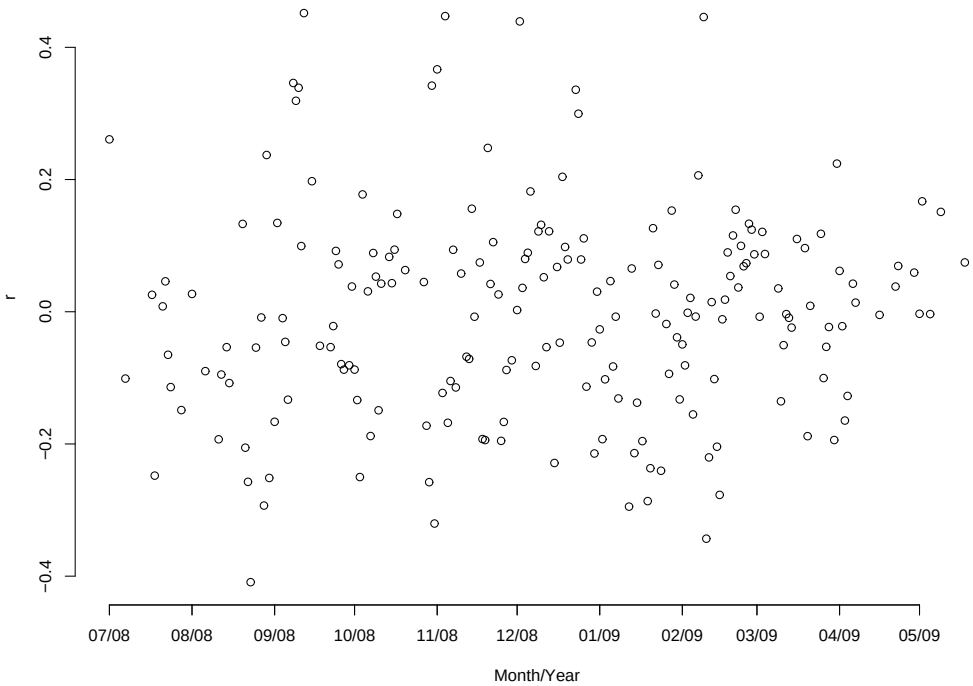

(b) Loadings of PC 5

Figure 4.15: Fifth principal component signal and loadings for NSY.

Although all the original variables are positively correlated with PC 1, the correlations show a clear annual variation, with the difference between the summer and winter months quite large. This is quite unlike the correlations of PC 1 for GBZ, which were all quite strongly correlated, with smaller variations between summer and winter.

The second principal component (PC 2) has an annual variation in the correlations with the original variables. Figure 4.12 shows that PC 2 is negatively correlated with the winter months, while having a positive correlation with the summer months. PC 2 has large drops in amplitude around 04:00 UT and 16:00 UT. The first drop extends until 07:00 UT, while the second is brief.

The addition of PC 2 to PC 1 for the summer months has the effect of increasing the signal strength of the daytime transmission, as well as broadening the length of the day. It also removes, to a certain extent, the first dip in the power during the dawn terminator passage. The winter months, being anticorrelated with PC 2, require the addition of the inverse of the signal. This results in a decrease in the daytime signal strength and a steepening of the dawn and dusk terminator passages. PC 2 also accentuates the initial dip in power during the dawn transition.

Figures 4.13 and 4.14 show the components and loadings for the third and fourth principal components. PC 3 has a semiannual variation in the loadings, with positive correlations around the equinoxes and negative correlations during solstices. This component affects the shape of the dawn and dusk terminator passages, either steepening or smoothing depending on the time of year. As is the case for the GBZ PCA results, analysis of further components becomes difficult. PC 4 exhibits a triannual variation in its loadings, while PC 5's loadings are randomly distributed.

4.2 Reconstruction of Data

It is possible to reconstruct the original data, neglecting the lesser components that account for a small amount of variance in the data. This is done by making use of (3.6). As some components are neglected this is now a rank-r approximation of the original data, where r is the number of components retained.

Figures 4.3 and 4.10 were used, along with Figures 4.16 and 4.17, to determine the number of components to retain for the reconstruction of the signal from each transmitter, as per discussion in Section 3.2.2. Figures 4.16 and 4.17 are plots of the logarithm of the eigenvalues of each principal component.

For GBZ, there in no clear elbow in Figure 4.3. Thus, the point where the variances stop dropping significantly between successive components is taken as the cutoff. This occurs subjectively at around PC 6. Figure 4.16 indicates that eigenvalues greater than one occur for components before PC 18. If 95% of the total variance in the data were to be accounted for, then 9 principal components would have to be retained. As each method is highly subjective, the analysis was repeated with differing numbers of retained components. It was seen that the results did not change considerably. The results for 11 components being retained for the reconstruction are shown here.

In the case of NSY, Figure 4.10 has an elbow ending at around PC 5 and all eigenvalues larger than one occur before PC 19. In order to account for 95% of the total variance in the data, 28 components would need to be retained. Once again, the analysis was repeated with differing numbers of components, ranging from 5 to 28, without much change in the results. The results for 18 retained components are presented here.

The amplitude scale in the figures of the recontructions that follow is now different to that shown in Figures 4.1 and 4.8 as the original data were standardised at the start of the PCA.

The top panel in Figure 4.18 shows the original data, after standardisation, recorded from GBZ on 26 December 2007 in red. The blue is the approximation reconstructed from the first 11 principal components, while the dashed line is an approximation derived from Fourier analysis. The PCA reconstruction is a much better approximation to the data than the Fourier analysis. This is due to the fact that the PCA basis functions are determined by the data, while the Fourier

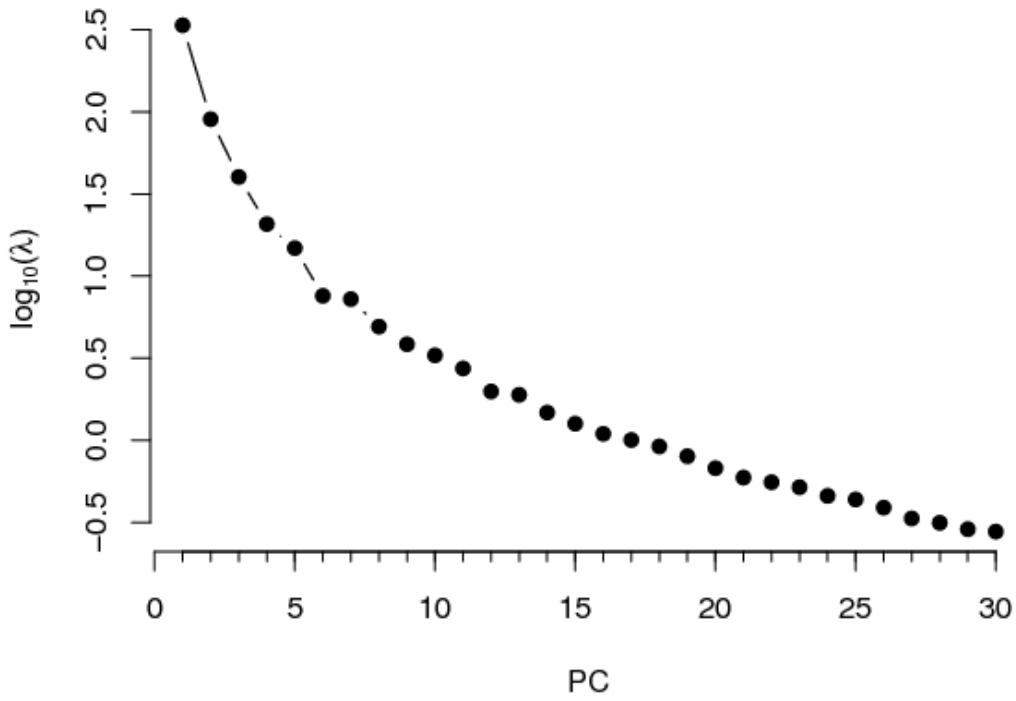

Figure 4.16: Eigenvalues of the leading principal components for GBZ.

analysis is completely general with generic basis functions. The bottom panel is a plot of the residuals between the original data and the PCA reconstruction. It is, effectively, a sum of all the unused components, which constitute the more irregular component of the data.

A similar example for NSY is provided in Figure 4.19, where the data were recorded on 23 April 2009. Once again the PCA performs better than the Fourier reconstruction. The residuals show larger deviations between the original data and the PCA than were seen in the GBZ reconstruction.

4.3 Detection of Transient Events

The residuals between the original data and the reconstruction from the PCA are used to identify transient events, as they represent the difference between the expected and observed data.

4.3.1 Gamma Ray Bursts

The detection of GRBs by satellites is published online at `http://grblog.org`. Tables of localised (their position has been recorded) GRBs from 2003 to 2009 by Stephen Holland are available at `http://lheawww.gsfc.nasa.gov/~sholland/grb/`. The majority of events presented here were identified by NASA's Swift Gamma Ray Burst Mission. Swift was launched into low earth orbit in 2004, at an altitude of 600 km. Experiments onboard are the Burst Alert Telescope (BAT), X-ray Telescope (XRT) and the UV/Optical Telescope (UVOT). BAT provides the initial detection of a GRB, while XRT and UVOT do the follow-up observations (images and spectra) of the afterglows (Gehrels et al., 2004).

A list of the detections of GRBs was compiled for 2007, 2008 and the first part of 2009. This consisted of the date, time and location, given in right ascension and declination, of the detected bursts. These were used to calculate the sub-burst point of each GRB. This is the point on the

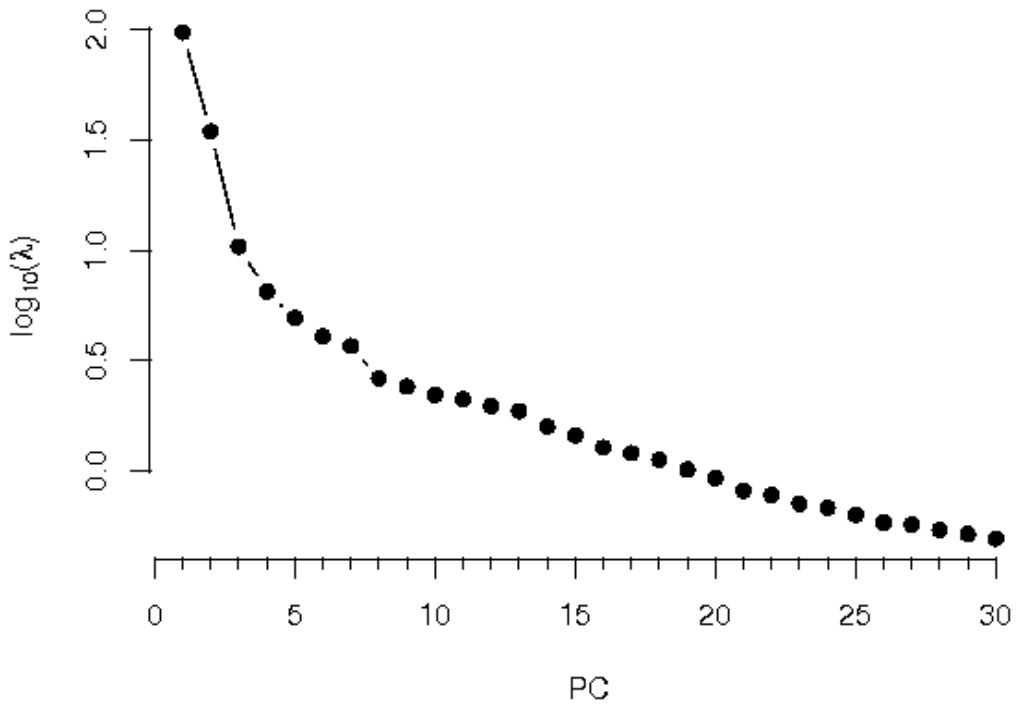

Figure 4.17: Eigenvalues of the leading principal components for NSY.

surface of the Earth, directly below the GRB. The position of the day/night terminator was also calculated at the time of the burst. Maps of events detected were created for the three years. These are shown in Figures 4.20, 4.21 and 4.22.

The increase in the detected number of GRBs between 2007 and 2008 is due to the launch of NASA's Fermi Gamma-ray Space Telescope in June 2008. The distribution of events is random, as expected. GRBs occurring outside the hemisphere of the transmitter-receiver paths were not expected to produce an effect in the propagation conditions of the signal, and were not considered in the initial analysis. Plots of the remaining GRBs with the signal paths and the location of the day/night terminator were created, to locate bursts occurring at nighttime over the paths. Residuals from the PCA reconstruction were then examined for an effect of the GRBs.

The first GRB event presented here is one that has already been mentioned. GRB 080319B, occurred at 06:12:47 UT at RA 14:31:40.98 and Dec $+36°18'08.80''$ (Cummings et al., 2008). This translates to a sub-burst point at 36.3024°N and 307.5489°E. The spatial relationship between the sub-burst point and the signal paths is shown in Figure 4.23. The sub-burst point is over 5700 km from the receiver in Tihany and is in darkness. However, the signals paths are in daylight, making the detection of any effect unlikely, despite the large fluence of this GRB.

Three other events occurred on the same day, with the fourth occurring at 17:05:09 UT at RA 06:37:53.60 and Dec $+23°56'34.20''$ (Ukwatta et al., 2008). GRB 080319D had a duration of 24 s and a fluence of 3.2×10^{-10} Jm^{-2}. The sub-burst point for GRB 080319D was at 23.9427°N and 25.5717°E. Figure 4.24 shows the configuration of the signal paths in relation to the sub-burst point, which is 2644 km from the receiver. Both the GRB and the NSY–Tihany path are in darkness, while the GBZ–Tihany path is mostly in daylight.

Figure 4.25 shows a plot of the signal amplitude from GBZ received on 19 March 2008. Once again the red line is the original data, while the blue and dashed lines are from the PCA reconstruction and Fourier analysis, respectively. There are no appreciable deviations in the signal

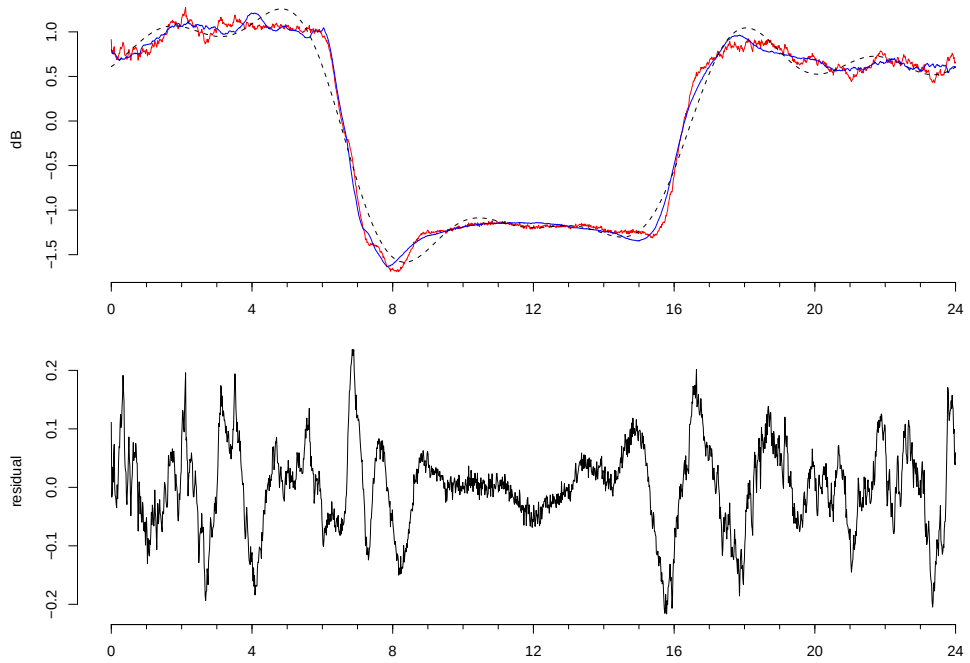

Figure 4.18: Reconstruction of the standardised data from GBZ on 26 December 2007. Red is the original data, blue the reconstruction from PCA and the dashed line is from a Fourier analysis. The bottom panel shows the residuals between the original data and the PCA reconstruction.

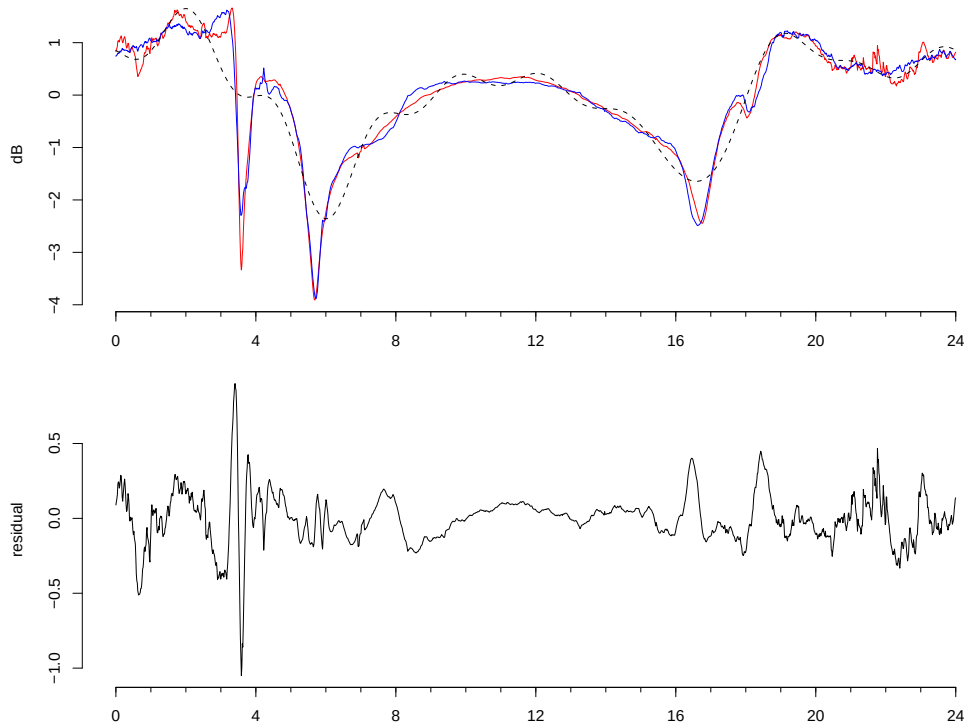

Figure 4.19: Reconstructed data from NSY on 23 April 2009. Format is the same as Figure 4.18.

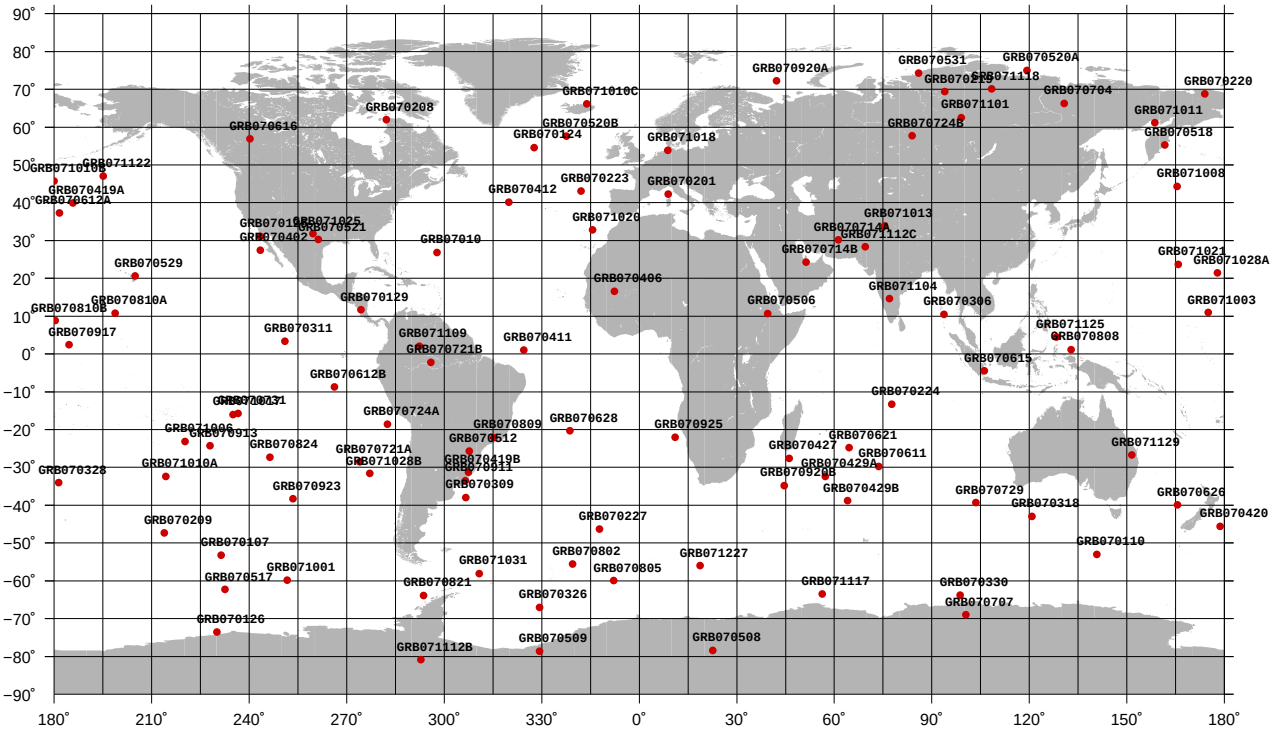

Figure 4.20: Map of sub-burst points for events detected in 2007.

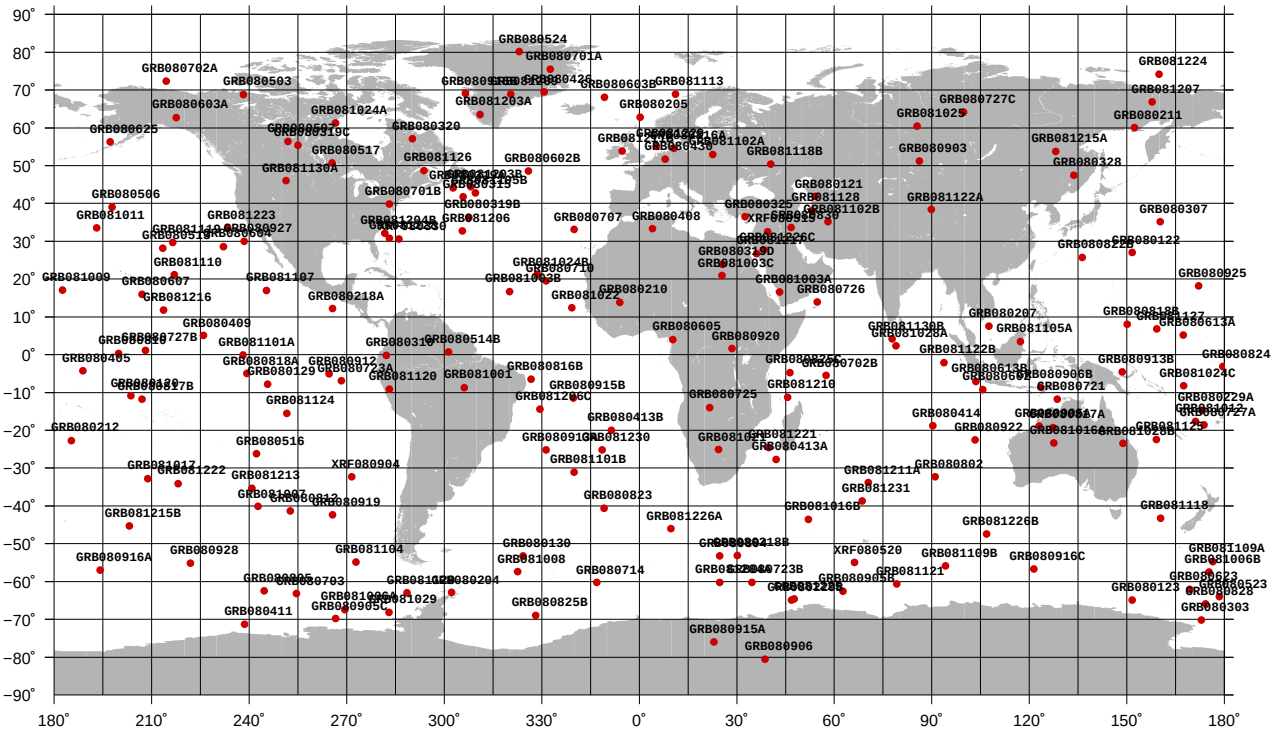

Figure 4.21: Map of sub-burst points for events detected in 2008.

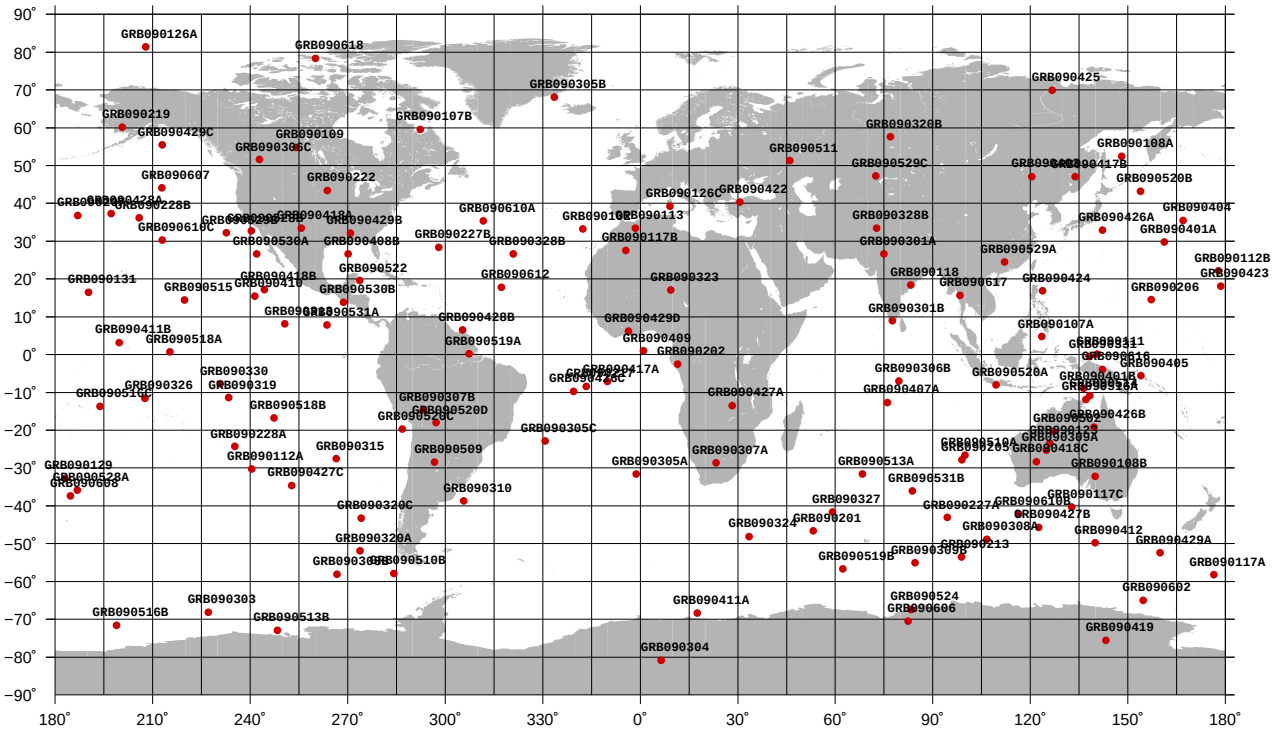

Figure 4.22: Map of sub-burst points for events detected in the first half of 2009.

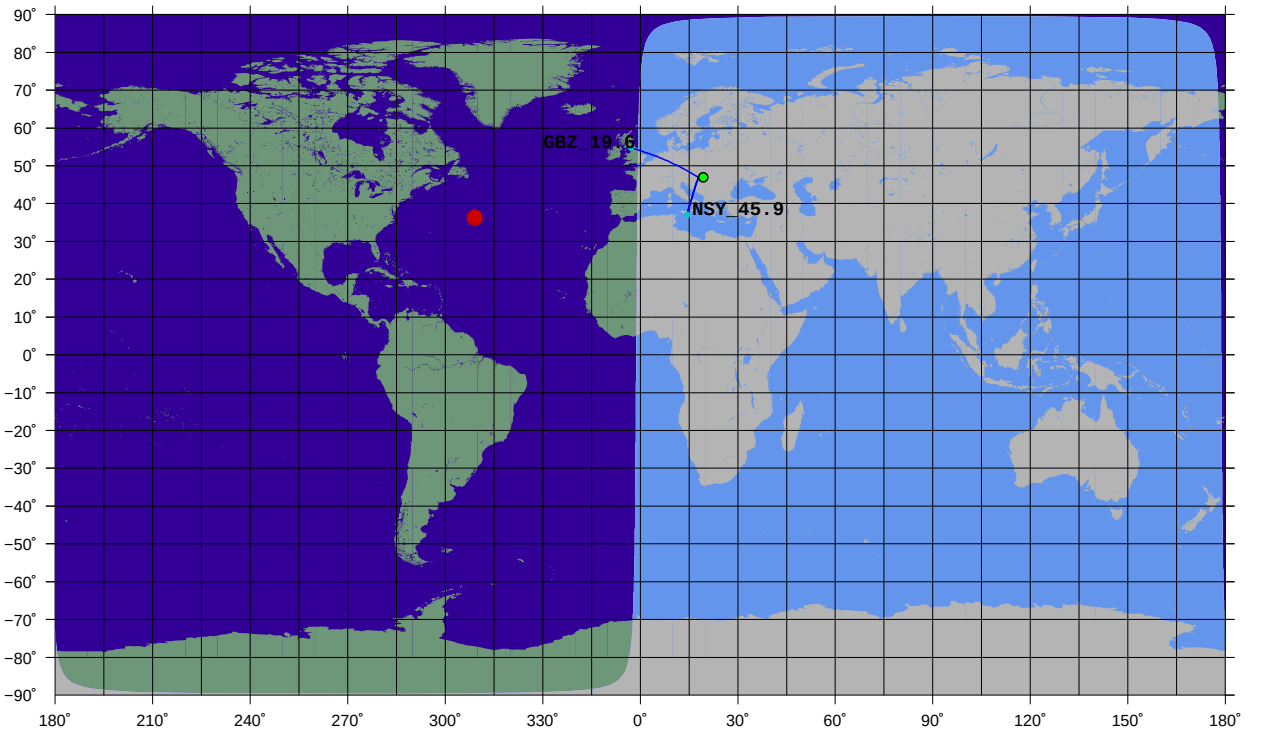

Figure 4.23: Map of GRB 080319B. The red dot indicates the sub-burst point of the GRB, while the green and blue dots indicate the locations of the transmitters and receiver. The night side of the Earth is shaded darker than the day side.

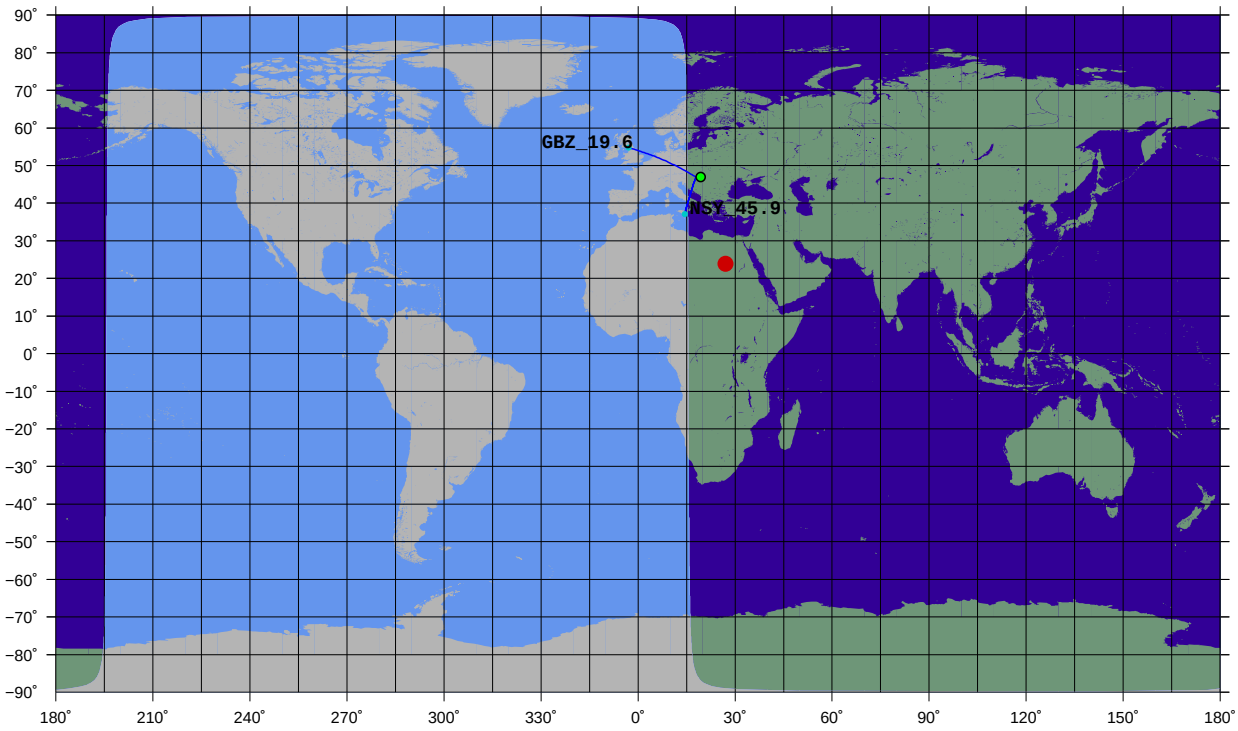

Figure 4.24: Map of GRB 080319D. The format is the same as Figure 4.23.

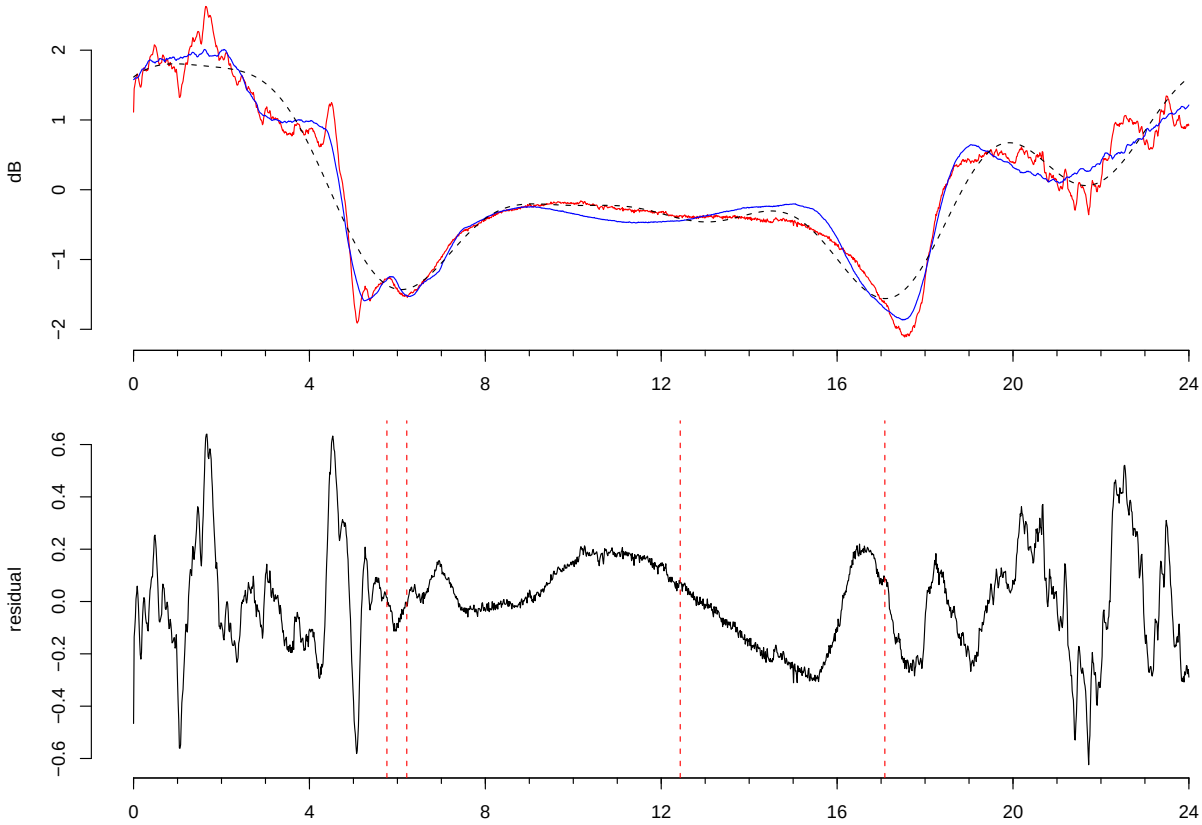

Figure 4.25: Signal strength variation for GBZ on 19 March 2008. The dashed lines on the residual plot indicate the time of GRBs.

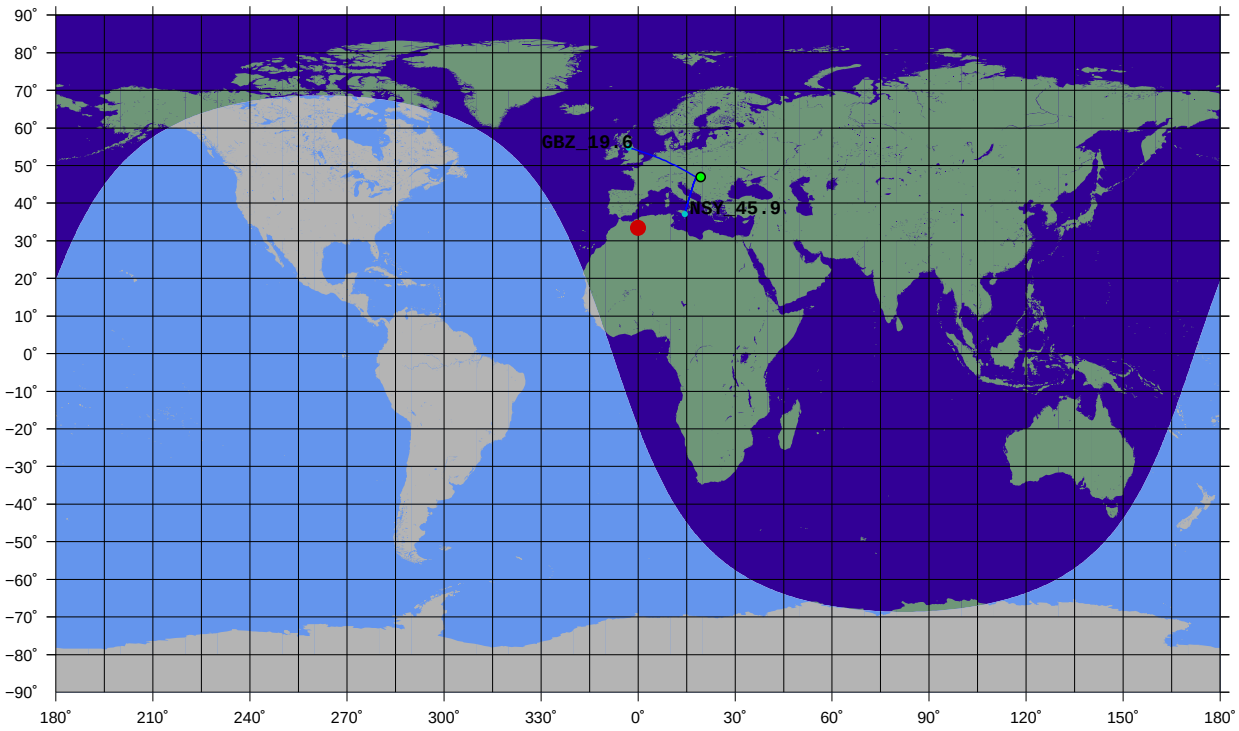

Figure 4.26: Map of GRB 090113.

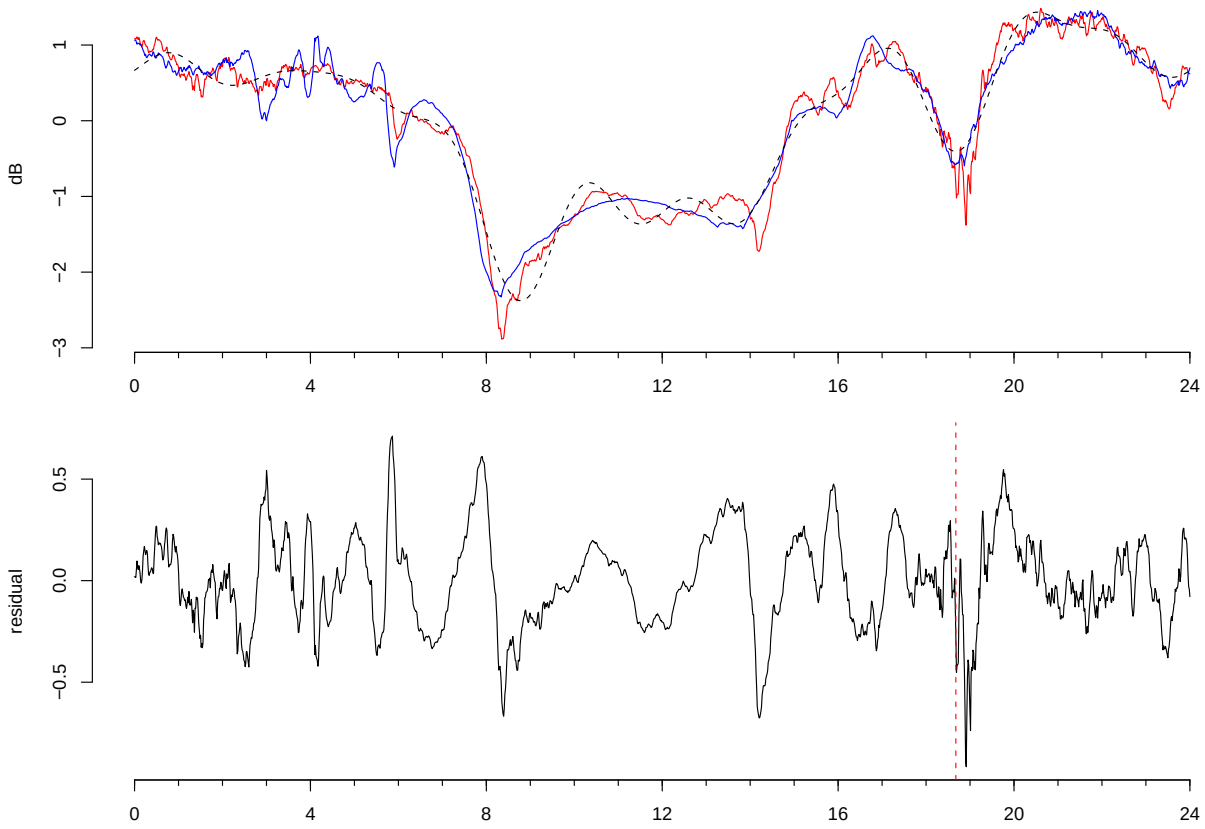

Figure 4.27: Signal strength variation for NSY on 13 January 2009. The dashed line on the residual plot indicates the time of the GRB.

strength seen around the times of the GRBs.

The bottom panel of Figure 4.25 shows the residuals between the original data and the PCA reconstruction. The red vertical lines indicate the times of the GRBs detected on that day. The second and fourth lines correspond to GRB 080319B and GRB 080319D. There are small perturbations in the residuals close to these times. However, it is difficult to ascertain if these are chance alignments of normal, random fluctuations or if they were caused by the GRBs. The distance between GRB 080319B and the signal path, along with the fact that the path is in daylight, suggests that this is a chance alignment.

In the case of GRB 080319D, the perturbation begins before the onset of the burst, therefore removing the burst as the cause of the perturbation. Thus, neither a strong, relatively distant burst, nor a closer, weaker burst have an effect on the day lit path.

The 20 s burst that occurred on 13 January 2009 at 18:40:39, denoted GRB 090113, had a sub-burst point located at 33.4285°N and 358.5194°E. This point is 2214 km from the receiver. GRB 090113 had a fluence of 7.6×10^{-10} Jm^{-2} (Tueller et al., 2009). Figure 4.26 indicates an ideal configuration of the system, with the signal paths and the sub-burst point in darkness.

Examination of the NSY signal amplitude received at Tihany, plotted in Figure 4.27, shows a possible perturbation, with sharp fluctuations at the time of the burst. The signal is, however, unusually perturbed on this particular day, thus it is once again difficult to ascertain the cause of the perturbation. There is no data available for this day from GBZ.

The lack of detected events in the subionospheric propagation data lead to a redefining of search parameters. The next step was to search all the GBZ and NSY data for any perturbation occurring at the same time as a GRB. This search turned up no positive results. The detection of a GRB appears to require a serendipitous occurrence of factors. Not only is the burst required to have a high enough fluence (the burst detected by Fishman and Inan (1988) had a fluence of 2×10^{-6} Jm^{-2}), but the sub-burst point should be relatively close to the signal paths and occurring over a nighttime ionosphere. A confluence of these factors did not occur within the data set examined.

4.3.2 Terrestrial Gamma Ray Flashes

Terrestrial Gamma Ray Flashes (TGFs) are detected by the Reuven Ramaty High Energy Solar Spectroscopic Imager (RHESSI). This satellite was launched into a circular orbit at an altitude of 600 km in early 2002. Although not its primary mission, detection of TGFs by the instruments on this satellite have been recorded since 2002. The RHESSI TGF catalog is available at `http://scipp.ucsc.edu/~dsmith/tgflib_public/` and is discussed by Grefenstette et al. (2009).

The number of TGFs detected between 26 May 2007 and 14 June 2009 was 145, with only 78 of these occurring within the same hemisphere as the signal paths. The residuals of the PCA reconstructions for both the NSY and GBZ data sets were examined for possible perturbations caused by these TGFs. Sixteen of these occurred at the same time as a perturbation in the residuals. The sub-satellite points are plotted in Figure 4.28. Grefenstette et al. (2009) calculate that the TGF occurs at least 255 km from the sub-satellite point. Although each TGF is in the same hemisphere as the signal paths under examination, they are all a considerable distance away, with some grouped quite tightly together over the northern regions of South America. As the attenuation for γ-rays in the atmosphere is high, the ionospheric effect of a TGF would be localised to the ionosphere above the event and would not travel over the horizon.

As no TGF occurred simultaneously with a perturbation on both transmitter signals, the top three energetic flashes are presented.

Figures 4.29 to 4.31 show the amplitude of the VLF transmitter signal, the residuals from the PCA reconstruction and the energy flux of the TGF. Each flash has a duration in the order of 50 µs and the energies recorded range from 4500 16000 keV. There is no correlation between the

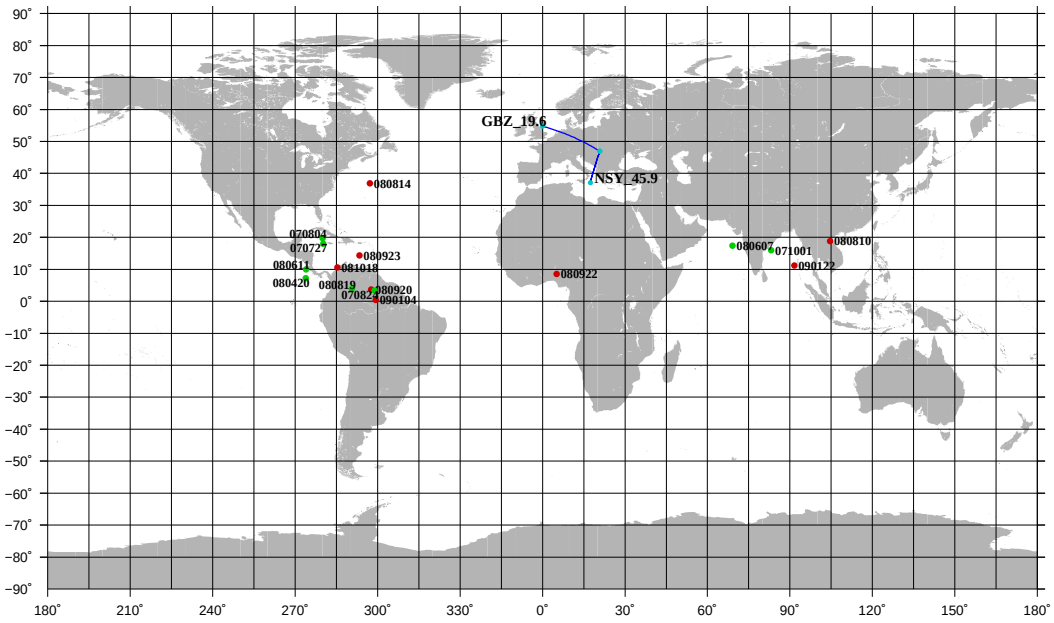

Figure 4.28: Map of sub-satellite points for TGF detections.

size of the perturbation in the residuals plot and the energy of the TGF, with the more energetic TGFs not necessarily creating a larger perturbation. Some of the largest perturbations occur with lower energy flashes.

It is therefore necessary to conclude that the perturbations seen in the residual data are not caused by the occurrence of TGFs and rather some random fluctuations of the nighttime ionosphere.

4.3.3 Solar Flares

Solar flare data is recorded by the Geostationary Operational Environment Satellites (GOES), which were first launched in 1975. Currently, GOES-10 and GOES-12 are operating in geostationary orbits, at altitudes of ~ 35800 km. The Space Environment Monitor is an experiment consisting of a magnetometer, X-ray sensor, high energy proton and alpha particle monitor and an energetic particle sensor. GOES-12 also sports a Solar X-ray Imager. A catalog of X-ray solar flares detected by the GOES satellites was used in this analysis and is available from `ftp://ftp.ngdc.noaa.gov/STP/SOLAR_DATA/SOLAR_FLARES/XRAY_FLARES/`.

The times of solar flares for 2007, 2008 and the beginning of 2009 were compared with the amplitude and residual plots of the VLF data from GBZ and NSY. Particular attention was paid to flares occurring during the local daytime of the signal paths, due to the expectation that only the sunlit portion of the ionosphere would be affected, and flares classified greater than C1.0.

The most remarkable signature detected in both the VLF data and residuals caused by a solar flare is shown in Figure 4.32. This C4.5 event began at 09:39 UT on 13 December 2007, ending half an hour later, with the peak occurring at 10:03 UT. The total integrated flux for this flare was 3.3×10^{-3} Jm^{-2}. The X-ray flux is shown in Figure 4.33. The perturbation in the GBZ data begins at the onset of the second and bigger peak in the flare. After the flare, the signal strength returns to its normal daytime level. Although this was detected in the raw data, the event signature was much more obvious in the residuals.

There were 20 other flares that occurred on this day, with classes ranging from B1.6 to C4.5. Only flares with an integrated flux greater than 2×10^{-4} Jm^{-2} are indicated in Figure 4.32. This

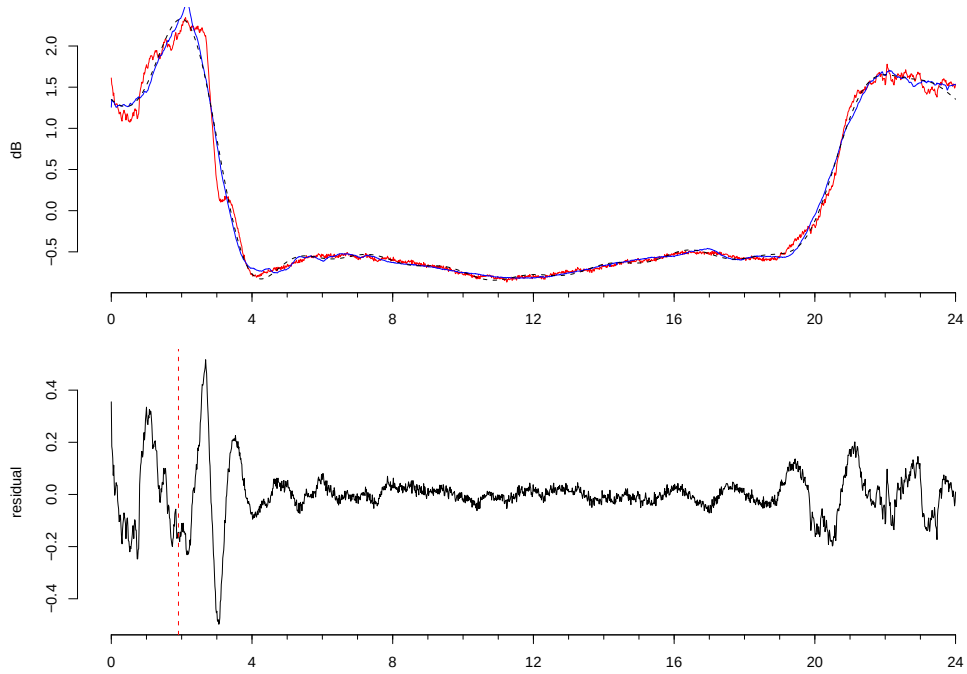

(a) Amplitude of GBZ, with time of the TGF indicated by the red dashed line

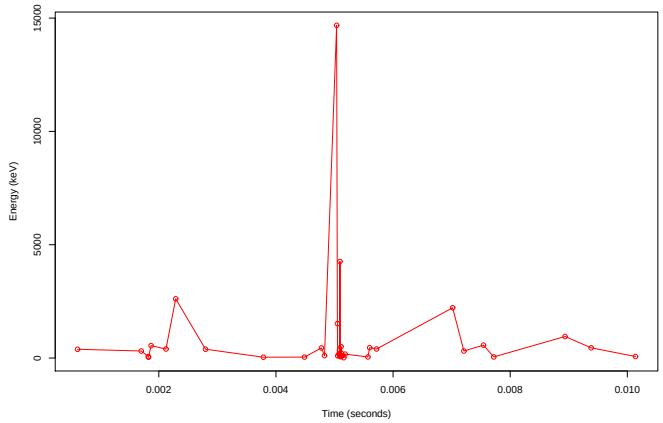

(b) Energy flux of TGF

Figure 4.29: TGF occurring on 27 July 2007.

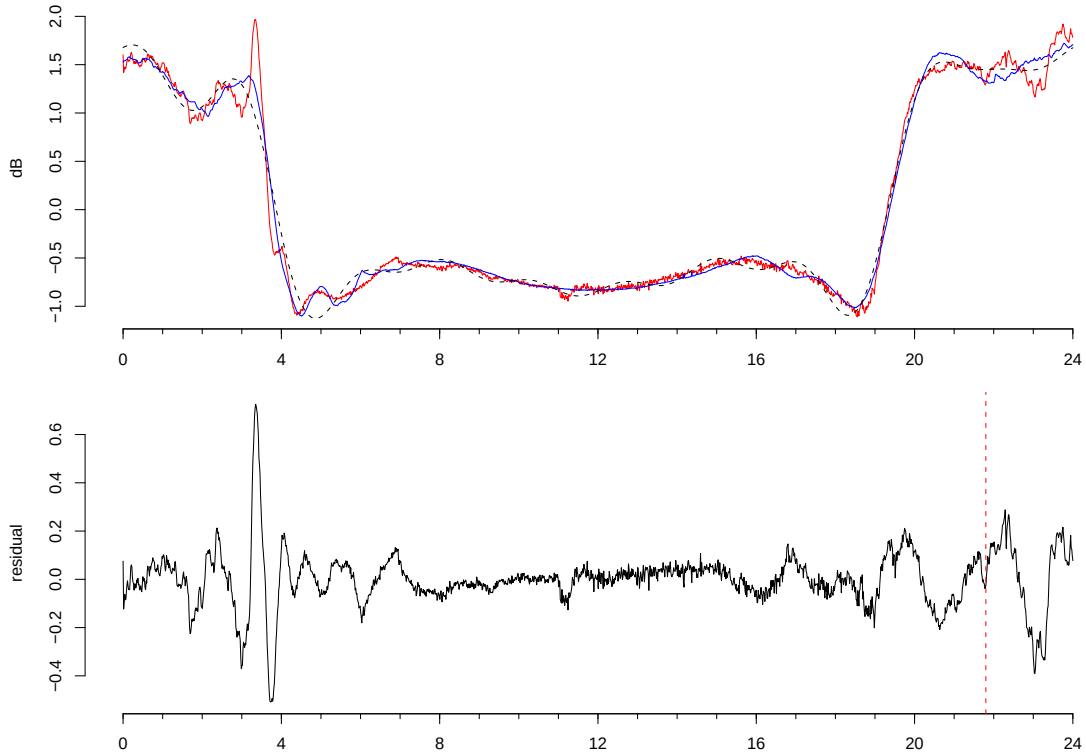

(a) Amplitude of GBZ, with time of TGF indicated by the red dashed line.

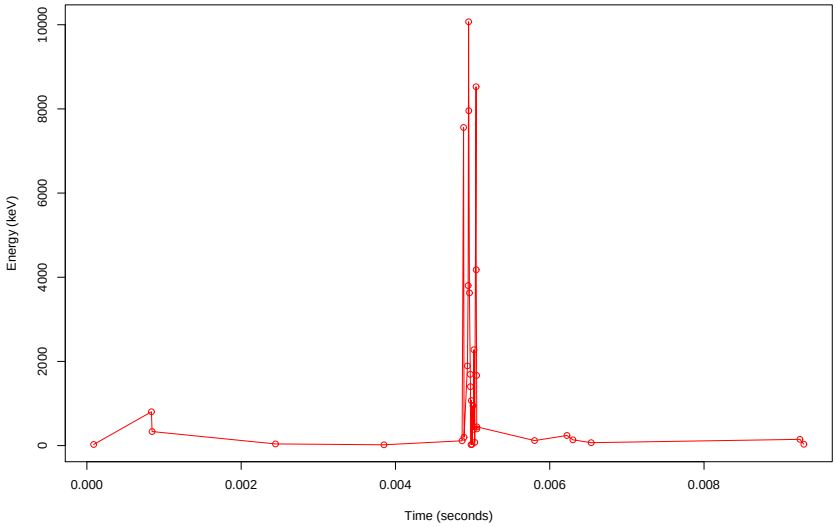

(b) Energy Flux

Figure 4.30: TGF occurring on 20 April 2008.

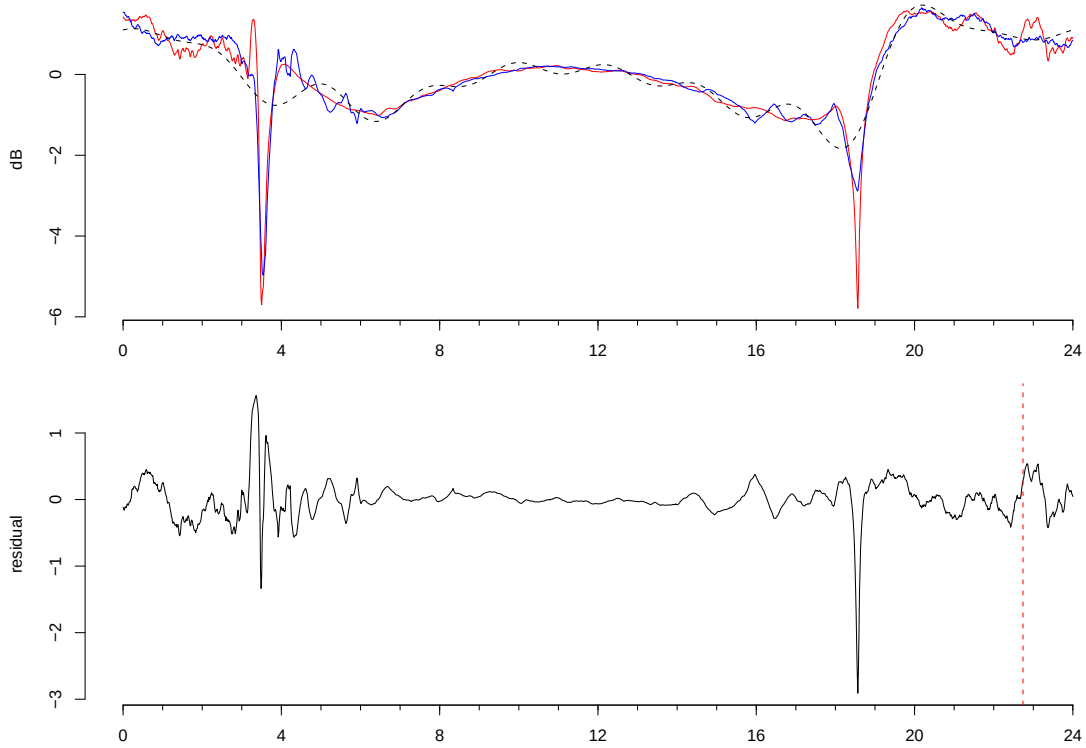

(a) Amplitude of NSY, with the TGF indicated on the residuals plot.

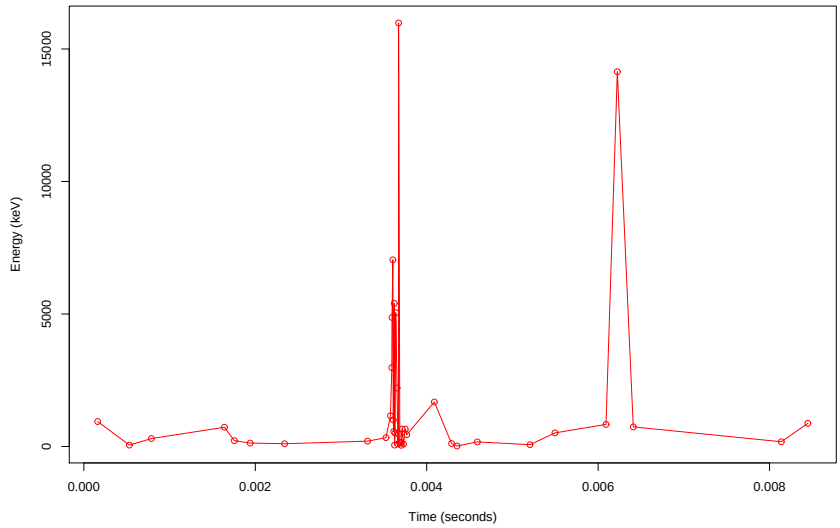

(b) Energy Flux

Figure 4.31: TGF occurring on 14 August 2008.

limitation was derived empirically, as only flares with larger flux are seen to cause a perturbation in the residual data.

Of the ten solar flares indicated by the red, vertical dashed lines in Figure 4.32, four (including the C4.5 flare already mentioned) show possible perturbations in the residuals. The first is a B7.8 flare, with integrated flux 2.2×10^{-4} Jm^{-2}. The flare lasted 7 min, peaking at 01:04 UT. The perturbation occurs when the GBZ–Tihany path is in darkness and thus may be a chance alignment. However, the sharp drop in the signal amplitude occurs concurrently with the flare onset, while the end of the flare occurs at the of bottom of the dip, making a chance alignment unlikely.

The next possible flare perturbation has a peak flux occurring at the peak of a bump in the residuals at 14:06 UT. This was a 13 min C1.0 flare, beginning at 13:59 UT, and had an integrated flux of 5.4×10^{-4} Jm^{-2}. The perturbation is small, but clear in the residuals.

The last event on 13 December 2007 was a C1.7 flare, which lasted 27 min and had a total integrated flux of 1.7×10^{-3} Jm^{-2}. The dashed line at 22:00 UT indicates the time of the peak flux, which occurred 8 min after the onset of the flare. The perturbation is seen in the amplitude of GBZ, as well as the residuals, as a small spike at the beginning of the flare and then a sudden decrease at the time of the peak flux. As with the B7.8 flare, the timing is precise enough to suggest that this perturbation is caused by the flare, despite the signal path being in darkness and hence the flare occurring on the other side of the Earth.

There were many solar flare signatures detected in the residuals from the PCA reconstruction of GBZ, all of which had an integrated flux greater than 2×10^{-4} Jm^{-2}, as mentioned above. However, not all flares which exceed this limit create a disturbance in the data. On 18 December 2007, there were 23 solar flares, with only 12 having an integrated flux greater than 2×10^{-4} Jm^{-2}. Of these, 5 are responsible for detectable perturbations in the residuals (see Figure 4.34). These were classed as B2.4, C2.1, B6.3, B8.4, C1.6 with peak fluxes occurring at 1:34, 13:20, 14:34, 15:24, 19:15 UT, respectively.

A number of solar flares also created perturbations in the PCA reconstruction of the NSY data. Examples of these are shown in Figures 4.35 and 4.36, which were flares recorded on 2 and 3 November 2008. The empirically derived total integrated flux limitation on the creation of a perturbation in the residuals does not hold for NSY, in fact appearing to be much lower. In Figure 4.35, the first flare with peak time indicated at 13:28 UT, is a B2.7 flare with total integrated flux of 1.7×10^{-4} Jm^{-2}. The perturbation seen in the residuals is a small dip, with the start and end times of the flare corresponding to the start and end times of the dip.

The next flare with the peak flux occurring at 14:40 UT is classed as B1.5. The total integrated flux was 4.5×10^{-5} Jm^{-2} and the residuals show no effect. The 5 min long B7.2, 1.3×10^{-4} Jm^{-2} event peaking at 15:05 UT does have a definite signature in the residuals, with a sharp drop at the time of the flare.

The last flare recorded on 2 November was also 5 min long. This had a peak at 20:15 UT and was classed as a B5.7 event. There is a clear concurrent drop in the residuals at this time. The total integrated flux was 7.5×10^{-5} Jm^{-2}, which is the smallest flux with a detected effect. Thus, this is adopted as the flux limit for NSY.

The flares occurring on 3 November 2008 corroborate this limitation. The first flare indicated is a B2.9 event, had a total integrated flux of 5.2×10^{-5} Jm^{-2} and is not seen in the residuals. The second flare has a very clear signature, also seen in the raw data. This C1.6 class event had a duration of 7 min, with the 11:19 UT peak occurring in the middle of this interval. The total integrated flux was 3.5×10^{-4} Jm^{-2}.

The B2.4 event is also detected in the residuals, even though it occurred at local nighttime. The time of the peak flux of this 18 min long flare is indicated on Figure 4.36 as usual. The total flux is 1.9×10^{-4} Jm^{-2}, supporting the detection limit.

4.4 Varimax Rotation

The results of the PCA on GBZ and NSY have provided a much more sensitive method for detecting transient events. However, as mentioned earlier, the understanding of the components themselves is complicated. Yet they have the capability to reveal much about the influences on subionospheric signal propagation. Thus, a Varimax rotation was performed on the results from the PCA on both data sets, in order to improve their interpretability.

4.4.1 GBZ, 19.6 kHz Transmitter

The rotation described in Section 3.2.3 was applied to the GBZ PCA, with 11 components retained. The first principal component in the new rotated space is presented in Figure 4.37, along with the component loadings. The variation of the component loadings throughout the data set has changed considerably from that seen in 4.4(b), with only summer months now strongly, positively correlated with PC 1. The correlations for the remainder of the variables are still positive, but now much smaller. Indeed, in Figure 4.37(a), the PC 1 signal is representative of the signal strength of GBZ during the summer months (see Figure 4.1(a)).

The second principal component, shown in Figure 4.38, also has annually varying loadings with the original variables. The maximum correlations occur for the northern hemisphere winter months and thus PC 2 represents the winter signal variation of GBZ. The original component is shown in Figure 4.5.

The correlations for PC 3 vary semi-annually, with all variables negatively correlated with this component. The anti-correlation peaks occur for September and March throughout the data set, thus PC 3 is most important for the signal variation during the equinoxes. The addition of this component with the relevant percentages of PC 1 and 2, creates the peaks just before the dawn and following the dusk transitions. Figures 4.39 and 4.40 show the components and loadings for PC 3 and 4. Figure 4.39 can be compared to the original component in Figure 4.6. Once again, PC 4 has a random distribution of correlations. The signal itself has not been modified too extensively from the original, seen in Figure 4.7, and thus it has the same effect on the data. It tends to add an asymmetry to levels of nighttime signal strength before dawn and after dusk, as well as sharpening the effect of the dawn terminator.

PC 5, shown in Figure 4.41, has a semiannual variation in the loadings, with peaks occurring in October and February. These are transition months, between autumn and winter and winter and spring. This component accounts for variations in the signal strength that occur mainly during these times of the year, namely pre-dawn and post-dusk peaks in the amplitude. It also deepens the dawn amplitude drop.

PC 6 in Figure 4.42 has very little variation in the component loadings, with none of the variables being strongly correlated with it. For variables which are positively correlated with it, the PC 6 lowers the signal level at the dusk terminator, while increasing the pre-dawn signal strength.

4.4.2 NSY, 45.9 kHz Transmitter

The varimax rotation was performed on the NSY transmitter data, with 18 of the principal components retained. The results of the rotation are less well defined than those for GBZ, yet they do provide minor clarification on the effects of the components.

The first principal component, shown in Figure 4.43, represents the signal variation of NSY during winter, with the variables from October to February strongly correlated with it. PC 2 in Figure 4.44 also shows an annual variation in its loadings, with the stronger correlations around summer. The original principal components can be viewed in Figures 4.11 and 4.12.

Figures 4.45 to 4.48 show the next four principal components, for comparison with the pre-rotated components in Figures 4.13 to 4.15. PC 3 shows a semi-annual variation in the correlations, with peaks around the equinoxes, the largest of these being in March. Comparison of this component with Figure 4.8(d) shows a remarkable similarity between these two curves. Thus, it represents the signal strength variation during autumn and spring.

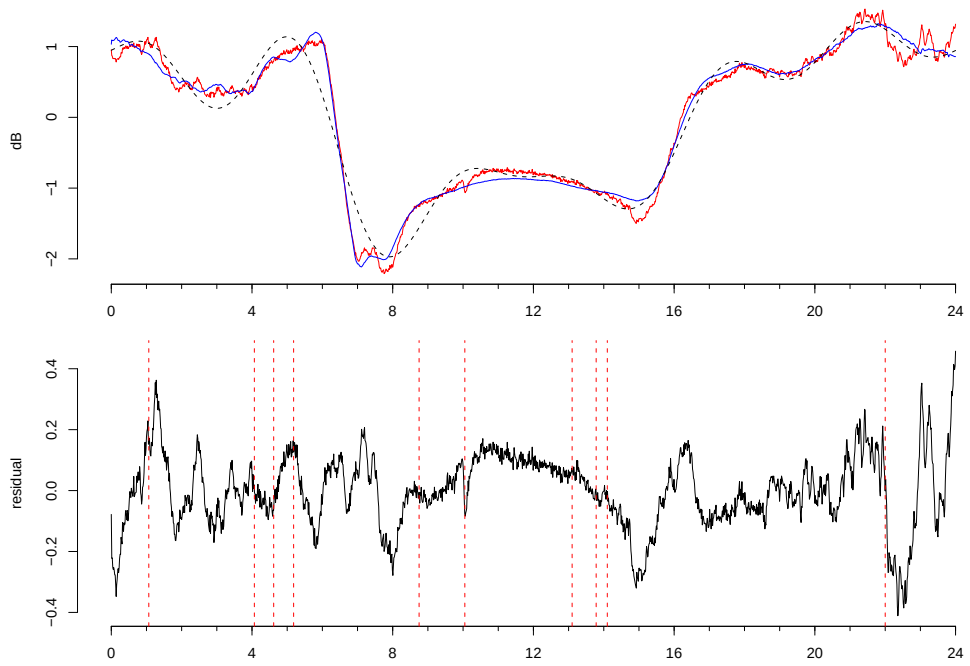

Figure 4.32: Signal strength of GBZ on 13 December 2007, with the dashed lines on the bottom panel showing times of solar flares with integrated flux $> 2 \times 10^{-4}$ Jm^{-2}.

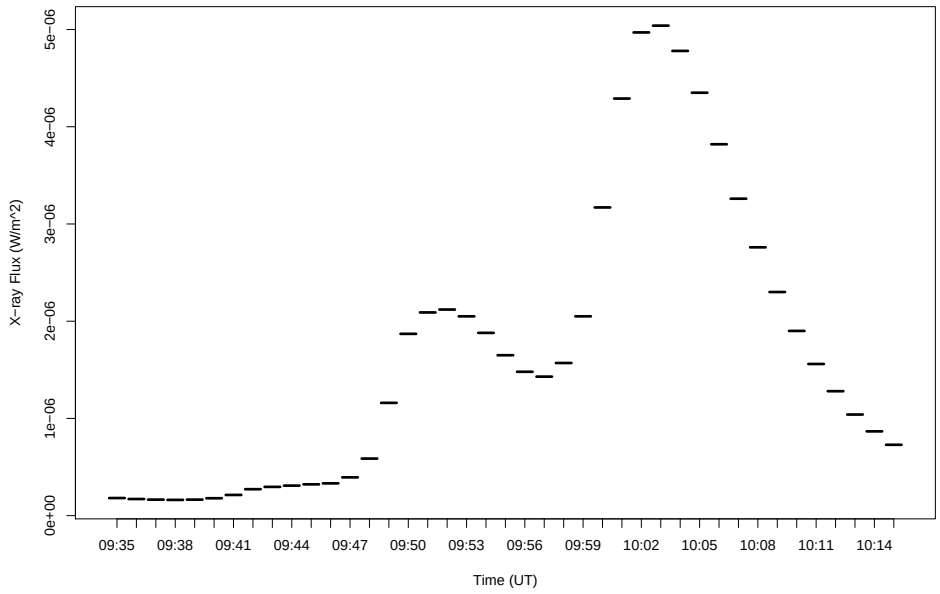

Figure 4.33: X-ray flux for the C4.5 flare with onset at 9:39 UT on 13 December 2007.

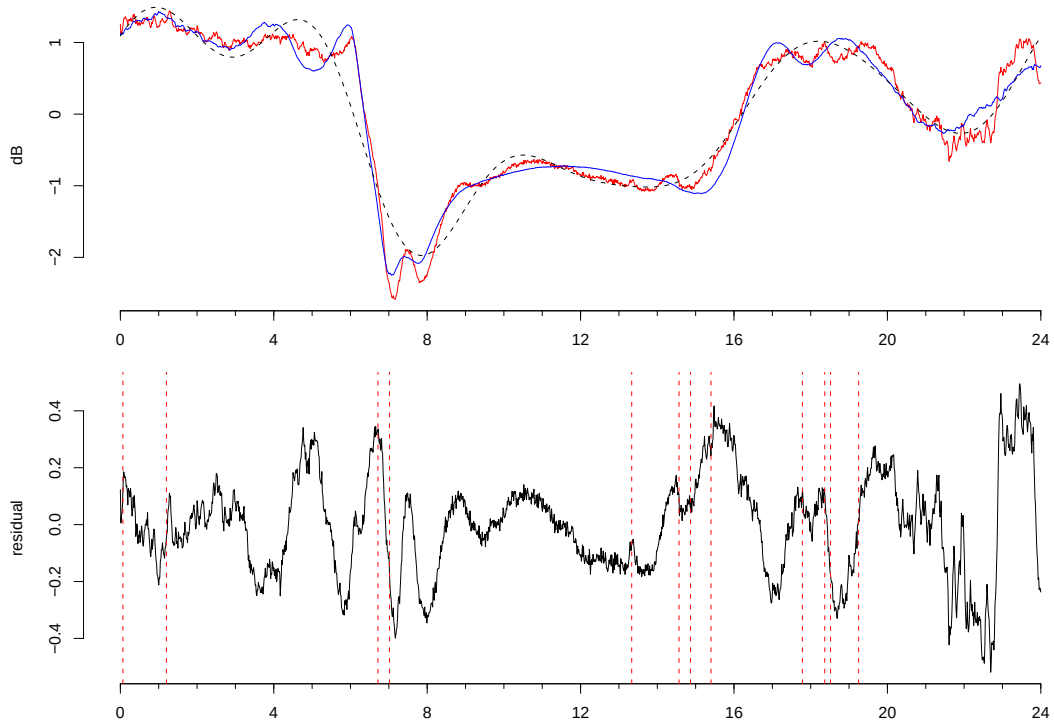

Figure 4.34: Signal strength of GBZ on 18 December 2007, showing the times of solar flares with integrated flux $> 2 \times 10^{-4}$ Jm^{-2}.

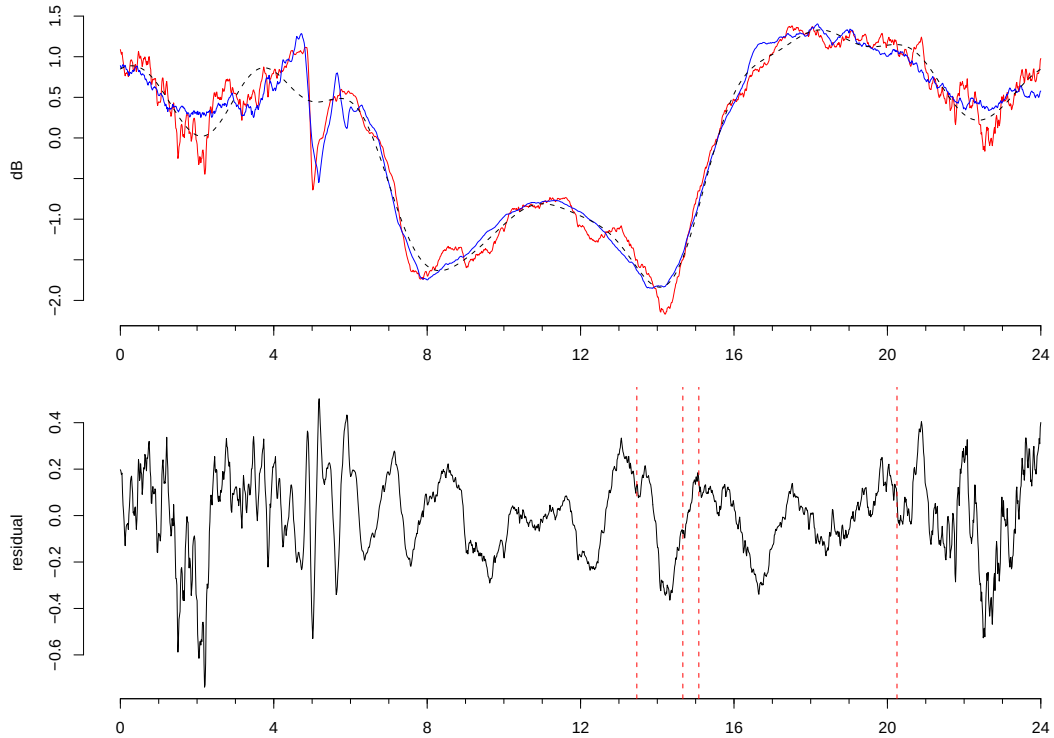

Figure 4.35: Signal strength of NSY on 2 November 2008, with times of all solar flares indicated.

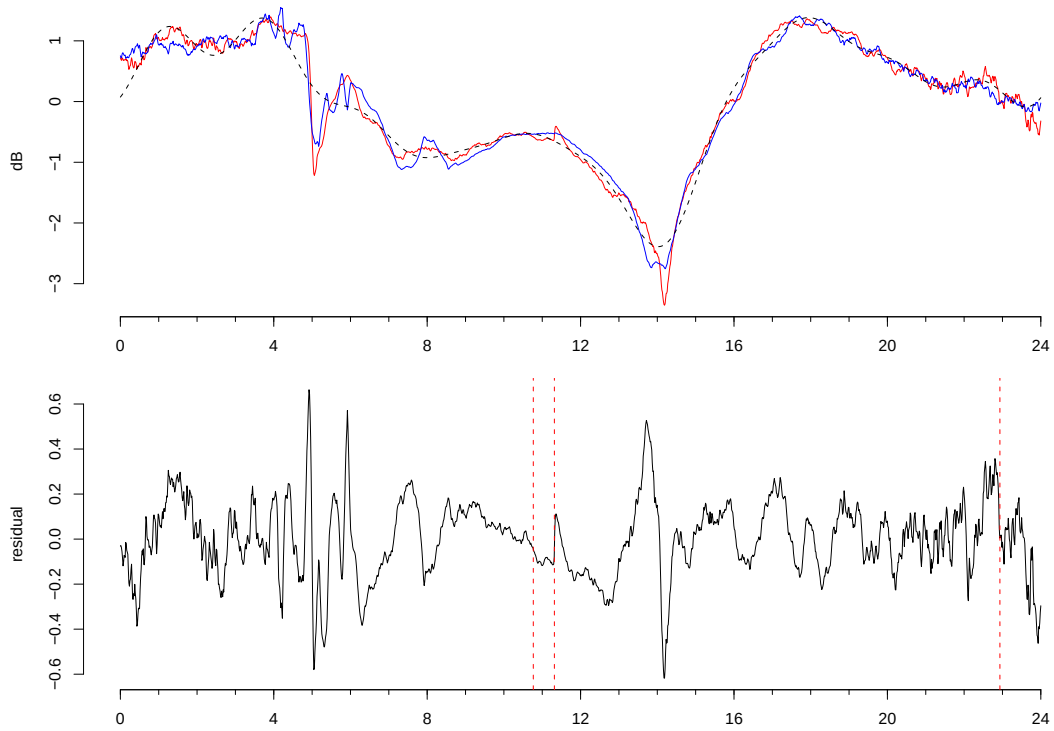

Figure 4.36: Signal strength of NSY on 3 November 2008, with times of solar flares indicated.

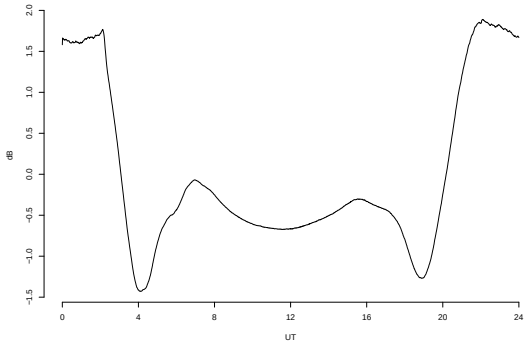

(a) PC 1

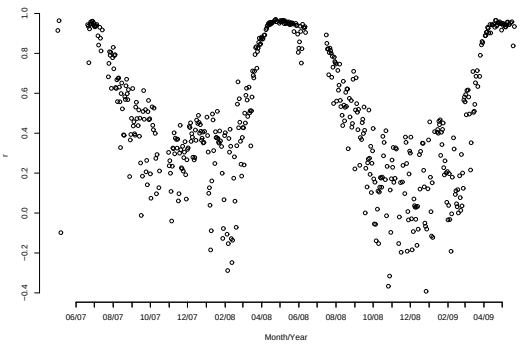

(b) Loadings of PC 1

Figure 4.37: First principal component and loadings for GBZ.

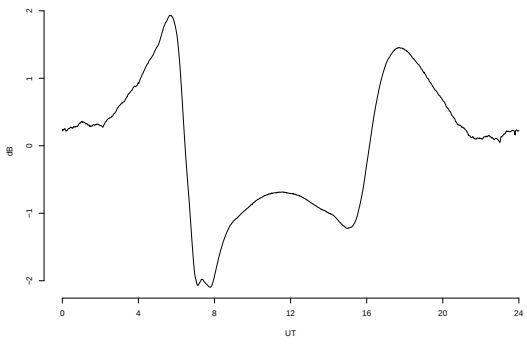

(a) PC 2

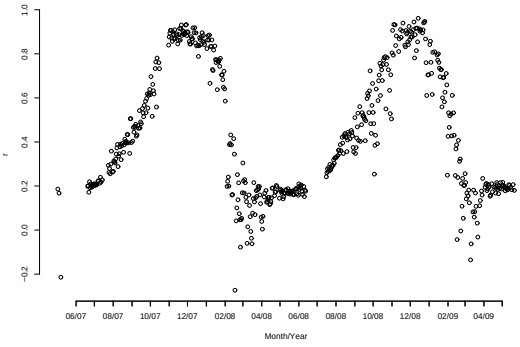

(b) Loadings of PC 2

Figure 4.38: Second principal component and loadings for GBZ.

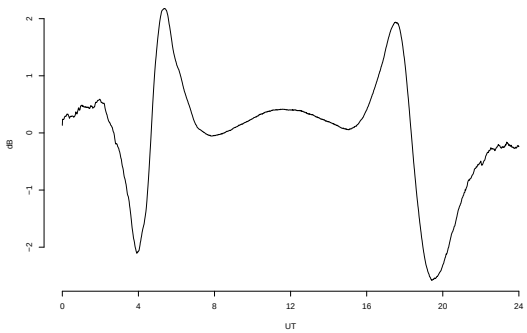

(a) PC 3

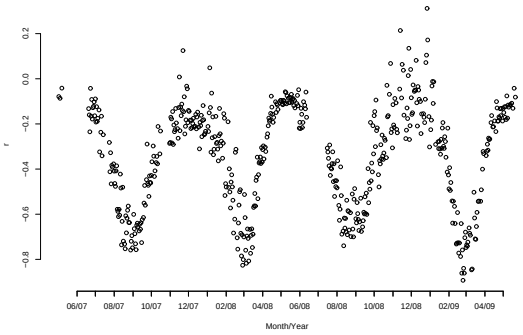

(b) Loadings of PC 3

Figure 4.39: Third principal component and loadings for GBZ.

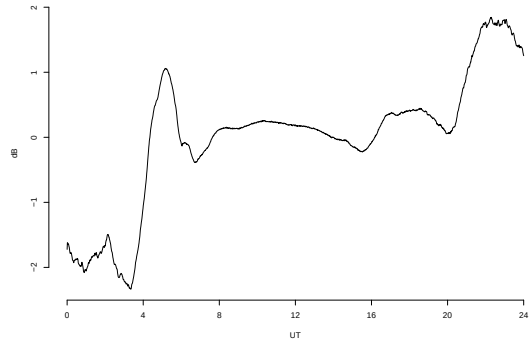

(a) PC 4

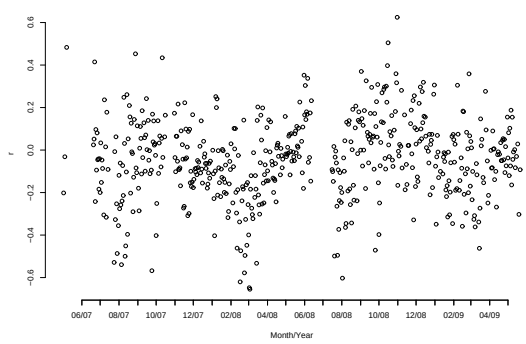

(b) Loadings of PC 4

Figure 4.40: Fourth principal component and loadings for GBZ.

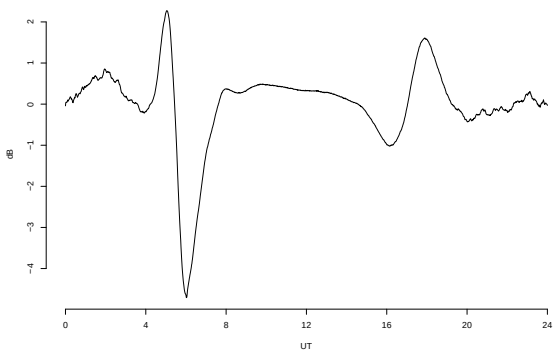

(a) PC 5

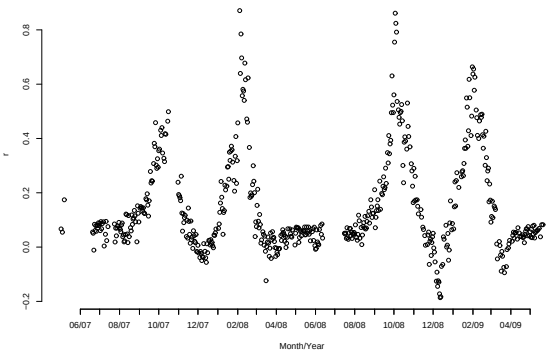

(b) Loadings of PC 5

Figure 4.41: Fifth principal component and loadings for GBZ.

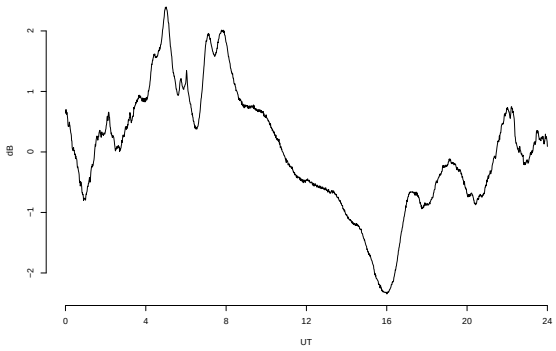

(a) PC 6

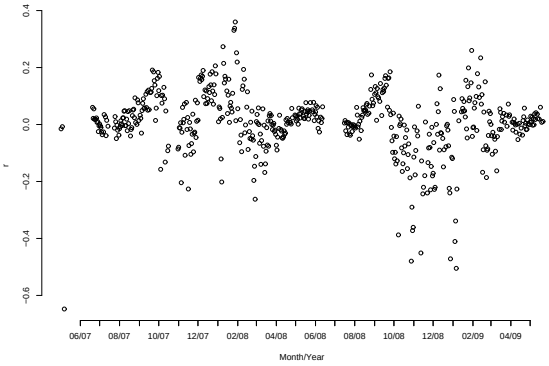

(b) Loadings of PC 6

Figure 4.42: Sixth principal component and loadings for GBZ.

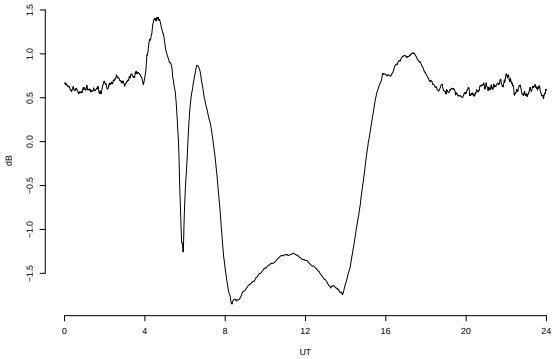

(a) PC 1

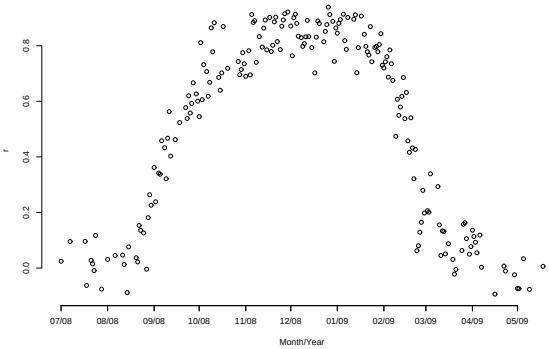

(b) Loadings of PC 1

Figure 4.43: First principal component and loadings for NSY.

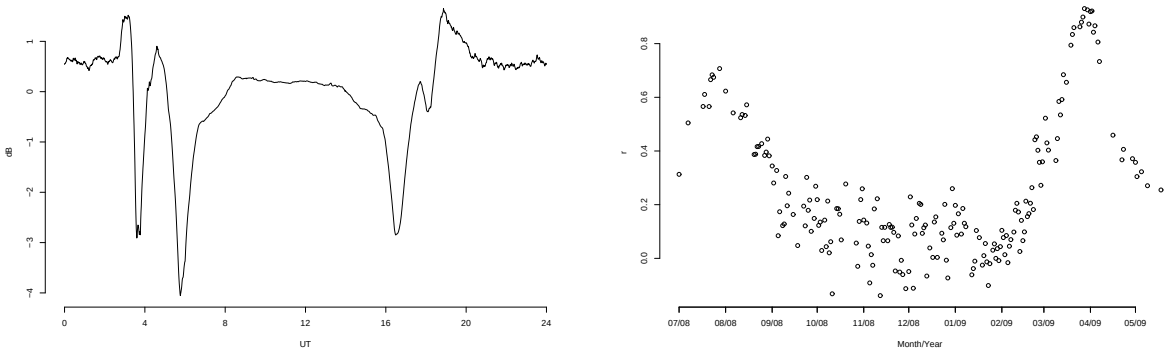

(a) PC 2 (b) Loadings for PC 2

Figure 4.44: Second principal component and loadings for NSY.

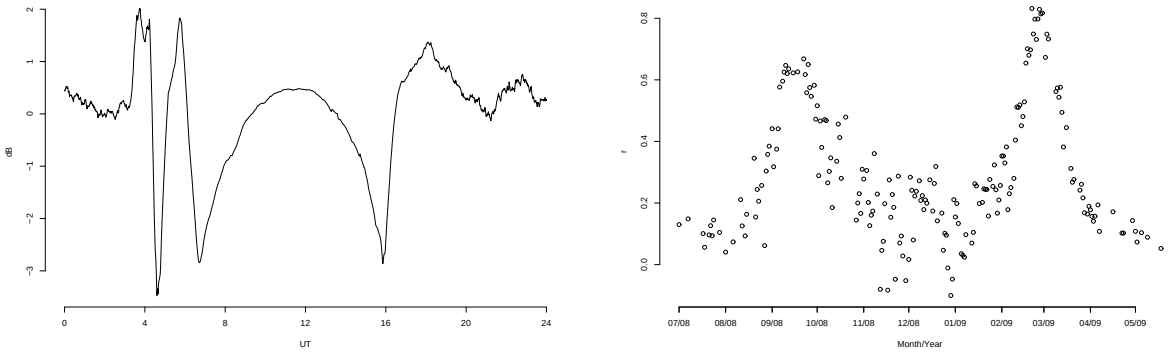

(a) PC 3 (b) Loadings of PC 3

Figure 4.45: Third principal component and loadings for NSY.

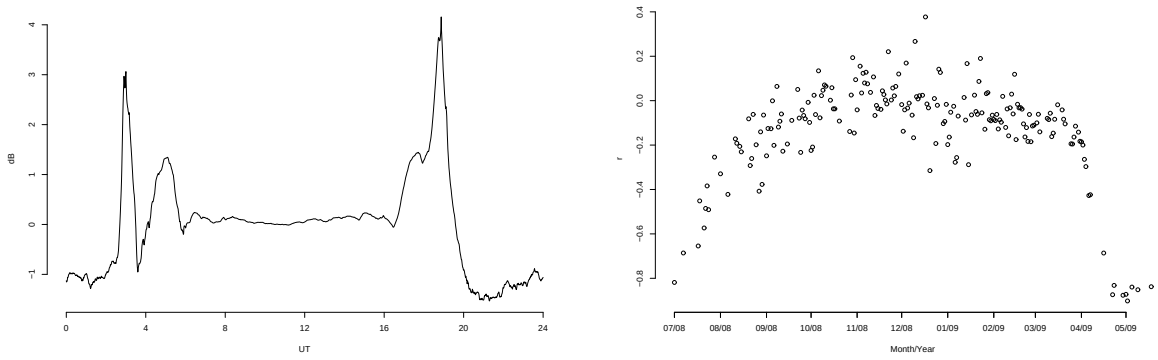

(a) PC 4 (b) Loadings of PC 4

Figure 4.46: Fourth principal component and loadings for NSY.

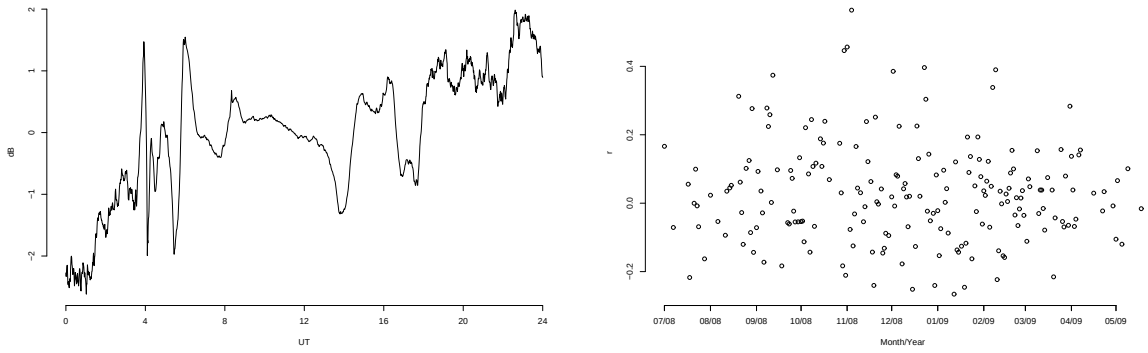

(a) PC 5 (b) Loadings of PC 5

Figure 4.47: Fifth principal component and loadings for NSY.

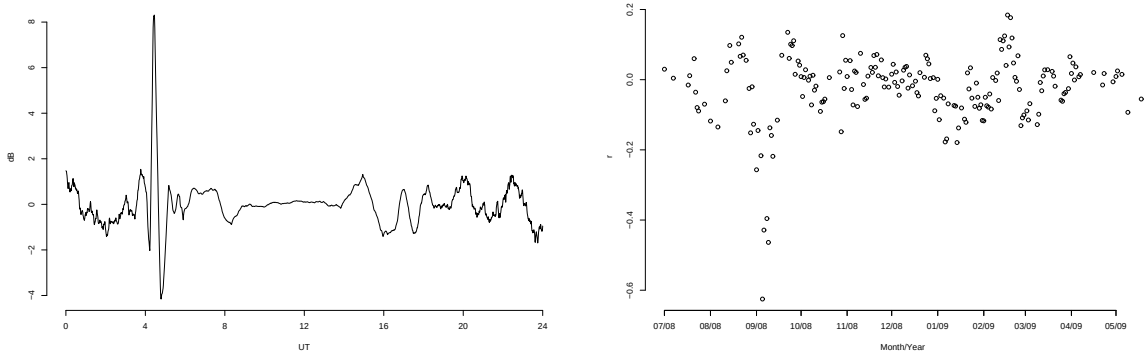

(a) PC 6 (b) Loadings of PC 6

Figure 4.48: Sixth principal components and loadings for NSY.

PC 4 has a mostly small, negative correlation with the majority of variables, with the loadings becoming increasingly negative towards the summer. This component acts to level out the daytime signal of the summer months, also moving the dawn and dusk terminator dips to earlier and later times respectively.

The generally random distributions of loadings on PC 4 for GBZ is seen here in PC 5. This component also acts to add an asymmetrical bias between the pre-dawn and post-dusk nighttime signal strength. The sixth principal component is only strongly anti-correlated in September with a few variables and adds a strong oscillation to the signal at around 04:30 UT.

Although the analysis of the effect of each principal component is still complicated, the varimax rotation has made it simpler to determine the time of year when the component has the most influence on the signal variation. This is due to the fact that the loadings are either strong or weak and no longer strongly positive and strongly negative and hence each variable is defined by only a few strong correlations with the principal components.

Chapter 5

Conclusions

Subionospherically propagating VLF signals are strongly influenced by conditions in the ionosphere. Diurnal and annual variations arise in the signals due to the corresponding variations in the ionosphere. As there are many factors which influence the bottom of the ionosphere, on a periodic and transient basis, the consequent variations in the signals are quite complex.

Narrowband VLF data have been analysed using a multivariate data analysis technique, principal components analysis, in an attempt to unravel some of these complex variations. Once the standard annual and diurnal variation is known, transient events can be detected in the deviations of the signal from the expected norm.

There were two transmitters used in this analysis. The data for GBZ, operating at 19.6 kHz, covered a span of almost two years, while the data from NSY, operating at 45.9 kHz, was just under a year long. This allowed for some interesting analysis of both the diurnal and annual variations in the signals.

The days on which operational problems with the transmitter or receiver caused the recording of bad data were neglected when the PCA was performed. This is due to the common sense rationale that goes with any computational analysis: garbage in equals garbage out. The gaps in the data time series caused by removing the bad data did not adversely affect the results of the PCA. In fact, the results of the PCA may be used to construct an estimation of the quiet signal amplitude variation on missing days, either by a crude average of the surrounding days, or by an interpolation between the reconstructed signals.

Quiet time estimation of the signals, acquired by reconstructing the variables without the higher order components, performed consistently better than a Fourier analysis. This is because PCA reconstruction uses basis functions that are derived from the data itself, while the Fourier analysis is based on generic mathematical functions.

PCA for GBZ indicated the first nine principal components collectively accounted for 95% of the variance in the data. By summing the relevant amounts of each of these components an approximation of the signal for any day within the data set can be created. Examination of each principal component and its component loadings also yields valuable information. The first principal component is one on which all the variables are strongly positively correlated. This shows the general diurnal variation seen throughout the year. The higher order components then add effects typical of each season, moving the dawn and dusk terminators, changing their shape, and changing the signal level of both the daytime and nighttime transmission. The times at which each component is most important is seen in high correlation values of their loadings.

Although the PCA of NSY did not perform quite as well as that for GBZ, similar results were obtained. NSY, being a north-south signal, varies more drastically over the course of a year than GBZ. This is due to the differing times at which the terminator crosses the signal path and the differing angle at which this occurs throughout the year. During the equinoxes, the terminator line would be almost parallel to the signal path, meaning that the change between day and night

occurs rapidly. This greater annual variability of NSY is reflected in the number of components required to account for 95% of the variance in the data, being 28 components.

Both the GBZ–Tihany and NSY–Tihany paths are relatively short (less than 2000 km). These results would be interesting in comparison to the equivalent from a longer signal path.

The residuals between the reconstructed curve and the original data, of both transmitters, were examined for the effects of transient events. These transient events are expected to cause additional ionisation in the ionosphere, causing a modification in the Earth-ionosphere waveguide, thereby changing the propagation conditions of the signals.

The residuals were examined for the effects of over 390 GRBs occurring over the course of 2007, 2008 and the first half of 2009. No effects were seen in either the residuals, or the raw data, for either transmitter. The observation of a transient effect in the VLF data caused by a GRB requires the following things:

- a long burst, with duration exceeding 100 s;
- the fluence of the burst must be greater than $\sim 10^{-7}$ Jm^{-2};
- the sub-burst point must be in reasonable proximity to the transmitter-receiver paths;
- the signal path should be in darkness;
- and both the transmitter and receiver need to be operational.

A confluence of these factors did not occur within the time frame of the data.

The 145 TGFs occurring during the time frame of the data set also did not create an effect in the residuals. Although there were some alignments of fluctuations with the times of the TGFs in the residuals, these flashes occurred too far away to conceivably have an effect. As the TGF occurs within the neutral atmosphere, and γ-rays are absorbed by this medium, the TGF signal would not be detected over the horizon and hence a VLF-perturbing TGF would need to occur over the transmitter path.

Numerous solar flare perturbations were detected in the residual data. The lower total integrated flux limit for detection of an event on GBZ was determined as 2×10^{-4} Jm^{-2} and that for NSY was 7.5×10^{-5} Jm^{-2}. Previous events detected in VLF data put the lowest class of the event that could cause an ionospheric effect as a C1 flare. However, the residuals method is much more sensitive to perturbations and thus lower peak flux events are detected in them. The lowest class event that was detected was a B2.4 flare, which has considerably lower peak flux than a C1 flare. However, as flares with a higher class and total integrated flux below the defined limits were not detected, the total integrated flux seems to be a more important factor in the occurrence of a VLF perturbation than the peak flux.

Some of the higher peak flux flares were also detected in the raw data, however, the signature in the residuals is greatly accentuated. The perturbations generally last slightly longer than the duration of the flare, with the onset time not delayed appreciably. Both increases and decreases in amplitude of the signals are seen to be caused by the flares. There has also been detection of flare perturbation occurring when the signal paths are in darkness. The times of these flares, in terms of onset, peak and end, are too well correlated with the perturbations to claim they are chance alignments.

Further work was done on the PCA components, rotating them to a new, more interpretable orientation via a varimax rotation. This rotation searches for simple structure in the component loadings matrix, thereby ensuring that each component is only well correlated with a few variables and each variable is defined by only a few components.

The results of the varimax rotation yielded very clear summer, winter and equinox signals. There was also a component that, while not vitally important to any of the variables, was either

positively or negatively correlated with most of them. This method has potential in identifying longer term variations in the amplitude of subionospherically propagating signals, such as might be caused by the eleven year solar cycle, given sufficient data.

Overall, PCA has proven to be a powerful analysis tool, being used both in the detection of transient events and the development of a quiet day approximation to the narrowband, subionospherically propagating data.

There are many aspects of this research that would benefit from further analysis. PCA applied to signal paths of much longer length would provide for an interesting comparison of the signal variations between different paths. Examination of data covering a larger period of time would allow longer duration variations in the signals to be identified.

The search for perturbations caused by TGFs could be repeated on a signal path that crossed the regions of highest density of TGF occurrence, thus clarifying the possibility of these events causing a perturbation.

Lastly, a more extensive examination of solar flare perturbations, in relation to total integrated flux, peak flux, time of day and time of year may determine the cause of the perturbations detected when the signal paths are in darkness. This would also allow the conditions for a flare to cause a perturbation to be more well defined.

Bibliography

T. Bai and P. A. Sturrock. Classification of Solar Flares. *Annual review of astronomy and astrophysics*, 27:421–467, 1989.

W. C. Bain and E. Hammond. Ionospheric solar flare effect observations. *Journal of Atmospheric and Terrestrial Physics*, 37:573–574, 1975.

D. Band, J. Matteson, L. Ford, B. Schaefer, D. Palmer, B. Teegarden, T. Cline, M. Briggs, W. Paciesas, G. Pendleton, G. Fishman, C. Kouveliotou, C. Meegan, R. Wilson, and P. Lestrade. BATSE observations of gamma-ray burst spectra. I - Spectral diversity. *The Astrophysical Journal*, 413:281–292, Aug. 1993. doi: 10.1086/172995.

R. Barr, D. Llanwyn Jones, and C. J. Rodger. ELF and VLF radio waves. *Journal of Atmospheric and Terrestrial Physics*, 62:1689–1718, 2000.

R. T. Brown. Ionospheric effects of cosmic gamma-ray bursts. *Nature*, 246:83–84, 1973. doi: 10.1038/246083a0.

K. G. Budden. The "Waveguide Mode" Theory of the Propagation of Very-Low-Frequency Radio Waves. *Proceedings of the IRE*, 36:772–774, 1957.

B. W. Carroll and D. A. Ostlie. *An Introduction to Modern Astrophysics*. Addison-Wesley Publishing Company, Inc., 1996.

M. W. Chevalier and U. S. Inan. A Technique for Efficiently Modeling Long-Path Propagation for Use in Both FDFD and FDTD. *IEEE Antennas and Wireless Propagation Letters*, 5:525–528, 2006.

M. A. Clilverd, N. R. Thomson, and C. J. Rodger. Sunrise effects on VLF signals propagating over a long north-south path. *Radio Science*, 34:939–948, 1999.

D. D. Crombie. Periodic fading of VLF signals received over long paths during sunrise and sunset. *Journal of Research National Bureau of Standards, Radio Science*, 68D:27–34, 1964.

S. A. Cummer. Modeling Electromagnetic Propagation in the Earth-Ionosphere Waveguide. *IEEE Transactions on Antennas and Propagation*, 48:1420–1430, 2000.

J. Cummings, S. D. Barthelmy, E. Fenimore, N. Gehrels, H. Krimm, C. Markwardt, K. McLean, D. Palmer, A. Parsons, J. L. Racusin, T. Sakamoto, G. Sato, M. Stamatikos, J. Tueller, and T. Ukwatta. GRB 080319B, Swift-BAT refined analysis. GCN Circular 7462, 2008.

J. R. Dwyer. Source mechanisms of terrestrial gamma-ray flashes. *Journal of Geophysical Research*, 113, D10103, 2008. doi: 10.1029/2007JD009248.

J. R. Dwyer and D. M. Smith. A comparison between Monte Carlo simulations of runaway breakdown and terrestrial gamma-ray flash observations. *Geophysical Research Letters*, 32, L22804, 2005. doi: 10.1029/2005GL023848.

C.-F. Enell, P. T. Verronen, M. J. Beharrell, J. P. Vierinen, A. Kero, A. Sepala, F. Honary, T. Ulich, and E. Turunen. Case study of the mesospheric and lower thermospheric effects of solar X-ray flares: Coupled ion-neutral modelling and comparison with EISCAT and riometer measurements. *Annales Geophysicae*, 26:2311–2321, 2008.

E. E. Fenimore. The Average Temporal and Spectral Evolution of Gamma-Ray Bursts. *The Astrophysical Journal*, 518:375–379, June 1999. doi: 10.1086/307245.

G. J. Fishman and U. S. Inan. Observation of an ionospheric disturbance by a gamma-ray burst. *Nature*, 331:418–420, 1988.

N. Gehrels, G. Chincarini, P. Giommi, K. O. Mason, J. A. Nousek, A. A. Wells, N. E. White, S. D. Barthelmy, P. W. A. Roming, L. Angelini, D. N. Burrows, L. R. Cominsky, K. C. Hurley, F. E. Marshall, P. Me, L. M. Barbier, T. Belloni, S. Campana, P. A. Caraveo, M. M. Chester, O. Citterio, T. L. Cline, M. S. Cropper, J. R. Cummings, A. J. Dean, E. D. Feigelson, E. E. Fenimore, D. A. Frail, A. S. Fruchter, G. P. Garmire, K. Gendreau, G. Ghisellini, J. Greiner, J. E. Hill, S. D. Hunsberger, H. A. Krimm, S. R. Kulkarni, P. Kumar, F. Lebrun, C. B. Markwardt, B. J. Mattson, R. F. Mushotzky, J. P. Norris, J. Osborne, B. Paczynski, D. M. Palmer, A. M. Parsons, J. Paul, M. J. Rees, C. S. Reynolds, J. E. Rhoads, T. P. Sasseen, B. E. Schaefer, A. T. Short, A. P. Smale, I. A. Smith, L. Stella, G. Tagliaferri, T. Takahashi, M. Tashiro, L. K. Townsley, J. Tueller, M. J. L. Turner, M. Vietri, W. Voges, M. J. Ward, R. Willingale, F. M. Zerbi, and W. W. Zhang. The swift gamma-ray burst mission. *The Astrophysical Journal*, 611:1005–1020, 2004.

S. Golenetskii, R. Aptekar, E. Mazets, V. Pal'shin, D. Frederiks, and T. Cline. Konus-Wind observation of GRB 080319B. GCN Circular 7482, 2008.

P. E. Green and J. D. Carroll. *Analyzing Multivariate Data*. The Dreyden Press, 1978.

B. W. Grefenstette, D. M. Smith, B. J. Hazelton, and L. I. Lopez. First RHESSI terrestrial gamma ray flash catalog. *Journal of Geophysical Research*, 114, 2009. doi: 10.1029/2008JA013721.

D. P. Grubor, D. M. Sulic, and V. Zigman. Classification of X-ray solar flares regarding their effects on the lower ionosphere electron density profile. *Annales Geophysicae*, 26:1731–1740, 2008.

A. V. Gurevich, G. M. Milikh, and R. Roussel-Dupre. Runaway electron mechanism of air breakdown and preconditioning during a thunderstorm. *Physics Letters A*, 165:463–468, 1992. doi: 10.1016/0375-9601(92)90348-P.

B. J. Hazelton, B. W. Grefenstette, D. M. Smith, J. R. Dwyer, X.-M. Shao, S. A. Cummer, T. Chronis, E. H. Lay, and R. H. Holzworth. Spectral dependence of terrestrial gamma-ray flashes on source distance. *Geophysical Research Letters*, 36, L01108, 2009. doi: 10.1029/2008GL035906.

U. S. Inan, A. Slingeland, and V. P. Pasko. VLF and LF signatures of mesospheric/lower ionospheric response to lightning discharges. *Journal of Geophysical Research*, 101:5219–5238, 1996.

U. S. Inan, N. G. Lehtinen, S. J. Lev-Tov, M. P. Johnson, T. F. Bell, and K. Hurley. Ionization of the lower ionosphere by gamma-rays from a magnetar: detection of a low energy (3 – 10 keV) component. *Geophysical Research Letters*, 26:3357–3360, 1999.

K. Kasturirangan, U. R. Rao, D. P. Sharma, R. G. Rastogi, and S. C. Chakravarty. Ionospheric effects of transient celestial x-ray and gamma-ray events. *Astrophysics and Space Science*, 42:57–62, 1976. doi: 10.1007/BF00645524.

K. J. W. Lynn. Anomalous sunrise effects observed on a long transequatorial VLF Propagation path. *Radio Science*, 2:521–530, 1967.

W. M. McRae and N. R. Thomson. Solar flare induced ionospheric D-region enhancements from VLF phase and amplitude observations. *Journal of Atmospheric and Terrestrial Physics*, 66: 77–87, 2004. doi: 10.1016/j.jastp.2003.09.009.

P. I. Meszaros. Gamma-ray bursts. *Reports on Progress in Physics*, 69:2259–2321, 2006. doi: 10.1088/0034-4885/69/8/R01.

R. J. Nemiroff, J. W. Bonnell, and J. P. Norris. Temporal and spectral characteristics of terrestrial gamma flashes. *Journal of Geophysical Research*, 102:9659–9665, 1997.

J. P. Norris, R. J. Nemiroff, J. T. Bonnell, J. D. Scargle, C. Kouveliotou, W. S. Paciesas, C. A. Meegan, and G. J. Fishman. Attributes of pulses in long bright gamma-ray bursts. *The Astrophysical Journal*, 459:393–412, 1996.

G. S. Paiva, A. C. Pavao, and C. C. Bastos. Seed electrons from muon decay for runaway mechanism in the terrestrial gamma ray flash production. *Journal of Geophysical Research*, 114, D03205, 2009. doi: 10.1029/2008JD010468.

R. A. Pappert and D. G. Morfitt. Theoretical and experimental sunrise mode conversion results at VLF. *Radio Science*, 10:537–546, 1975.

T. Piran. The physics of gamma-ray bursts. *Reviews of Modern Physics*, 76:1143–1210, Jan. 2005. doi: 10.1103/RevModPhys.76.1143.

G. L. Pollack and D. R. Stump. *Electromagnetism*. Pearson Education, Inc., 2002.

R. D. Preece, M. S. Briggs, R. S. Mallozzi, G. N. Pendleton, W. S. Paciesas, and D. L. Band. The BATSE Gamma-Ray Burst Spectral Catalog. I. High Time Resolution Spectroscopy of Bright Bursts Using High Energy Resolution Data. *The Astrophysical Journal Supplement Series*, 126: 19–36, Jan. 2000. doi: 10.1086/313289.

J. L. Racusin, S. V. Karpov, M. Sokolowski, J. Granot, X. F. Wu, V. Pal'shin, S. Covino, A. J. van der Horst, S. R. Oates, P. Schady, R. J. Smith, J. Cummings, R. L. C. Starling, L. W. Piotrowski, B. Zhang, P. A. Evans, S. T. Holland, K. Malek, M. T. Page, L. Vetere, R. Margutti, C. Guidorzi, A. P. Kamble, P. A. Curran, A. Beardmore, C. Kouveliotou, L. Mankiewicz, A. Melandri, P. T. O'Brien, K. L. Page, T. Piran, N. R. Tanvir, G. Wrochna, R. L. Aptekar, S. Barthelmy, C. Bartolini, G. M. Beskin, S. Bondar, M. Bremer, S. Campana, A. Castro-Tirado, A. Cucchiara, M. Cwiok, P. D'Avanzo, V. D/'Elia, M. D. Valle, A. de Ugarte Postigo, W. Dominik, A. Falcone, F. Fiore, D. B. Fox, D. D. Frederiks, A. S. Fruchter, D. Fugazza, M. A. Garrett, N. Gehrels, S. Golenetskii, A. Gomboc, J. Gorosabel, G. Greco, A. Guarnieri, S. Immler, M. Jelinek, G. Kasprowicz, V. La Parola, A. J. Levan, V. Mangano, E. P. Mazets, E. Molinari, A. Moretti, K. Nawrocki, P. P. Oleynik, J. P. Osborne, C. Pagani, S. B. Pandey, Z. Paragi, M. Perri, A. Piccioni, E. Ramirez-Ruiz, P. W. A. Roming, I. A. Steele, R. G. Strom, V. Testa, G. Tosti, M. V. Ulanov, K. Wiersema, R. A. M. J. Wijers, J. M. Winters, A. F. Zarnecki, F. Zerbi, P. Mészáros, G. Chincarini, and D. N. Burrows. Broadband observations of the naked-eye γ-ray burst GRB 080319B. *Nature*, 455:183–188, 2008. doi: 10.1038/nature07270.

Y. Reuveni and C. Price. A new approach for monitoring the 27-day solar rotation using VLF radio signals on the Earths surface. *Journal of Geophysical Research*, 114, A10306, 2009. doi: 10.1029/2009JA014364.

N. R. Thomson. Experimental daytime VLF ionospheric parameters. *Journal of Atmospheric and Terrestrial Physics*, 55:173–184, 1993.

N. R. Thomson, I. Waldrom, and W. M. Mcrae. D-region electron densities during solar flares from vlf radio measurements. In *XXVIIth General Assembly of the International Union of Radio Science*, Maastricht, 2002. URL `http://www.ursi.org/Proceedings/ProcGA02/papers/p0375.pdf`.

N. R. Thomson, C. J. Rodger, and R. L. Dowden. Ionosphere gives size of greatest solar flare. *Geophysical Research Letters*, 31, L06803, 2004. doi: 10.1029/2003GL019345.

N. R. Thomson, C. J. Rodger, and M. A. Clilverd. Large solar flares and their ionospheric D region enhancements. *Journal of Geophysical Research*, 110, A06306, 2005. doi: 10.1029/2005JA011008.

J. Tueller, S. D. Barthelmy, W. H. Baumgartner, J. R. Cummings, E. E. Fenimore, N. Gehrels, H. A. Krimm, C. B. Markwardt, D. M. Palmer, A. M. Parsons, T. Sakamoto, G. Sato, M. Stamatikos, and T. N. Ukwatta. GRB 090113: Swift-BAT refined analysis. GCN Circular 8808, 2009.

T. Ukwatta, P. J. Brown, J. Cummings, E. Fenimore, N. Gehrels, H. Krimm, C. Markwardt, K. McLean, D. Palmer, A. Parsons, T. Sakamoto, G. Sato, M. Stamatikos, and J. Tueller. GRB 080319D, Swift-BAT refined analysis. GCN Circular 7498, 2008.

J. R. Wait. *Electromagnetic Waves in Stratified Media*. Pergamon Press Ltd., 1962.